INFLUENCE OF FIBER WEIGHT CONTENT AND FIBER DISTRIBUTION ON FUNCTIONAL PROPERTIES OF GLASS-FIBER REINFORCED COMPOSITES

Barbara Bertoncelj

Doctoral Dissertation
Jožef Stefan International Postgraduate School
Ljubljana, Slovenia

Supervisor: Prof. Dr. Barbara Malič, Jožef Stefan Institute, Ljubljana, Slovenia
Co-Supervisor: Dr. Janez Rihtaršič, Domel, d.o.o., Železniki, Slovenia

Evaluation Board:
Prof. Dr. Slavko Bernik, Chair, Jožef Stefan Institute, Ljubljana, Slovenia
Asst. Prof. Dr. Andreja Benčan Golob, Member, Jožef Stefan Institute, Ljubljana, Slovenia
Dr. Janez Bernard, Member, Slovenian National Building and Civil Engineering Institute, Ljubljana, Slovenia

MEDNARODNA PODIPLOMSKA ŠOLA JOŽEFA STEFANA
JOŽEF STEFAN INTERNATIONAL POSTGRADUATE SCHOOL



Barbara Bertoncelj

INFLUENCE OF FIBER WEIGHT FRACTION AND FIBER DISTRIBUTION ON FUNCTIONAL PROPERTIES OF GLASS-FIBER REINFORCED COMPOSITES

Doctoral Dissertation

VPLIV DELEŽA IN PORAZDELITVE STEKLENIH VLAKEN NA FUNKCIJSKE LASTNOSTI KOMPOZITOV NA OSNOVI POLIMERNE MATRICE

Doktorska disertacija

Supervisor: Prof. Dr. Barbara Malič

Co-Supervisor: Dr. Janez Rihtaršič

Ljubljana, Slovenia, March 2017

Acknowledgments

This thesis would not have been possible without the support and guidance of many people, who helped me over the years.

First, I would like to express my appreciation to the Domel company for giving me the opportunity to start this experience, for supporting me and giving me the resources and time needed to complete my PhD work.

Nothing less, my sincere gratitude also goes to my supervisor Prof. Dr. Barbara Malič for her guidance, invaluable insights and innumerable suggestions. I truly appreciate her patience, support, motivation and willingness to take the time for discussions, for checking my drafts, for her suggestions, pieces of advice and comments during various stages of my research. I would like to thank her for giving me the opportunity and an "occasional" place to work at the Electronic Ceramics Department-K5 at the Jožef Stefan Institute, as well as for allowing me to use the laboratory equipment during my research.

I am grateful to Dr. Janez Rihtaršič, my supervisor from the Domel company. I acknowledge his support and patience during these years. Especially I appreciate him giving me enough time to complete this thesis.

My special thanks goes to Dr. Katarina Vojisavljević who helped me during all my years of the PhD study. I am extremely grateful for her help with the SEM analysis, for her effort, support, suggestions and assistance with writing scientific papers.

I would like to extend the acknowledgement to all the colleagues at the Electronic Ceramics Department, especially to Jena Cilenšek for the thermal analysis measurements and for her help with sample preparation, Silvo Drnovšek for technical support, Dr. Marko Vrabelj for his advice and demonstration of thermal conductivity and specific heat capacity measurements, and Dr. Tanja Pečnik for all the help and advice, especially during the finalizing stages of this thesis.

It is a pleasure to thank Dr. Gregor Trefalt from the University of Geneva for performing the Monte Carlo simulations, RDF analysis and for the support with the Voronoi diagram analysis.

I appreciate the contribution of Dr. Ema Žagar and Assoc. Prof. Dr. Miro Huskić for performing DMA measurements. I also thank Edi Krajnc for the XRD measurements (National Institute of Chemistry, Slovenia).

I am grateful to all my co-workers in the Domel company, particularly to Tomaž Kosem for his assistance with the flexural strength measurements, Gregor Jelenc and Tomaž Benedičič for ordering and providing the samples, Igor Demšar and Jure Brovč for the sample molding and answering all the technical questions. In addition, I acknowledge the help of all the other co-workers as well as friends that have, in any way, contributed to this PhD thesis, helped me and encouraged me during these years.

I wish to thank the Ministry of Education, Science and Sport of the Republic of Slovenia and the European Commission through the European Social Fund for the scholarship funding, and the Center of Excellence NAMASTE and the Center for Electronic Microscopy at the Jožef Stefan Institute for allowing the use of their equipment.

Finally, I would like to acknowledge my closest family for their love, support and encouragement.

Abstract

Bulk molding compound (BMC) composites are short fiber reinforced polymer-matrix composites, predominantly used for the mass production of complex-shaped components in electro, automotive and appliance industry. Despite the advantages of high specific strength and design flexibility as compared to metals, the manufacturing of polymer-matrix composites on industrial scale suffers the problems of reproducibility. Environmental issues, related to styrene emissions during manufacturing and waste management of end-of-life composites also need to be considered.

Mechanical, viscoelastic and thermal properties of BMC composites are influenced by the orientation and distribution of fibers in the microstructure. The latter is formed during the molding process and depends on the composition, molding conditions and on the geometry of the mold cavity. Thus, a molded BMC product can exhibit a high microstructural variation, resulting in random and regular or non-uniform, clustered microstructural patterns. In the Thesis, we address and discuss the relation between the microstructure, mechanical and thermal properties of BMC composites with different weight fractions of electric (E)-glass fibers (EGFs), i.e. from 0 wt% to 35 wt%.

The Voronoi tessellation method, radial distribution functions (RDFs), stereological analysis and derived statistical descriptors are used to quantitatively describe the microstructures of BMC composites with different fiber fractions (5 wt%–20 wt%). The experimental microstructures were obtained perpendicular on the filling-flow direction, i.e., in cross-section. They were compared to the modeled microstructures with random fiber distribution, in order to distinguish between different microstructural patterns and to describe the level of microstructural uniformity. We show that the highest level of microstructural uniformity is obtained in the composite with 7.5 wt% of fibers and it decreases either with lower or progressively higher glass fiber content. The latter composite has the best coincidence of the experimental and modelled Voronoi area size distributions and RDF, as well as the lowest calculated homogeneity parameter, HP_A (0.68) and the smallest extent of local disorder (~40 µm).

The flexural strength of BMC composites reaches the peak values at EGF content between 10 wt% and 15 wt%, 110 ± 8 MPa and 121 ± 16 MPa, respectively, and at lower or higher EGF fractions the flexural strength is much lower. The maximum flexural strength is attributed to a combined effect of an optimum fiber content and fiber distribution uniformity, while a decrease in the flexural strength at EGF contents exceeding 15 wt% is a consequence of progressively pronounced microstructural disorder. The reinforcing effect of fibers is the highest in the composite with 15 wt% of EGFs, as confirmed by the lowest value of the coefficient of reinforcement, C (0.79).

Thermal conductivity of BMC composites decreases with increasing EGF weight content from 0.960 W/mK to 0.771 W/mK for the composites containing 0 wt% and 35 wt% of fibers, which suggests that it is to a large extent influenced by the fraction of EGFs, and not or only slightly by their distribution in the microstructure.

Our results demonstrate that the optimal BMC material composition for a certain application is a compromise between the high level of microstructural uniformity and suitable mechanical and thermal properties. Furthermore, the quantitative microstructural analysis is found to be a reliable support in the product design and in the manufacturing process of BMC parts on an industrial scale.

Povzetek

Mase za preoblikovanje (angl: *bulk molding compounds*, BMC) so kompoziti na osnovi polimerne matrice, ojačane s steklenimi vlakni. Uporabljamo jih za masovno izdelavo različnih izdelkov, predvsem v elektro in avtomobilski industriji ter beli tehniki. Kljub prednostim, ki jih kompoziti izkazujejo v primerjavi s kovinami, kot sta velika specifična trdnost in fleksibilnost oblikovanja, se pri izdelavi tovrstnih izdelkov srečujemo s problemom ponovljivosti izbranih lastnosti. Poleg tega se v industriji kompozitov srečujemo z okoljskimi vprašanji, predvsem z izhajanjem stirena med procesom oblikovanja, kot tudi z ravnanjem z odpadnimi kompoziti.

Mehanske, viskoelastične in toplotne lastnosti BMC kompozitov so v veliki meri odvisne od usmerjenosti in porazdelitve vlaken v mikrostrukturi. Slednja nastane med procesom brizganja in je odvisna predvsem od sestave, pogojev brizganja in geometrije kalupa. BMC kompoziti lahko izkazujejo velike razlike v (ne)urejenosti porazdelitve steklenih vlaken.

V disertaciji obravnavamo povezavo med mikrostrukturo, mehanskimi in toplotnimi lastnostmi BMC kompozitov z različnimi masnimi deleži steklenih vlaken, primernih za uporabo v elektrotehniki, in sicer od 0 % do 35 %.

Metode Voronoijevih diagramov, radialnih porazdelitvenih funkcij (angl: *radial distribution function,* RDF), stereološko analizo in statistične deskriptorje smo uporabili za kvantitativni opis mikrostruktur BMC kompozitov z masnimi deleži steklenih vlaken od 5 % do 20 %. Eksperimentalne mikrostrukture kompozitov s prevladujočo usmerjenostjo vlaken v smeri polnjenja kalupa smo analizirali pravokotno na smer polnjenja in primerjali z modeliranimi mikrostrukturami z naključno porazdelitvijo vlaken, na osnovi česar smo lahko določili stopnjo urejenosti mikrostrukture. Kompozit s 7,5 % vlaken izkazuje največjo stopnjo urejenosti mikrostrukture. Slednja se zmanjša v kompozitih z bodisi manjšo bodisi čedalje večjo vsebnostjo vlaken. V kompozitu s 7,5 % vlaken je ujemanje med eksperimentalno in modelirano porazdelitvijo Voronoijevih poligonov in RDF najboljše, tudi izračunana vrednost parametra homogenosti HP_A (0,68) in obseg mikrostrukturne neurejenosti (~40 µm) sta najmanjša.

Upogibna trdnost BMC kompozitov doseže največje vrednosti v kompozitih z masnim deležem steklenih vlaken med 10 % in 15 %, in sicer od 110 ± 8 MPa do 121 ± 16 MPa. Pri bodisi višjih bodisi nižjih deležih steklenih vlaken je upogibna trdnost izrazito manjša. Povečanje upogibne trdnosti pripisujemo kombiniranemu učinku ojačenja zaradi optimalne vsebnosti vlaken in enakomerni porazdelitvi vlaken v mikrostrukturi, medtem ko je zmanjšanje upogibne trdnosti pri deležu vlaken nad 15 % posledica naraščajoče neurejenosti mikrostrukture. Ojačevalni učinek steklenih vlaken je največji pri kompozitu s 15 % steklenih vlaken, kar izkazuje tudi najnižja vrednost koeficienta ojačitve, C, (0,79).

Toplotna prevodnost BMC kompozitov se s povečevanjem deleža steklenih vlaken zmanjša od 0,960 W/mK (0 % vlaken) do 0,771 W/mK (35 % vlaken). Rezultati nakazujejo, da je toplotna prevodnost kompozitov odvisna predvsem od deleža steklenih vlaken in manj od njihove porazdelitve v mikrostrukturi.

Rezultati kažejo, da je optimalna sestava BMC materiala za določeno uporabo kompromis med zadostno stopnjo urejenosti mikrostrukture in primernimi mehanskimi in toplotnimi lastnostmi. Mikrostrukturna analiza je lahko zanesljiva podpora v fazi oblikovanja in izdelave izdelka iz BMC kompozitov.

Contents

List of Figures **xiii**

List of Tables **xvii**

Abbreviations **xix**

Symbols **xxi**

1 Introduction **1**
1.1 Composites ... 1
1.1.1 Polymer-matrix composites ... 2
1.1.1.1 Composites - replacement for metals ... 3
1.2 Bulk Molding Compounds ... 5
1.2.1 Composition ... 6
1.2.1.1 Unsaturated polyester resin ... 6
1.2.1.2 Glass fiber reinforcement ... 9
1.2.1.3 Mineral fillers ... 9
1.2.1.4 Additives ... 10
1.2.2 Processing methods ... 10
1.3 Microstructure ... 11
1.3.1 Fiber content, distribution and orientation ... 12
1.3.2 Characterization of composite microstructures ... 14
1.3.2.1 Voronoi diagram analysis ... 14
1.3.2.2 Radial distribution function ... 19
1.4 Influence of the Microstructure on Mechanical Properties of the Composites ... 21
1.4.1 Influence of the microstructure on dynamic mechanical properties ... 23
1.5 Thermal Properties ... 25
1.5.1 Thermal conductivity ... 25
1.5.2 Thermal stability and decomposition ... 26

2 Environmental Considerations in Manufacturing and Waste Management of Polymer-Matrix Composites **29**
2.1 Styrene ... 29
2.1.1 Occupational exposure ... 30
2.1.1.1 Workplace exposure limits ... 30
2.1.1.2 Health effects of styrene exposure ... 31
2.1.2 Monitoring exposure to styrene emissions ... 32
2.1.2.1 Exposure to styrene emissions in the company ... 32
2.2 Waste Management of Composites ... 33
2.2.1 Recycling of fiber-reinforced composites ... 34

3 Aims and Hypotheses **37**

4 Materials and Methods **39**
4.1 Sample Preparation ... 39
4.2 Characterization Methods ... 41
4.2.1 Density measurements ... 41
4.2.2 Scanning Electron Microscopy ... 42
4.2.3 Image analysis ... 43
4.2.3.1 Voronoi diagrams ... 43
4.2.4 Computer-simulated microstructures ... 45
4.2.5 Radial distribution function ... 46
4.2.6 Stereological analysis ... 47
4.2.7 Three-point bending test ... 48
4.2.8 Thermal analysis ... 48
4.2.8.1 Dynamic mechanical analysis ... 48
4.2.8.2 Thermogravimetry and Differential Thermal Analysis ... 48
4.2.8.3 Differential Scanning Calorimetry ... 49
4.2.9 Thermal conductivity measurement ... 49
4.2.10 X-ray powder-diffraction analysis ... 50

5 Results and Discussion **51**
5.1 Microstructure ... 51
5.1.1 Microstructure of BMCs with EGF weight content from 5 % to 20 % ... 54
5.1.1.1 Voronoi diagram analysis of BMC composite in different areas of sample cross-section ... 54
5.1.1.2 Voronoi diagram analysis of experimental and modeled microstructures ... 58
5.1.1.3 Radial distribution function ... 64
5.1.1.4 Elongation parameter ... 67
5.1.2 Microstructure of BMCs with EGF weight content from 25% to 35% ... 70
5.1.3 Summary ... 72
5.2 Mechanical Properties ... 73
5.2.1 Flexural strength ... 73
5.2.2 Dynamic mechanical properties ... 76
5.2.3 Summary ... 78
5.3 Thermal Properties ... 78
5.3.1 Thermal stability ... 79
5.3.2 Specific heat capacity ... 82
5.3.3 Thermal conductivity ... 82
5.3.4 Summary ... 83

6 Summary and Conclusions **85**

Appendix A
A.1 Definition of Voronoi Diagram ... 89

References **91**

Bibliography **101**

Biography **103**

List of Figures

Figure 1.1: Schematic representation of two-phase composite material (left). The matrix phase and the dispersed phase are different in chemical composition. Formation of the polymer-matrix composite (right). Fibers of various lengths are bound together with the polymer matrix to form a composite material. Adapted from [4]. 2
Figure 1.2: An overview of FRCs. Redrawn from [6]. 3
Figure 1.3: Comparison between metals and polymer-matrix composites. Composites have lower weight, lower thermal expansion and higher strength, stiffness and fatigue resistance as compared to steel and Al. Adapted from [7]. Stiffness of a material is defined as a measure of resistance to deformation in response to the applied force. Fatigue resistance is the tendency of a material to fracture or fail under cyclic loading (bending, axial or torsional). 4
Figure 1.4: An example of the product from the BMC composite for automotive industry. 6
Figure 1.5: Synthesis of an unsaturated polyester molecule by condensation reaction. The sign * indicates unsaturated sites for the cross-linking reaction. Adapted from [10]. 7
Figure 1.6: Chemical structure of a cross-linked polyester with styrene monomer [11]. 8
Figure 1.7: Change of viscosity during the cross-linking of a thermoset molding compound. The combination (red curve) of the thinning (blue curve) and crosslinking (green curve) process is what is actually happening in the mold cavity during the manufacturing of PMCs. After [2]. 8
Figure 1.8: Injection molding process. Adapted from [17]. 11
Figure 1.9: Transfer molding process. Adapted from [18]. 11
Figure 1.10: Different spatial arrangements and characteristics that determine the properties of fiber-reinforced polymer-matrix composites: a) concentration, b) size, c) shape, d) distribution, e) orientation. From [22]. 12
Figure 1.11: Shematic representation of fiber orientation in the test specimen. During the molding process, the fibers tend to align parallel with the filling flow direction. 12
Figure 1.12: Representation of different orientations in FRC (from the left side): discontinuous and randomly oriented, discontinuous and aligned, continuous and aligned. Redrawn after [22]. 13
Figure 1.13: SEM micrograph of the polished cross-section of a BMC composite containing 20 wt% of EGFs. The glass fibers are surrounded by the particles of the $CaCO_3$ mineral filler distributed in the polymer matrix. The glass fiber intersections, marked with red, can be easily identified from the micrograph. By measuring the axes of the circles and ellipses, the fiber orientation parameters can be determined. 14
Figure 1.14: An example of a Voronoi diagram constructed from eight points. 15
Figure 1.15: Comparison of two differently processed unidirectional carbon fiber composites. After [48]. 16
Figure 1.16: Voronoi diagrams of zirconia-toughened alumina composites prepared under different processing conditions. The homogeneity parameter derived from the area of Voronoi polygons (HP_A) indicates that the most uniform distribution of the zirconia phase

is in the samples a) and b) (0.69 and 0.70, respectively) and the least in the sample c) (0.93), which also had the highest wear rate, k_W. Redrawn after [42]. 17
Figure 1.17: Microstructures of PZT-ZrO_2 composites prepared with the non-modified and modified synthesis. The area size distributions of Voronoi polygons show that modification of the synthesis contributes to a more uniform ZrO_2 particle distribution as compared to the composite prepared with the non-modified synthesis where large polygon areas indicate clustering of particles. After [43]. 18
Figure 1.18: Voronoi diagrams of clustered and random computer-simulated point-patterns with the corresponding size distributions of Voronoi polygons. In the clustered point pattern, a high peak at smaller values and the presence of large polygons in the size distribution reflects clustering. Redrawn from [45]. 19
Figure 1.19: Radial distribution function is defined as the probability of finding a particle in a shell dr at a specific distance r from a certain "reference" particle (black marked circle). The particles in the first shell are accountable for the first peak, the particles in the second shell correspond to the second peak in RDF, etc. Redrawn from [50]. 20
Figure 1.20: RDF of modeled random composite microstructures with different fiber volume fractions (from 0.10 to 0.50). The sharp peak indicates a higher fiber density at the distance of the closest approach. With increasing volume fraction of the fibers, the peak intensity increases. Redrawn after [51]. 21
Figure 1.21: a) Tensile strength, b) tensile modulus and c) mean fiber length of the polypropylene (PP) composites reinforced with short glass (SGF) and short carbon fibers (SCF). The tensile strength only slightly increases with increasing fiber content, meanwhile the enhancement of the modulus with a higher fiber content is more pronounced. The mean length of glass and carbon fibers in the PP matrix decreases with increasing fiber content, which demonstrates greater fracture of the fibers during the molding process with increasing fiber fraction. Redrawn after [55]. 22
Figure 1.22: Tensile and flexural strenth of polypropylene (PP) composites reinforced with glass fibers. The highest tensile and flexural strength is achieved at fiber weight fraction of 40 %– 50 %. Redrawn after [58]. 23
Figure 1.23: The influence of glass fiber content on dynamic mechanical properties. The storage (a) and loss modulus (b) increase with increasing glass fiber content. Glass transition temperature (Tg) determined from the $tan\,\delta$ curves (c) is not affected by the glass fiber content. Redrawn after [65]. 24
Figure 1.24: The mechanism of heat transfer in polymer-matrix composites: the size and the shape of the inclusions influence the thermal conductivity. Redrawn from [75]. 26
Figure 1.25: Representation of different states and transitions in a thermosetting polymer during heating. Redrawn after [84]. 27
Figure 2.1: EU waste hierarchy: stages and associated actions. Redrawn after [103]. 34
Figure 4.1: Composition of BMC composite samples with varying EGF (0/5/7.5/10/12.5/15/20/25/30/35 wt%) and $CaCO_3$ content. The number denotes the number of the series. 40
Figure 4.2: Schematic representation of the filling flow direction of BMC material during transfer molding, dimensions of the test specimen, cutting direction and sample position. 41
Figure 4.3: Molded test specimens of BMC composites with 0 wt%, 5 wt%, 10 wt%, 15 wt% and 25 wt% of EGFs. 41
Figure 4.4: Sampling scheme of the cross-sectional area for the microstructural analysis. 42
Figure 4.5: Steps in construction of Voronoi diagrams: SEM micrograph (a), binary point-pattern image (b) obtained from the SEM micrograph by point marking of each fiber and the Voronoi diagram (c) generated from the point-pattern image. 44

Figure 4.6: Modeled random distribution of disks (d) and a corresponding Voronoi diagram (e). 46
Figure 4.7: Stereological analysis. The fibers on the SEM micrograph (a) are outlined in black (b). 47
Figure 4.8: Schematic representation of the HotDisk measurement. 49
Figure 5.1: Representation of the selected BMC samples and methods that were used and performed for microstructural analysis. 51
Figure 5.2: Plan-view (left) and cross-sectional (right) SEM micrographs of BMC composite samples with 0 wt%, 5 wt%, 15 wt% and 30 wt% of EGF content. 53
Figure 5.3: SEM micrographs of areas 1, 5 and 9 of the samples with 5 wt%, 10 wt%, 15 wt% and 20 wt% of EGFs. 55
Figure 5.4: Voronoi diagrams constructed from SEM micrographs of areas 1, 5 and 9 of the samples with 5 wt%, 10 wt%, 15 wt% and 20 wt% of EGFs. The fiber distribution uniformity was evaluated by the homogeneity parameter HP_A 57
Figure 5.5: Cross-section micrographs (first column) of BMC composite samples with 5 wt%, 7.5 wt% and 10 wt% of EGFs and corresponding Voronoi diagrams (second column). Modeled patterns of fiber distribution and corresponding Voronoi diagrams are shown in the third and fourth column, respectively. 59
Figure 5.6: Cross-section micrographs (first column) of BMC composite samples with 12.5 wt%, 15 wt% and 20 wt% of EGFs and corresponding Voronoi diagrams (second column). Modeled patterns of fiber distribution and corresponding Voronoi diagrams are shown in the third and fourth column, respectively. 60
Figure 5.7: Distribution of Voronoi relative polygon areas of experimental and modeled fiber distributions of BMC composites with varying EGF weight content. 63
Figure 5.8: RDFs of experimental and modeled fiber distributions (from 5 wt% to 20 wt% of EGFs). The RDFs of the samples with 7.5 wt% and 20 wt% of fibers in the distance range from 0 µm to 40 µm are enlarged on the right. In the first case the experimental and modeled RDFs are very close, meanwhile, when the fiber content increases, the difference between the experimental and modeled RDFs becomes more pronounced indicating inhomogeneous fiber distribution. The arrows denote the scale of local microstructure disorder. 66
Figure 5.9: The mean values of EP of BMC composites with different EGF weight fractions showing that the EP is increasing with increasing fiber content. As evident from the representative BMC microstructures (insets of black fibers on white background), at higher fiber content some of the fibers also orient in different directions as a consequence of smaller available space. 68
Figure 5.10: EP distributions of BMC composite samples with 5 wt% to 20 wt% of EGF content 69
Figure 5.11: Micrographs of the plan-view (left) and cross-section areas (right) of BMC composite samples with 25 wt%, 30 wt% and 35 wt% of EGFs. At higher fiber weight fractions the microstructure is highly disordered, resulting in groups of fibers with the same orientation direction, poor wetting of fibers and increased porosity. 71
Figure 5.12: Cross-section SEM micrograps of BMC composite sample containing 30 wt% of EGFs where the difference in fiber density is clearly seen. These observations confirm high local disorder of the microstructure. 71
Figure 5.13: Micro cracks of EGFs observed in the sample with 30 wt% of fiber content. At higher fiber content the fibers are heavily loaded and bent which results in increased fiber cracking and breaking. 72
Figure 5.14: Flexural strength and flexural modulus of BMC composites as a function of EGF content. Flexural strength is increasing with increasing EGF weight fraction, reaching

the peak value at 15 wt% of EGFs. Flexural modulus also increases with increasing EGF content up to 20 wt% and with further increase in EGF content it remains constant. ... 74
Figure 5.15: Dependence of the mechanical strength of composites on the fiber content. The strength increase depends not only on the fraction of the fibers but also on their orientation. The arrow denotes the direction of the applied stress. ... 75
Figure 5.16: Storage modulus (E'), loss modulus (E'') and damping behaviour ($tan\ \delta$) of BMC composites with different fiber weight fractions in the temperature range from 25 °C to 190 °C. ... 77
Figure 5.17: DSC curves of BMC composite materials before curing with 0 wt%, 20 wt% and 30 wt% of EGFs. ... 79
Figure 5.18: TG/DTA curves of BMC composites with 0 wt%, 10 wt%, 20 wt% and 30 wt% of EGFs recorded in synthetic air atmosphere. ... 80
Figure 5.19: Thermal decomposition of representative BMC composite containing 15 wt% of EGFs. ... 81
Figure 5.20: XRD pattern of the residue obtained after heating the BMC composite with 15 wt% of EGFs up to 900 °C. CaO is the crystalline phase in the thermal decomposition product. ... 81
Figure 5.21: Thermal conductivity of BMC composites as a function of the EGF content. The results are presented for individual series of the samples. In all three series the thermal conductivity shows a decrease with increasing EGF content with similar slopes of the fitted lines. ... 83
Figure 6.1: Relation between the microstructural descriptors and physical properties of BMC composites as a function of the EGF content. ... 86

List of Tables

Table 1.1: Comparison of properties of some traditional materials and PMCs. Adapted from [4]. 5
Table 1.2: Typical formulation of BMCs, based on a polyester matrix. From [9]. 6
Table 1.3: Typical composition of different types of glass fibers [7]. 9
Table 1.4: Properties of E-glass fibers. 9
Table 1.5: Properties of $CaCO_3$ [14]....10
Table 1.6: List of the main additives in the production of BMCs. 10
Table 2.1: Properties of styrene monomer. 30
Table 2.2: Styrene concentration limits, for 8-hour exposure TWA and STEL (or C when STEL data is not available) in different countries across Europe [90]....31
Table 2.3: Results of worker's exposure to styrene emissions. 33
Table 5.1: Number of fibres (N_f), mean area size (μ_A) and standard deviation (σ_A) of Voronoi polygons used in calculations of HP_A. 57
Table 5.2: Mean area size (μ_A), standard deviation (σ_A) and homogeneity parameter HP_A of Voronoi polygons. 62
Table 5.3: Flexural strength of BMC composites with 5 wt%–20 wt% of EGFs (the third series of BMC samples)....75
Table 5.4: Glass transition temperature of BMC composites with different EGF weight contents as determined from the loss modulus curves and the coefficient of reinforcement C. 77
Table 5.5: Specific heat capacity of BMC composites with different EGF weight fractions. 82
Table 5.6: Thermal conductivity of individual phases in the composite, i.e. polymer, E-glass fibers and $CaCO_3$ mineral filler as reported in the literature. 83

Abbreviations

ACGIH ... Association Advancing Occupational and Environmental Health
BMC ... bulk molding compound
BN ... boron nitride
DMA ... dynamic mechanical analysis
DSC ... differential scanning calorimetry
DTA ... differential thermal analysis
EGF ... E-glass fibers
ELV ... end of life vehicles directive
EP ... elongation parameter
FE-SEM ... field emission scanning electron microscope
FRC ... fiber reinforced composite
GFRC ... glass fiber reinforced composites
IARC ... International Agency for Research on Cancer
ISO ... International Standardization Organization
MAPP ... maleated polypropylene
NIOSH ... National Institution for Occupational Safety and Health
OEL ... occupational exposure limit
OSHA ... Occupational Safety and Health Administration
PM ... polymer matrix
PMC ... polymer-matrix composite
PP ... polypropylene
PZT ... $Pb(Zr,Ti)O_3$
RDF ... radial distribution function
SCF ... short carbon fiber
SEM ... scanning electron microscope
SGF ... short glass fiber
SMC ... sheet molding compound
STEL ... short term exposure limit
TG ... thermogravimetry
TWA ... time weighted average concentration
UP ... unsaturated polyester
US EPA ... The United States environmental protection agency
WEEE ... Waste electrical and electronic equipment
wt ... weight
XRD ... X-ray powder diffraction analysis

Symbols

V_f	... volume fraction
A	... area
A_p	... absolute polygon area size
A_r	... relative polygon area size
A_{total}	... area size of the sample
b	... width of the sample in 3-point bending test
C	... coefficient of reinforcement
c_p	... specific heat capacity
$c_p^{standard}$	... specific heat capacity of the standard sample
$\cos\ \delta$	... phase angle in dynamic mechanical analysis
DSC_{sample}	... DSC curve of the sample
$DSC_{standard}$	... DSC curve of the standard sample
E'	... storage modulus
E''	... loss modulus
E_f	... flexural modulus
E'_g	... storage modulus in the glassy state
E'_r	... storage modulus in the rubbery state
$g(r)$	... pair distribution function
h	... thickness of the sample in 3-point bending test
HP_A	... homogeneity parameter calculated from the area size of Voronoi polgons
HP_q	... homogeneity parameter, where q is corresponding property
i	... number of polygons
k_w	... wear rate
l	... perimeter
l	... span between the supports in 3-point bending test
m_{air}	... mass of the sample weighted in the air
m_{water}	... mass of the sample weighted in the water
N	... number of polygons
N_f	... number of fibers
N_i	... number of points
n	... number of polygon faces
P	... maximum fracture load in 3-point bending test
p, q	... elements in the plane
r	... distance
S	... set of points in the plane
$\sin\ \delta$	... phase angle in dynamic mechanical analysis
T_d	... decomposition temperature
T_g	... glass transition temperature
$tan\ \delta$	... loss factor
x_i	... area size of the polygon i

δ	... Euclidean distance function
ε_0	... strain in dynamic mechanical analysis
θ	... diffraction angle
λ	... thermal conductivity
μ	... mean value
μ_A	... mean area size of polygon
ρ	... density
ρ_{water}	... density of water
σ	... standard deviation
σ_A	... standard deviation of the Voronoi polygons area size
σ_f	... flexural strength
σ_a	... stress in dynamic mechanical analysis

Chapter 1

Introduction

We begin the Introduction chapter with a general overview of composite materials. The polymer-matrix composites (PMCs), where the emphasis is given to bulk molding compounds (BMCs), are described – we address their composition, structure and the manufacturing process. We continue with the description of the microstructural features that influence the properties of composites. In the last part of this chapter the influences of fiber content, distribution and orientation on mechanical and thermal properties of polymer-matrix composites are discussed.

1.1 Composites

By general definition [1], composites are multi-phase materials, i.e. a combination of two or more solid materials that are different in chemical composition and separated by an interphase boundary. The main concept of composites is to achieve better properties with a combined action of the properties of individual constituents.

The principle of composite materials is found in nature, e.g. wood, where cellulose fibers are held together by lignin. By nature, both materials are weak, but together they form a much stronger material. The first technical composites for commercial applications were made in the 1940's and 1950's, i.e. after the development of glass fibers in 1930 that were used as reinforcement in the polymer matrix [2]. Nowadays, composites are used in various industrial areas, including aerospace, automotive, marine, sporting goods, consumer, appliance, electrical and electronic, infrastructure, etc. The main driving force for composite utilization are new and improved manufacturing processes, high volume production methods, materials development and optimization, design possibilities and economic benefits [3].

Composite materials are composed of two or more phases. If we generally talk about two-phase composites, one of the phases is appointed as the matrix phase and the other is designated as the dispersed phase. Commonly, when it comes to structural composites where mechanical strength is of paramount importance, the dispersed phase is called the reinforcing phase.

The matrix phase surrounds the dispersed phase, as schematically presented in Figure 1.1 (left). On the other hand, the dispersed phase can be in the form of particles, flakes, whiskers, short or discontinuous fibers, and is usually made of stronger, harder and stiffer material as compared to the matrix. In some cases, the dispersed phase can be from a material that gives specific properties, for example high thermal or electrical conductivity.

Common classification of composites is by the type of the matrix, which can be metal, ceramic or polymer. Of the aforementioned, the polymer-matrix composites are the most prevailing and are also the focus of this thesis. They represent about 90 % of all composites,

according to Strong [2]. The important features of the matrix are to bind together the dispersed phase and to hold it in a proper spatial arrangement, to give shape to the structure/product, to protect particles/fibers from mechanical and environmental damage and to help transmit the load to the reinforcement. An example of PMCs formation is shown in Figure 1.1 (right), where short or discontinuous fibers are bound together with the polymer matrix to form a composite material. The overall properties of the composites depend on the properties of the matrix and the dispersed phase(s), their relative amounts and spatial arrangement, manufacturing process and conditions during manufacturing. Although the final properties are a result of the interaction between individual constituents, some properties are either dominated by the matrix, for example toughness, or by the dispersed phase, e.g. thermal conductivity.

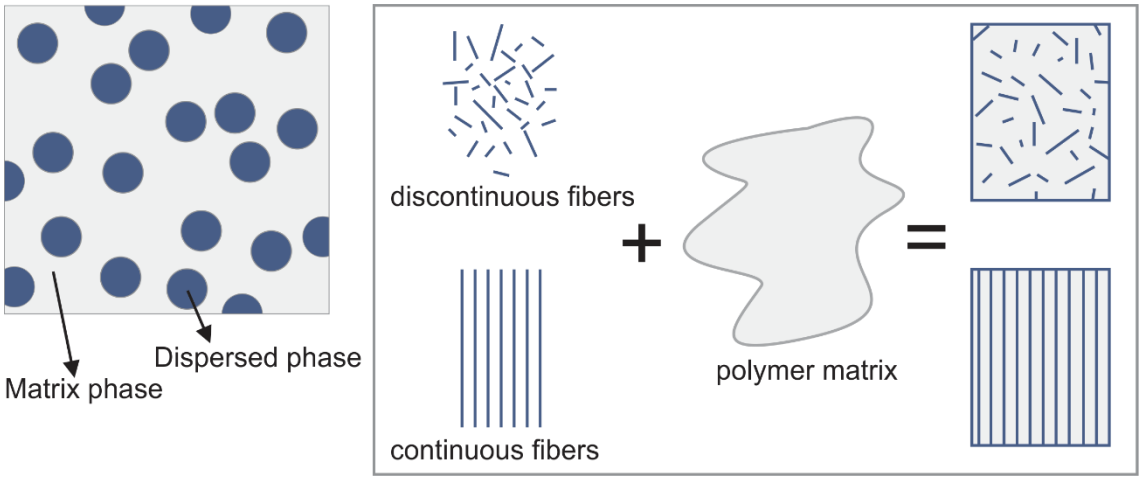


Figure 1.1: Schematic representation of two-phase composite material (left). The matrix phase and the dispersed phase are different in chemical composition. Formation of the polymer-matrix composite (right). Fibers of various lengths are bound together with the polymer matrix to form a composite material. Adapted from [4].

1.1.1 Polymer-matrix composites

PMCs consist of a polymer matrix and dispersed or reinforcing phase(s). The reinforcement is usually in the form of fibers (glass, carbon, natural, etc.), thus they are in general appointed as fiber-reinforced composites (FRCs). An overview scheme of FRCs is presented in Figure 1.2, where the main constituents of FRCs are listed, i.e. matrix, reinforcement, fillers and additives.

The matrix can be based either on thermosetting resin including epoxy, polyester, vinyl-ester or on thermoplastic resin such as polyester, polyamide, polypropylene and polyether-ether ketone. Thermoset resins undergo chemical reaction during processing crosslinking or curing, in which the adjacent molecules in the polymer chains crosslink through covalent bonding and form a complex three-dimensional amorphous structure. The crosslinking reaction of a thermoset polyester is an irreversible reaction (described in more detail in Chapter 1.2.1.1), thus upon heating, the material only burns and eventually degrades as in contrast to thermoplastics that can be re-melted and re-processed. This characteristic hinders suitable recycling routes for thermosetting polymers and composites as discussed in Chapter 2.2 [5].

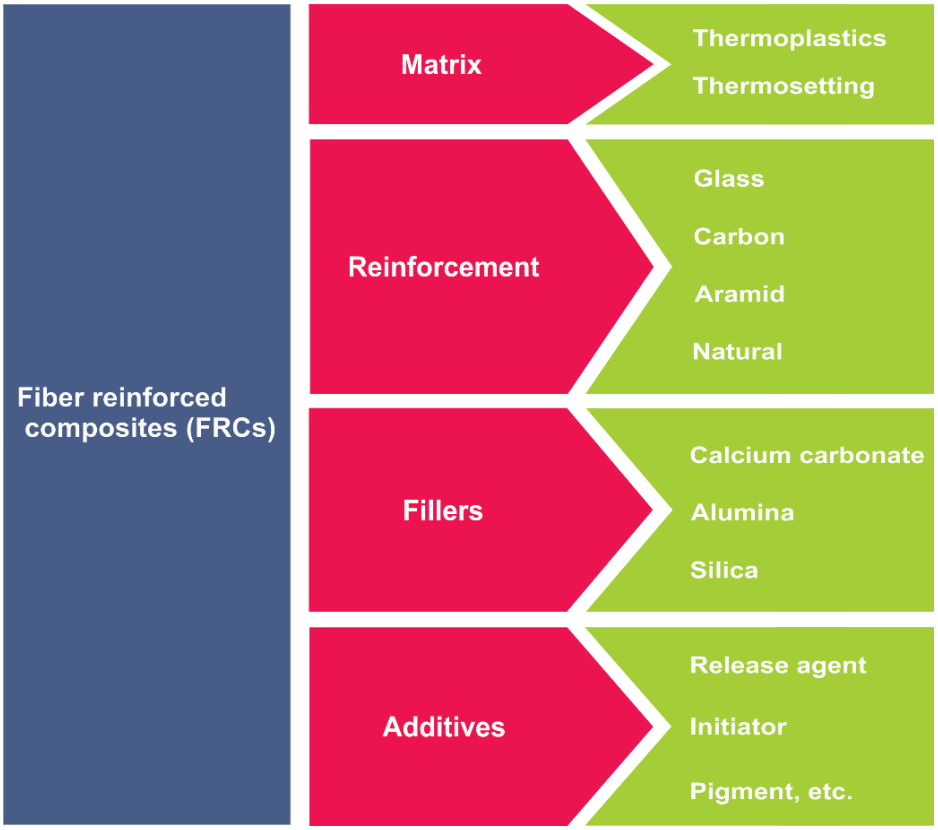


Figure 1.2: An overview of FRCs. Redrawn from [6].

PMCs are divided into two groups, i.e. advanced composites and engineering composites. Advanced composites are mainly used in aerospace and aircraft industry as well as in high performance sporting goods such as bike frames and tennis rackets. They are a combination of continuous or long[1] fibers, for example carbon fibers, and polymer matrix, e.g. epoxy resin, with higher thermal stability, which all contributes to superior mechanical and thermal properties. On the other hand, the reinforcing phase in engineering composites is in the form of shorter[2] length fibers, commonly glass fibers, that yield lower mechanical properties as compared to advanced composites.

1.1.1.1 Composites - replacement for metals

PMCs are a favorable substitute for traditional materials, like steel and aluminum (Al), in many industrial areas, especially in automotive, aerospace, electrical and appliance industry. Their potential to replace metals arises from design flexibility, easy processing, dimensional stability, corrosion resistance, lower weight, lower thermal expansion, high strength and stiffness, UV resistance and good electrical insulation. In Figure 1.3 a comparison between steel, Al and PMCs in some important properties is shown.

[1] Long fibers are defined as those having a length of 10–75 mm [6].
[2] Short fibers are identified as fibers with lengths from 3–10 mm [6].

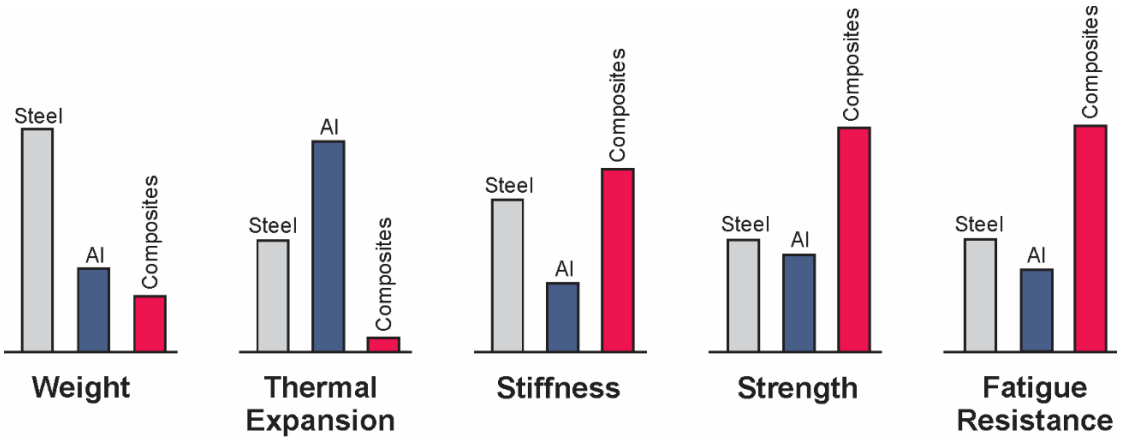


Figure 1.3: Comparison between metals and polymer-matrix composites. Composites have lower weight, lower thermal expansion and higher strength, stiffness and fatigue resistance as compared to steel and Al. Adapted from [7]. Stiffness of a material is defined as a measure of resistance to deformation in response to the applied force. Fatigue resistance is the tendency of a material to fracture or fail under cyclic loading (bending, axial or torsional).

High specific strength and stiffness, i.e. strength to density ratio and stiffness to density ratio, of PMCs results in much lighter materials as compared to metals. This leads to weight saving and subsequently to increased fuel efficiency and cost saving. According to [4] replacement of steel with PMCs in structures and components can save 60 to 80 % in weight and 20–50 % when replacing Al parts. A comparison between specific strength and specific modulus of some traditional materials with plastics and PMCs is presented in Table 1.1.

Furthermore, design flexibility and processing techniques enable that a composite part can be made in one piece. This reduces the manufacturing cycle time, assembling time and subsequently lowers the cost due to fewer or no fasteners and by eliminating additional machining operations.

On the other hand, constraints of PMCs are environmental aging initiated by matrix cracking, temperature and chemical/solvent resistance. They are all limited by the properties of the polymer matrix. For instance, average working temperatures for polymers are <100 °C for thermoplastics , ~150 °C for thermosets and for high temperature polymers such as epoxies, bismaleimides, polyphenylene sulfide and Teflon up to ~250 °C [4].

Table 1.1: Comparison of properties of some traditional materials and PMCs. Adapted from [4].

Materials	Density (g/cm^3)	Tensile modulus (GPa)	Tensile Strength (GPa)	Specific Modulus (GPa cm^3/g)	Specific Strength (GPa cm^3/g)	Maximum Service Temp. ($^{\circ}C$)
Metals						
Cast iron, grade 20	7.0	100	0.14	14.3	0.02	230-300
Steel, AISI 1045 hot rolled	7.8	205	0.57	26.3	0.073	500-650
Aluminum 2024-T4	2.7	73	0.45	27.0	0.17	150-250
Polymers						
Nylon 6/6	1.15	2.9	0.082	2.52	0.071	75-100
Polypropylene	0.9	1.4	0.033	1.55	0.037	50-80
Epoxy	1.25	3.5	0.069	2.8	0.055	80-215
Short fiber composites						
Glass-filled nylon (35%)	1.62	14.5	0.20	8.95	0.12	75-110
Glass-filled polyester (35%)	2.00	15.7	0.13	7.25	0.065	80-125
Glass-filled epoxy (35%)	1.90	25	0.30	8.26	0.16	80-200
Unidirectional composites						
*S-glass/epoxy (45%)	1.81	39.5	0.87	21.8	0.48	80-215
Carbon/epoxy (61%)	1.59	142	1.73	89.3	1.08	80-215
Kevlar/epoxy (53%)	1.35	63.6	1.1	47.1	0.81	80-215

* S stands for high strength.

1.2 Bulk Molding Compounds

The production of Bulk Molding Compounds (BMCs), together with Sheet Molding Compounds (SMCs)[3], reached 265 kilotons in Europe in 2015 [8]. The preferred area of BMCs application is electrical and electronic industry which comprises about 45 % [8] with a products range from switches and parts of switches, connection boxes, and components for electrical motors, such as housings, brush holders, yokes and armature shaft insulators. The second biggest area for BMC application is the automotive industry, occupying roughly 40 %. Common products are headlamp reflectors and under-the-hood components. Typical applications are also found in consumer, appliance and construction industry (see Figure 1.4 for an example).

[3] SMCs are similar to BMCs in their composition. However, SMCs contain longer fibers and have higher strength than BMCs. SMCs are commonly manufactured by press-molding.



Figure 1.4: An example of the product from the BMC composite for automotive industry.

1.2.1 Composition

BMC materials are a mixture of polymer resin, additives, fibers and mineral fillers. The manufacturing process of BMC starts by blending together all the liquid components, i.e. polymer resin, cross-linking agent, initiator and other functional additives, to obtain a liquid premix, see Table 1.2 for a more detailed composition. In the next step, the fibers and fillers are added to the mixture and homogenized. The resulting compound is in the form of dough-like material which is packed in gas-tight bags and stored under controlled conditions (e.g., stored at 18 °C to 20 °C with a service lifetime of 3 months) until the molding in order to avoid any changes during transport and storage, such as premature curing. The formulation can be adapted to a specific application in order to achieve the required properties.

During the manufacturing of BMC parts, the most frequently used diluent and cross-linking agent, styrene, evaporates from the material, which may lead to styrene emissions in the working environment and can have a negative effect on the health of the employees. Therefore, special care must be given to establish appropriate working conditions and to control styrene emissions. This topic is discussed in more detail in Chapter 2.

Table 1.2: Typical formulation of BMCs, based on a polyester matrix. From [9].

Component	wt%
Polyester resin	17.7
Styrene monomer	3.6
Initiator (t-Butyl perbenzoate)	0.2
Release agent (Zinc stearate)	1.1
Filler ($CaCO_3$)	57.4
Glass fibers	20.0

1.2.1.1 Unsaturated polyester resin

Polyesters are the most commonly used thermosetting resins in the production of BMCs. Unsaturated polyester (UP) is produced by the condensation reaction or polyesterification between unsaturated acids and anhydrides or diols as shown in Figure 1.5. During the reaction the water is eliminated. The double carbon-carbon bonds in the backbone present reactive sites for the cross-linking.

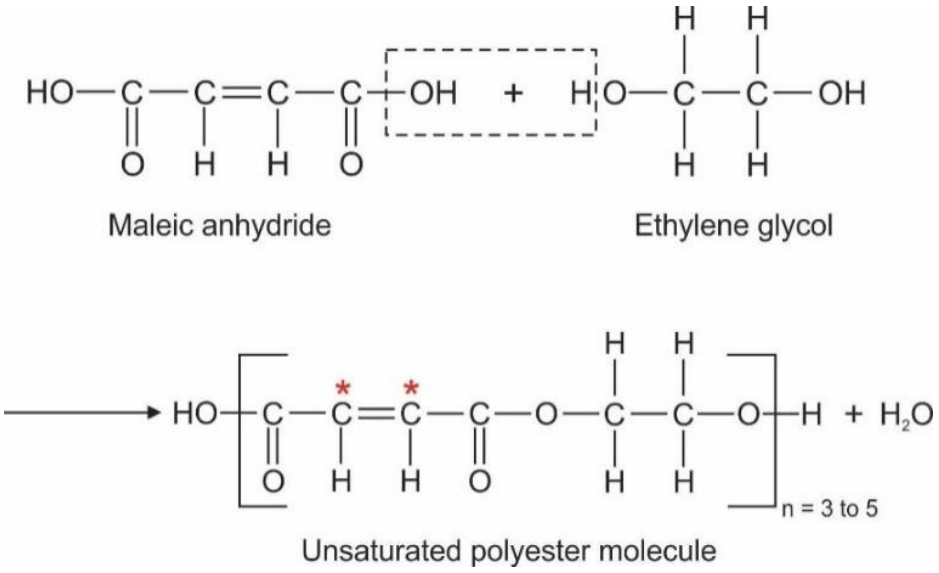


Figure 1.5: Synthesis of an unsaturated polyester molecule by condensation reaction. The sign * indicates unsaturated sites for the cross-linking reaction. Adapted from [10].

The synthetized UP resin is then dissolved in a reactive diluent, usually styrene. The latter is added to reduce the viscosity of the polyester resin and to enable good wetting of the reinforcing fibers. Furthermore, it also acts as a crosslinking agent.

UP resin is cured by 3-step free radical polymerization [11], most often activated by heat:

1 Initiation: Begins with the molding process. The initiator, i.e. organic peroxide, is activated by heat. It decomposes and forms free radicals at carbon-carbon double bonds in polyester chain.
2 Propagation: The styrene monomer reacts with free radicals creating links between adjacent polyester chains. As the reaction proceeds, the chain network is growing until there are no more styrene monomers. The molecular weight and the viscosity of the resin are increased.
3 Termination: The reaction stops when there are no more reactive sites for the cross-linking. The final material is polyester-styrene copolymer with a highly interconnected structure as shown in Figure 1.6.

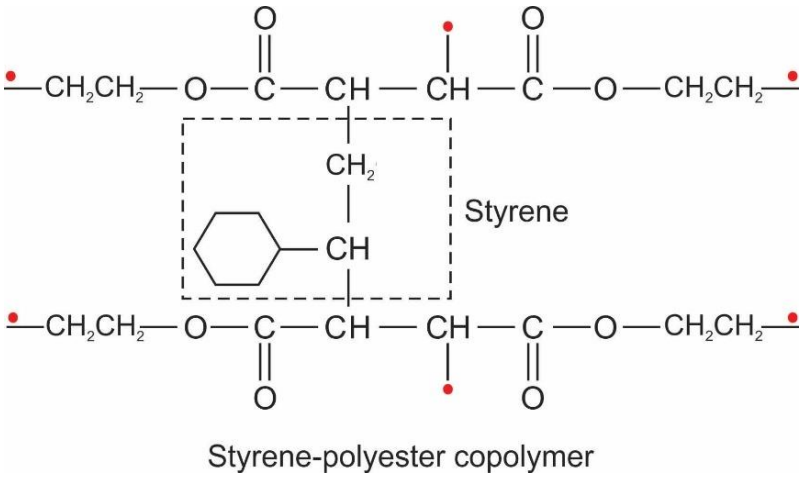


Figure 1.6: Chemical structure of a cross-linked polyester with styrene monomer [11].

The cross-linking behavior of the molding compound can also be represented by the viscosity profile of the resin as shown in Figure 1.7, where two processes overlap, i.e. thinning and crosslinking of the resin [2]. At room temperature, the thermoset resin is liquid but when the temperature is increased, the resin becomes less viscous due to softening and moving of molecules, represented by the blue line. On the other hand, further heating activates the curing reaction. The formation of cross-links between molecules increases the viscosity of the resin and as it passes the gel point, the polymer becomes a solid structure, i.e. it is cured, represented by the green line. The red line represents the combination of both processes.

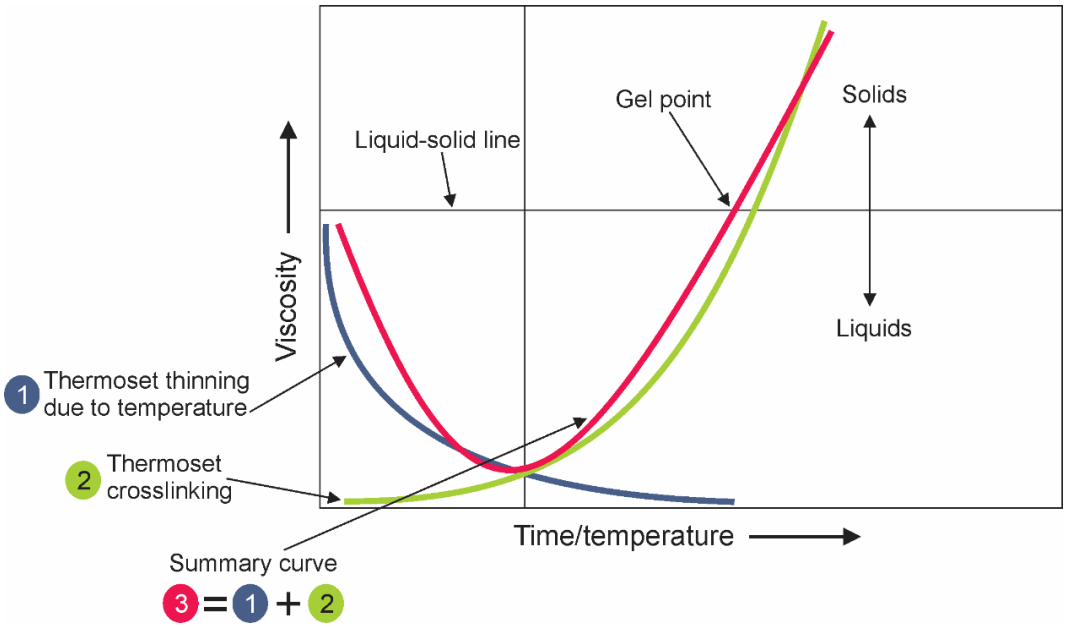


Figure 1.7: Change of viscosity during the cross-linking of a thermoset molding compound. The combination (red curve) of the thinning (blue curve) and crosslinking (green curve) process is what is actually happening in the mold cavity during the manufacturing of PMCs. After [2].

1.2.1.2 Glass fiber reinforcement

Glass fibers with initial lengths between 4 mm and 12 mm are typically used as reinforcement in BMCs. Their content is usually in the range from 15 % to 20 %, however it depends on the desired final properties.

Glass is an amorphous material composed mainly of silica (SiO_2) and different oxides (e.g. Al_2O_3, MgO, Na_2O). Glass fibers are manufactured by the fiber-spinning process, in which the melt is extruded to form the filament that is further chopped to the desired length. Types of glass fibers slightly differ in composition (see Table 1.3), for example C-glass fibers with high resistance to chemical corrosion, high strength S-glass fibers or electrical grade E-glass fibers that are the most commonly used fiber type in BMCs.

E-glass fibers ("E" stands for electrical) are a general-purpose fiber type, they have high strength and are low cost. Because of the low alkali content (2 %) they have very stable electrical properties and are good electrical insulators. Their properties are listed in Table 1.4.

Table 1.3: Typical composition of different types of glass fibers [7].

Composition (wt%)	E-glass fibers	C-glass fibers	S-glass fibers
SiO_2	55.2	65.0	65.0
Al_2O_3	8.0	4.0	25.0
CaO	18.7	14.0	-
MgO	4.6	3.0	10.0
Na_2O	0.3	8.5	0.3
K_2O	0.2	-	-
B_2O_3	7.3	5.0	-

Table 1.4: Properties of E-glass fibers.

Density (g/cm^3) [7]	2.55
Tensile strength (GPa) [4]	3.45
Tensile modulus (GPa) [4]	70
Elongation at break (%) [4]	4.8
Coefficient of thermal expansion ($°C^{-1}$)[2]	5.2×10^{-6}
Dielectric strength (kV/cm) [2]	103
Softening point (°C) [2]	846
Specific heat at room temperature (kJ/kgK)[2]	0.810
Thermal conductivity (W/mK) [12]	1.2-1.35

1.2.1.3 Mineral fillers

BMCs are highly filled with mineral fillers, even up to 80 wt%. The primary function of the mineral filler in the compound is to modify the viscosity of the resin-glass fiber mixture in order to prevent the segregation of individual components. Addition of mineral fillers improves dimensional stability of the molded parts, increases the modulus, improves heat transport [13] and consequently enables faster molding cycles, improves surface appearance and gives self-extinguishing properties. Furthermore, it lowers the overall cost of the material because it is the cheapest component in the compound. Calcium carbonate

($CaCO_3$) is the most commonly used filler, see Table 1.5 for properties. Another common filler, aluminum hydroxide, $Al(OH)_3$, also acts as a flame retardant.

Table 1.5: Properties of $CaCO_3$ [14].

Density (g/cm^3)	2.65
Mohs hardness	2.5-3
Modulus (GPa)	179
Coefficient of thermal expansion ($°C^{-1}$)	10×10^{-6}
Dielectric constant	6.14
Thermal conductivity (W/mK)	5.6

1.2.1.4 Additives

Various additives are added to the compound, usually in small amounts, in order to meet specific requirements during the molding process or to achieve the desired final properties of composite material. The main additives and their use are given in Table 1.6.

Table 1.6: List of the main additives in the production of BMCs.

Additive	Function
Low profile additive	to reduce post-curing shrinkage and to improve surface finish; thermoplastic in amount of 2 to 5 wt%, such as vinyl acetate or polystyrene [15]
Initiator	degrades at a specified temperature and transforms polyester and styrene molecules into free radicals and therefore induces crosslinking; usually organic peroxide [16]
Inhibitor	added to prevent polymerization for a certain period of time; loss of styrene or slow decomposition of initiator can cause premature curing, therefore the inhibitor extends the storage life of the molding compound [16]
Release agent	or lubricant; forms a thin oily film in the mold surface in order to facilitate removal of the product from the mold; materials with a low melting point, such as calcium or zinc stearate [16]
Pigment	gives color to the compound; powder or pigment paste

1.2.2 Processing methods

Injection molding is the most frequently used manufacturing technique for BMCs. The process is schematically presented in Figure 1.8. During the molding process the compound is fed into a barrel and with a screw type plunger forced into the mold cavity which is heated to around 140 °C to 160 °C. Under heat and pressure the material cures and takes the shape of the mold. Afterwards the mold opens and the part is ejected. The mold closes and the manufacturing cycle is repeated. Injection molding is preferably used for mass production of complex shaped components since it enables fast cycle times and the possibility of multi-cavity molds.

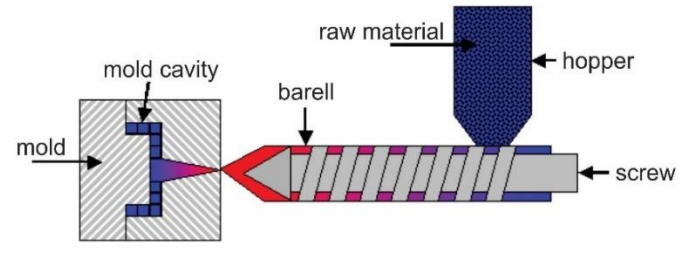


Figure 1.8: Injection molding process. Adapted from [17].

Another widely used processing technique for BMCs is transfer molding (see Figure 1.9). In this process the raw material is weighed, preheated and placed into a pot. Then the material is pressed into a heated mold cavity through a sprue channel. The material fills the mold and solidifies.

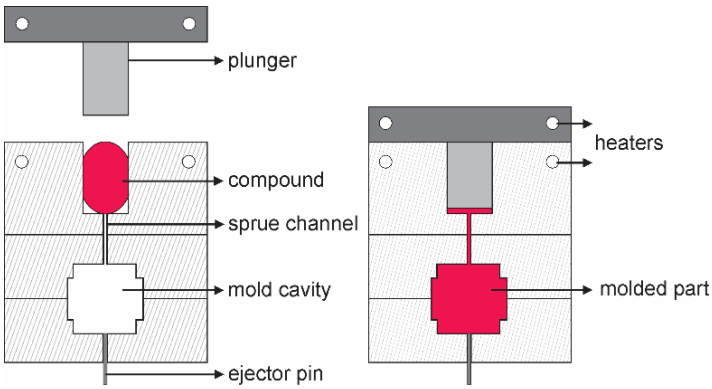


Figure 1.9: Transfer molding process. Adapted from [18].

1.3 Microstructure

The properties of FRCs are influenced by the microstructure. As represented in Figure 1.10, the main factors that characterize the microstructure of FRCs are fiber content, length, shape, distribution and orientation. Furthermore, the microstructure is influenced by the technological process, i.e. molding process, molding conditions and the geometry of the mold cavity [19, 20, 9].

In this section we describe some of the influencing factors which were of interest in the present work, i.e. *fiber content*, *fiber distribution* and *fiber orientation*.

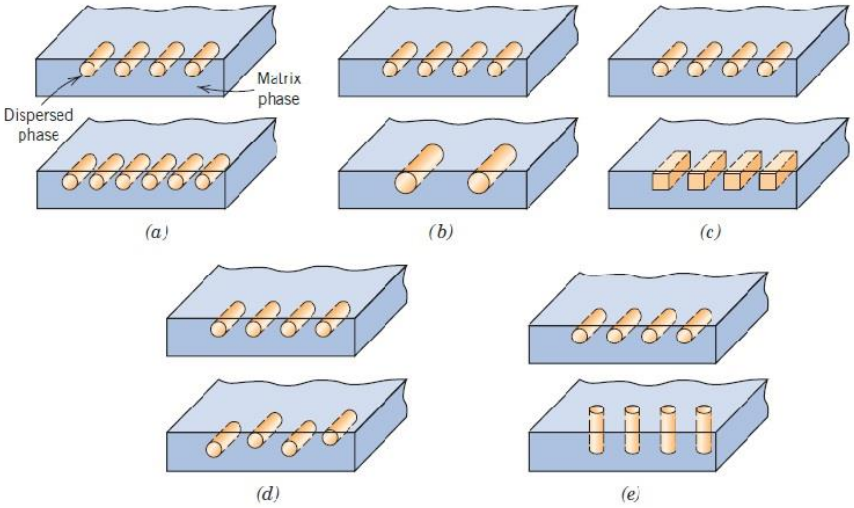


Figure 1.10: Different spatial arrangements and characteristics that determine the properties of fiber-reinforced polymer-matrix composites: a) concentration, b) size, c) shape, d) distribution, e) orientation. From [22].

1.3.1 Fiber content, distribution and orientation

Fiber content in FRCs is usually expressed as volume (V_f) or weight fraction (wt) and has the greatest influence on the mechanical properties, such as tensile and flexural strength, as discussed later in Chapter 1.4. Fiber damage that occurs during manufacturing due to the fiber-fiber, fiber-matrix and fiber-mold cavity interactions is strongly related to the fiber content.

The fiber orientation in FRCs is governed by the manufacturing process, such as injection or compression molding as well as by the shape and thickness of the mold cavity [23, 24]. BMC product may have areas with preferred orientation of fibers and areas with randomly oriented fibers forming a complex microstructure. Local variations in fiber orientation can be found throughout the molded part, e.g. from skin to core layer in injection-molded fiber-reinforced composites [25, 19]. The orientation and distribution of fibers depend on the complexity of the shape of a real part and are induced by the profile of the shear flow (found at the mold walls) or extensional flow (found at the flow front of the compound), aligning fibers parallel or perpendicular to the filling flow direction, respectively [26]. In a simple mold geometry, for example in test specimens defined by ISO standards, a high alignment of fibers is achieved, as schematically presented in Figure 1.11. In this case, a high shear flow induces a preferred alignment of fibers in the filling flow direction [27].

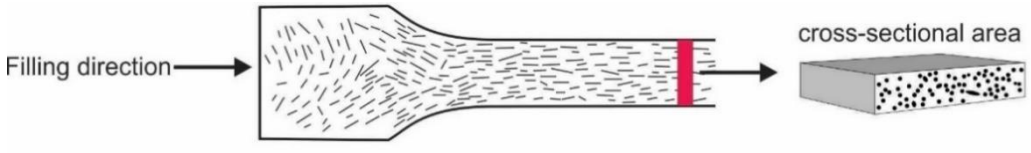


Figure 1.11: Shematic representation of fiber orientation in the test specimen. During the molding process, the fibers tend to align parallel with the filling flow direction.

Figure 1.12 represents two possible extremes in fiber orientation of discontinuous FRC – totally parallel alignment and truly random orientation of fibers. In the latter case the properties of the material are isotropic, meaning they are independent of the direction of measurement. For example, as compared to unidirectional long fiber-reinforced composites, the properties are anisotropic and dependent on the direction of measurement. Accordingly, the strength and stiffness of the composite is higher in the longitudinal direction to which the most fibers are oriented and weaker in the transverse direction.

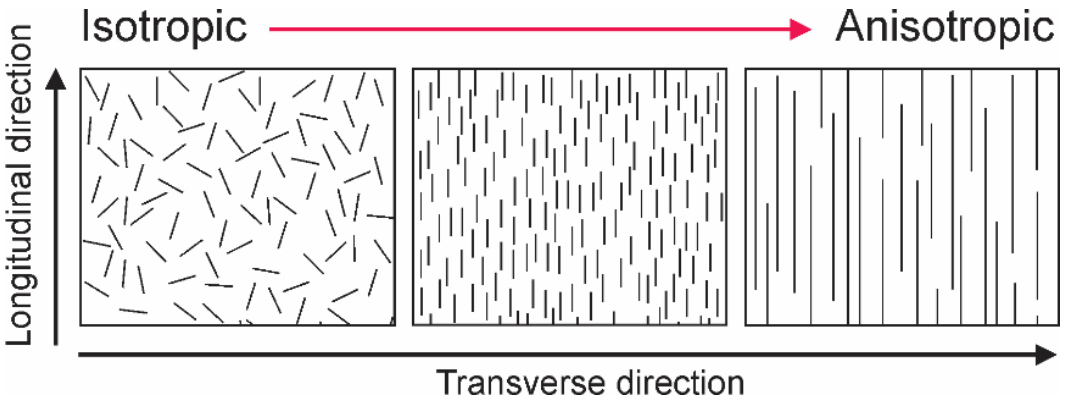


Figure 1.12: Representation of different orientations in FRC (from the left side): discontinuous and randomly oriented, discontinuous and aligned, continuous and aligned. Redrawn after [22].

Fiber orientation in composites can be experimentally determined and statistically described by different methods [28–30], most commonly with fiber orientation tensors. The easiest way to determine fiber orientation is by analyzing the micrographs of composites' polished cross-sections, although such analysis has some limitations, for example it does not enable determination of a three-dimensional fiber orientation. The fiber surface intersections in the material are visible as circles (when cut perpendicular to the fiber length) and as ellipses when the fibers are oriented at different angles. Figure 1.13 shows a typical microstructure of a BMC composite where the cross-sections of some fibers are encircled in red.

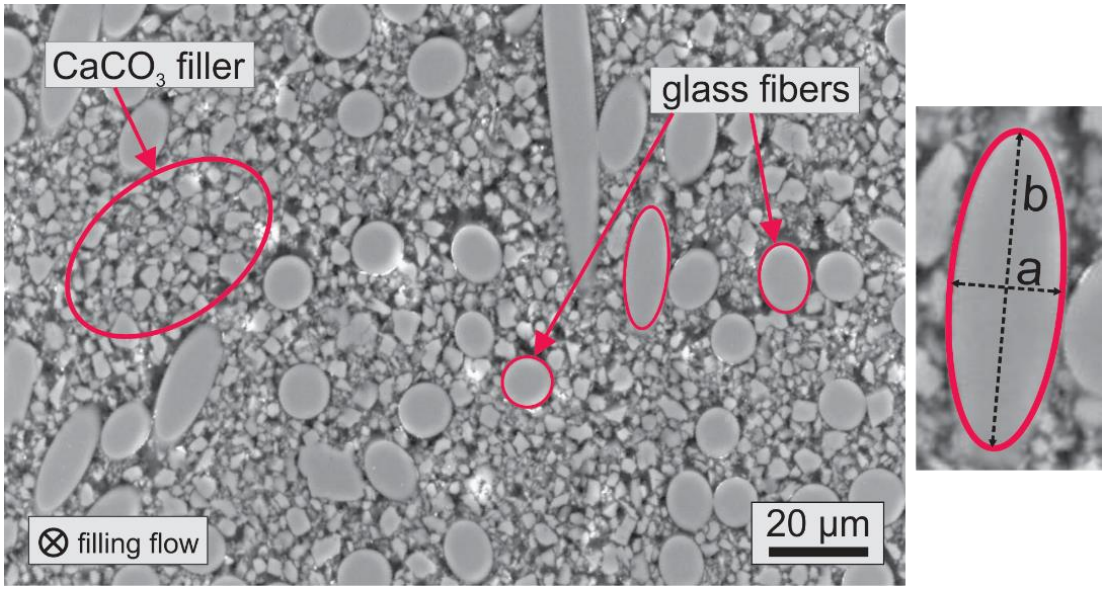


Figure 1.13: SEM micrograph of the polished cross-section of a BMC composite containing 20 wt% of EGFs. The glass fibers are surrounded by the particles of the $CaCO_3$ mineral filler distributed in the polymer matrix. The glass fiber intersections, marked with red, can be easily identified from the micrograph. By measuring the axes of the circles and ellipses, the fiber orientation parameters can be determined.

1.3.2 Characterization of composite microstructures

In order to characterize and quantitatively describe the microstructures of composites, the data from the image analysis of the micrographs is extracted [31–34] and further used to construct spatial tessellations or to generate statistical functions and descriptors. These also include the Voronoi diagram analysis and radial distribution function (RDF), which are described in this section and were found useful in the present work.

1.3.2.1 Voronoi diagram analysis

The Voronoi diagram method, named after the Russian mathematician Georgy Voronoi (1868–1908), also commonly known as the Dirichlet tessellation, involves partitioning a plane into cell areas known as Voronoi polygons [35–37]. The Voronoi diagrams are constructed from a number of points (N_i) in a plane, where every polygon is assigned to a given point N and occupies a region, i.e., a convex polygon[4], around a selected point, allowing that all neighboring points are closer to the corresponding point than to any other point in the plane. See Figure 1.14 for an example of a Voronoi diagram. Formal definition of a Voronoi diagram [35] is summarized in Appendix A.

[4] In a convex polygon all the interior angles are less than or equal to 180°.

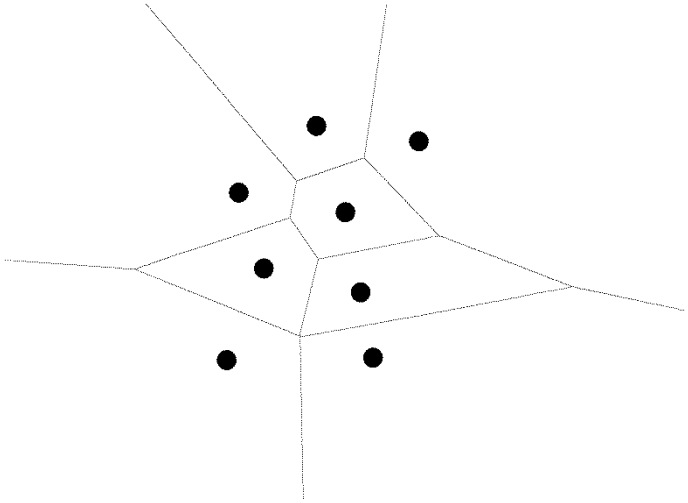


Figure 1.14: An example of a Voronoi diagram constructed from eight points.

The Voronoi diagram method gives quantitative information about the spatial distribution of objects/points and is used in many areas, such as in geography, territorial behavior of animals and transportation. More examples can be found in [38–41].

Several papers report the correlation of the microstructural analysis, based on Voronoi tessellations, with the processing and properties of materials. Furthermore, the Voronoi diagram method was found useful in quantifying the level of homogeneity of the second-phase distribution in composites [42–46].

For example, Sun and co-workers [47] characterized the structure of sisal fibers, analyzed the polypropylene matrix (PP) crystallinity and made a comparison in distribution between sisal fibers in the PP matrix by means of the Voronoi method. The fibers were used as received or treated with aminopropyltriethoxysilane. The effect of the coupling agent, maleated polypropylene (MAPP), was also investigated. Both the fiber treatment and the MAPP addition contribute to a more uniform distribution of the fibers in the PP matrix and to a higher tensile modulus.

Figure 1.15 shows Voronoi diagrams generated from the microstructures of two differently processed unidirectional carbon fiber composites – manufactured without or with the consolidation pressure upon curing, respectively denoted as Material 1 and Material 2. It is apparent that the distribution of the fibers in Material 2 is more homogeneous than in Material 1 where some areas depleted in fibers are found. Furthermore, the relation between the polygon area size and the number of polygon sides (see Figure 1.15, bottom) shows that the polygon mean area size is increasing with the number of polygon sides for both materials. However, in the composite exhibiting an inhomogeneous fiber distribution there are more n-sided ($n = 7, 8, 9$) polygons found suggesting a higher probability of finding fibers being closer to each other in the material with a non-uniform fiber distribution [48].

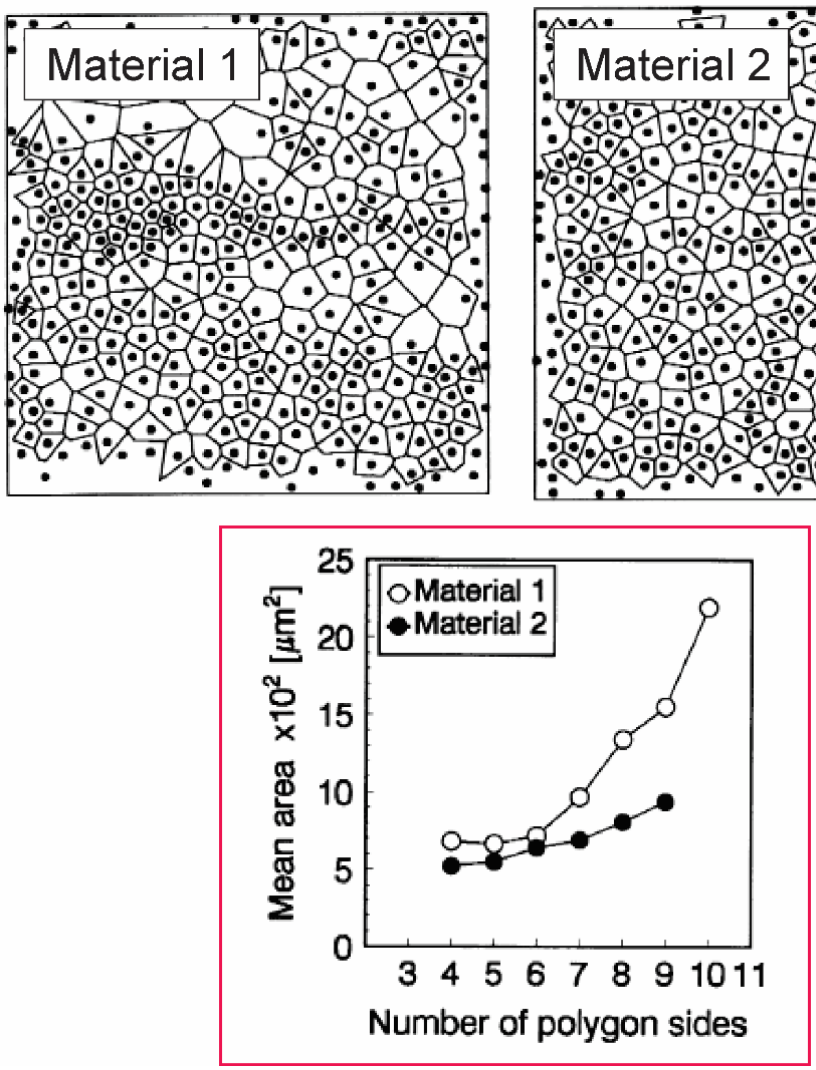


Figure 1.15: Comparison of two differently processed unidirectional carbon fiber composites. After [48].

Heijman et al. [42] applied the Voronoi analysis to a zirconia-toughened alumina composite in order to study the effect of different processing conditions on the level of microstructural homogeneity. From the statistical data they derived the homogeneity parameter HP_q (coefficient of variation):

$$HP_q = \frac{\sigma_q}{\mu_q} \tag{1.1}$$

where σ_q is the standard deviation, μ_q is the average value and q is a corresponding property, such as area (A), perimeter (l) or number of polygon faces (n). It applies that a smaller HP_q value indicates a greater level of the zirconia distribution homogeneity. The HP_q is dimensionless and has no upper limit. Figure 1.16 shows the Voronoi diagrams of the investigated composites. The HP_q derived from the area of Voronoi polygons (HP_A) indicates that the distribution of zirconia phase in the alumina matrix is the least homogeneous in the sample c), with the highest HP_A. Furthermore, the microstructural homogeneity was correlated to the wear rate (k_w, bottom line in Figure 1.16) of composites, where the latter sample had the lowest wear resistance (highest k_w).

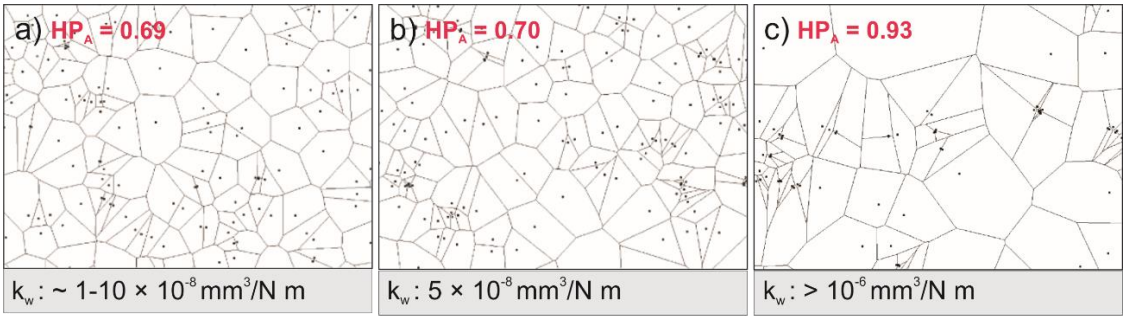


Figure 1.16: Voronoi diagrams of zirconia-toughened alumina composites prepared under different processing conditions. The homogeneity parameter derived from the area of Voronoi polygons (HP_A) indicates that the most uniform distribution of the zirconia phase is in the samples a) and b) (0.69 and 0.70, respectively) and the least in the sample c) (0.93), which also had the highest wear rate, k_W. Redrawn after [42].

Similarly, Trefalt et al. [43] studied the distribution of tetragonal zirconia particles (ZrO_2) in $Pb(Zr,Ti)O_3$ (PZT) ceramic composites using a Voronoi-diagram analysis. They compared the microstructure of PZT-ZrO_2 ceramic composites with surface modified and surface unmodified ZrO_2 particles in order to define the optimal conditions for achieving the most homogeneous distribution of ZrO_2 particles. From the parameters obtained from the Voronoi analysis, such as the size distribution of Voronoi polygons, one can detect and quantify clustering of second-phase inclusions in composites. Trefalt et al. concluded that the modified synthesis contributes to a more uniform distribution of ZrO_2 particles in the PZT matrix as compared to the non-modified synthesis. Figure 1.17 shows the microstructures and corresponding area size distributions of Voronoi polygons for both investigated PZT-ZrO_2 composites. The presence of large areas in the Voronoi polygon area size distribution of the composite prepared with the non-modified synthesis confirms clustering of ZrO_2 particles (Figure 1.17, right column).

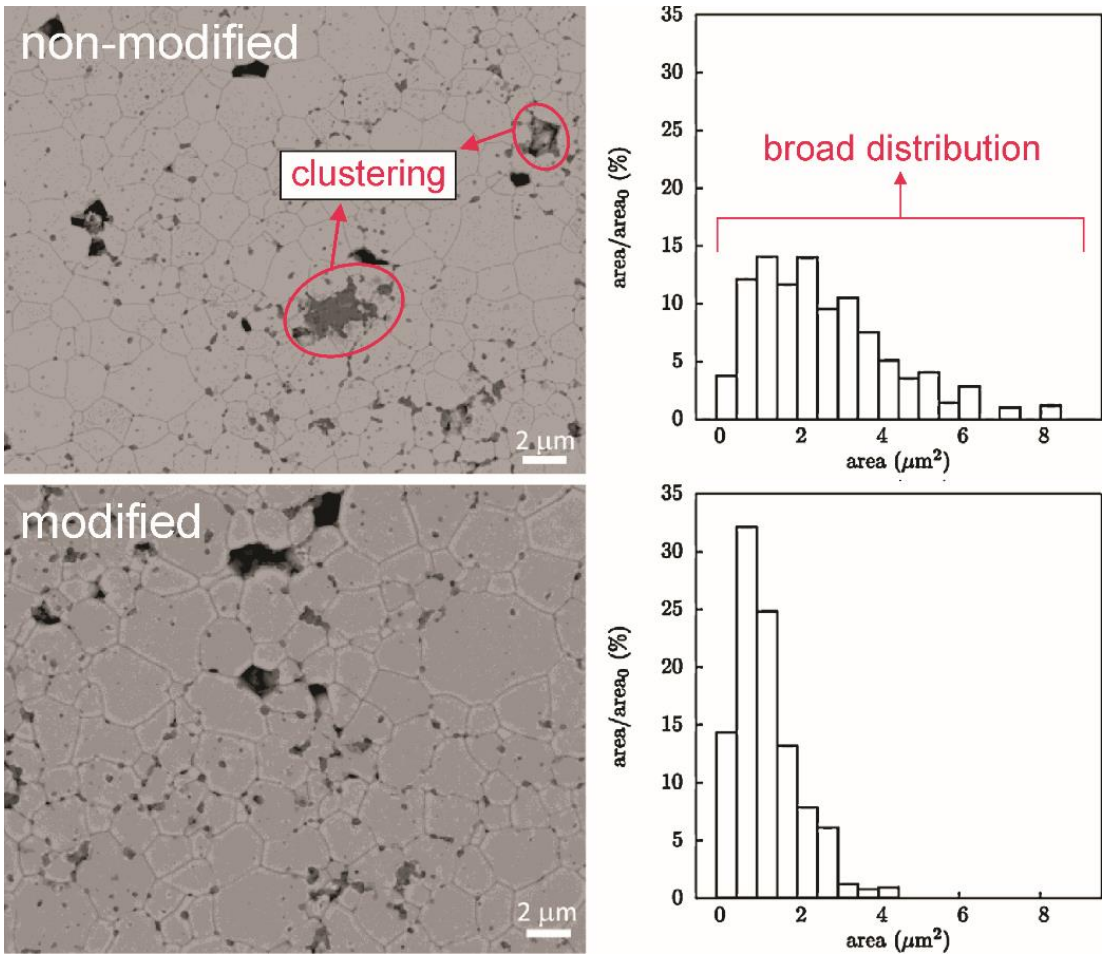


Figure 1.17: Microstructures of PZT-ZrO_2 composites prepared with the non-modified and modified synthesis. The area size distributions of Voronoi polygons show that modification of the synthesis contributes to a more uniform ZrO_2 particle distribution as compared to the composite prepared with the non-modified synthesis where large polygon areas indicate clustering of particles. After [43].

In order to classify and to better distinguish between clustered, random or ordered distributions of particles/second phases in the investigated composite, the data in the form of computer-simulated point-patterns serve as a comparison between different types of distributions.

As an example, Voronoi diagrams of the computer-simulated clustered and random (Poisson)[5] point patterns are collected in Figure 1.18 [45]. Clearly, for a clustered structure, the difference between the sizes of Voronoi polygon areas will be more pronounced and the size distribution will be broader. A high peak at smaller values and the presence of large polygon areas in the size distribution of Voronoi polygons indicate clustering (Figure 1.18, left column). It follows that for a random or more homogeneous distribution of points/particles respective Voronoi polygons will be more similar in size. Samardžija et al. [45] used clustered, random and ordered computer-simulated point patterns in order to

[5] Poisson process is the simplest stochastic mechanism for the generation of a random point pattern. Such point pattern serves as a standard for the determination of how much the observed distribution of particles/second phases in an investigated sample/microstructure deviates from the complete randomness [48].

evaluate the distribution of ZrO_2 particles in Al_2O_3 matrix. They made a comparison between the aforementioned simulated point-patterns and two differently prepared Al_2O_3-ZrO_2 samples. They concluded that simulated point-patterns and Voronoi-diagram analysis are found useful in evaluating and distinguishing between different types of the second-phase distribution.

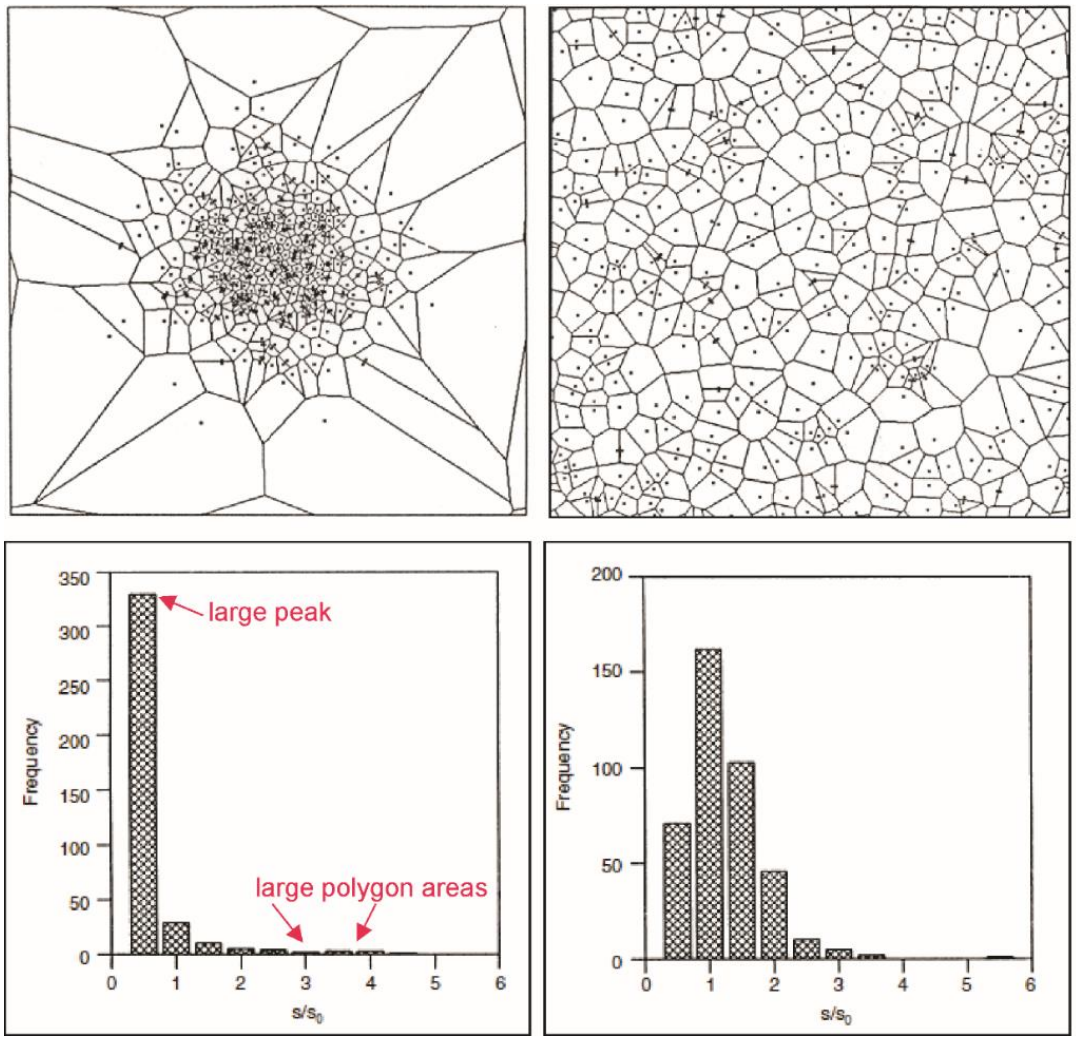


Figure 1.18: Voronoi diagrams of clustered and random computer-simulated point-patterns with the corresponding size distributions of Voronoi polygons. In the clustered point pattern, a high peak at smaller values and the presence of large polygons in the size distribution reflects clustering. Redrawn from [45].

1.3.2.2 Radial distribution function

RDF, which is essentially equal to the pair distribution function $g(r)$, is interpreted as the probability of finding a center of a particle in a shell (dr) at a specific distance (r) from the center of the reference particle [49, 48].

The principle of RDF and an example are presented in Figure 1.19. As shown in the histogram, the $g(r)$ equals zero at distances that are smaller than the minimal distance between two neighboring particles in the pattern. Afterwards, at a typical distance r, the first peak corresponds to the first shell. The sharper the peak, the more frequent and uniform are the distances between the reference particle and the neighboring particles.

Likewise, the second peak at a specific distance corresponds to the second shell, etc. Further on, at larger distances the peaks broaden and merge, indicating that the local variations in the particle density are faded away as r grows. The distance r, over which the RDF merges with the continuum, measures the extent of the local disorder [48, 50]. The RDF for a completely random distribution of particles (i.e. Poisson pattern) equals one, as marked in Figure 1.19 [48].

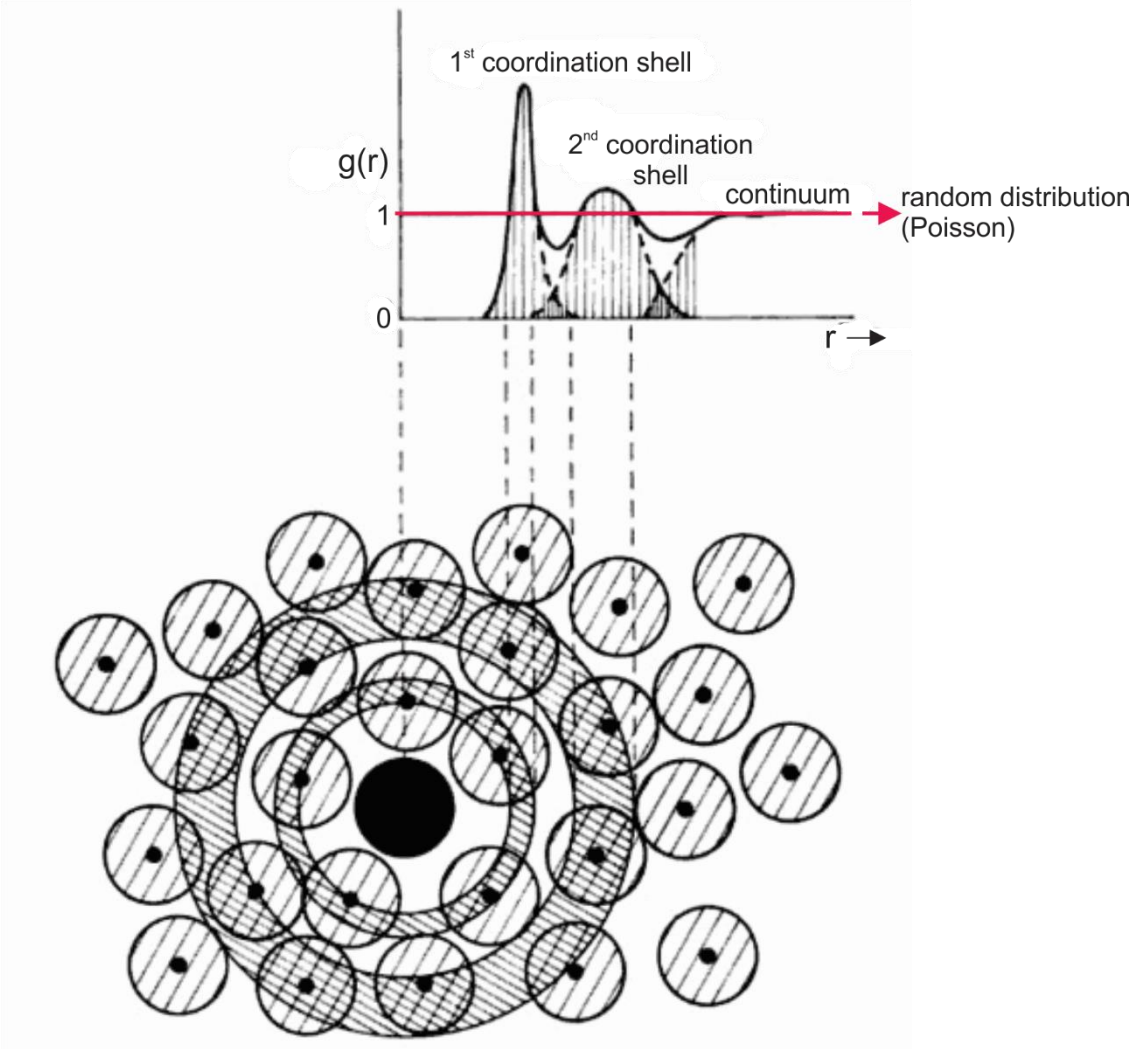


Figure 1.19: Radial distribution function is defined as the probability of finding a particle in a shell dr at a specific distance r from a certain "reference" particle (black marked circle). The particles in the first shell are accountable for the first peak, the particles in the second shell correspond to the second peak in RDF, etc. Redrawn from [50].

RDF can disclose geometrical features in a microstructure pattern. However, in order to get detailed information about the microstructure or about the arrangement of the second-phase particles in composites, a comparison of experimental and modeled RDFs is necessary. RDF was applied to describe modeled patterns (random, clustered) of the second-phase particles as well as microstructure patterns of real composites [46, 51, 52]. For example, Everett [51] determined the RDF of modeled random (Hard Core distribution

model[6]) composite microstructures with different fiber volume fractions (from 0.10 to 0.50) and RDFs of two microstructures of Nicalon/zirconia titanate composites with a high and low flexural strength, i.e. ~860 MPa and ~640 MPa, respectively. He concluded that the fiber density in random microstructures varies with the radial distance – it is higher near a specific fiber than farther away, as evidenced by a sharp peak (see Figure 1.20). At a higher volume fraction of fibers, the difference in RDF peak intensity increases. The RDF of both Nicalon/zirconia titanate (48 %) composites was found similar to RDF of random microstructures, however the RDF of the composite with a higher flexural strength was more consistent with the random distribution.

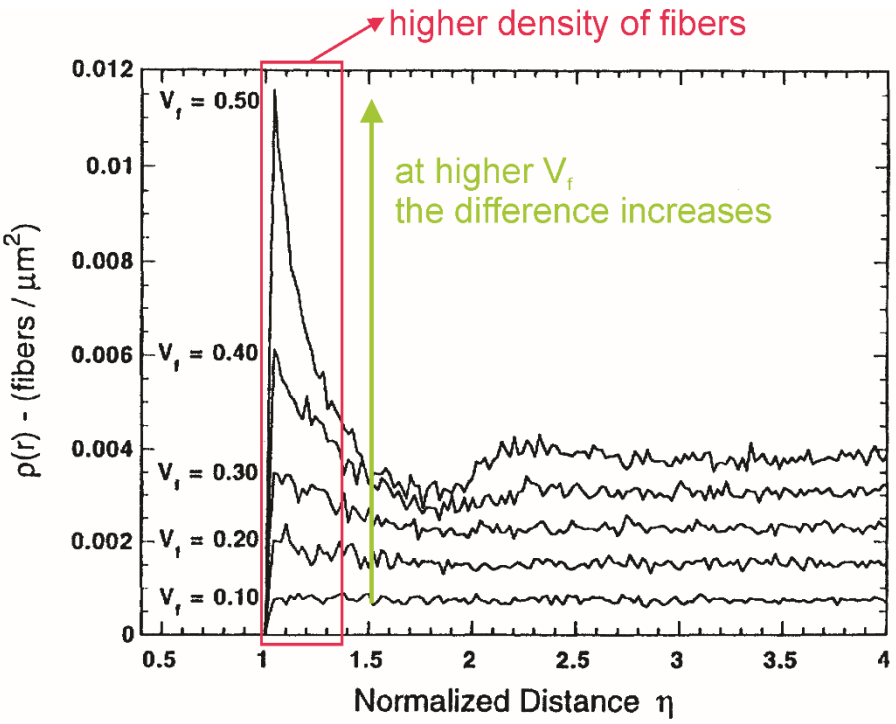


Figure 1.20: RDF of modeled random composite microstructures with different fiber volume fractions (from 0.10 to 0.50). The sharp peak indicates a higher fiber density at the distance of the closest approach. With increasing volume fraction of the fibers, the peak intensity increases. Redrawn after [51].

1.4 Influence of the Microstructure on Mechanical Properties of the Composites

Mechanical properties of the composites are strongly dependent on the properties of the fibers, matrix and fillers, their volume fractions, fiber length, orientation and distribution as well as adhesion between the fibers and the matrix [53–62].

S. Y. Fu et al. [55] studied the combined effect of the fiber volume fraction (8, 16, 25 vol%) and the mean fiber length on the tensile strength and modulus of polypropylene (PP) composites reinforced with short glass (SGF) and short carbon fibers (SCF) prepared by injection molding. Note that the carbon fibers exhibit much higher tensile strength

[6] Hard Core distribution model is a variation of the Poisson point process. In this model, the constraint of no overlapping of particles is taken into account as well as all the particles are contained within a region [46].

(3950 MPa) and modulus (238 GPa) than the glass fibers (1956 MPa and 78.51 GPa, respectively). The tensile strength of PP itself was 31.6 MPa. The addition of either fibers contributed to higher values of both tensile strength and modulus and the increase was much higher for the SCF, see Figure 1.21. The increase of the fiber fraction contributed to only a slight increase in the strength, but to a strong enhancement in the modulus, see Figure 1.21. The authors suggested that the tensile strength was less dependent on the fiber volume fraction than the tensile modulus. For both types of fibers, they observed that the mean fiber length decreased with increasing the fiber volume fraction (see Figure 1.21 c)) as a consequence of increasingly pronounced fiber damage. The SGFs were at all fractions longer than the SCF which was related to the more brittle nature of the former. They concluded that at high fiber contents the fiber damage almost nullifies their reinforcing effect.

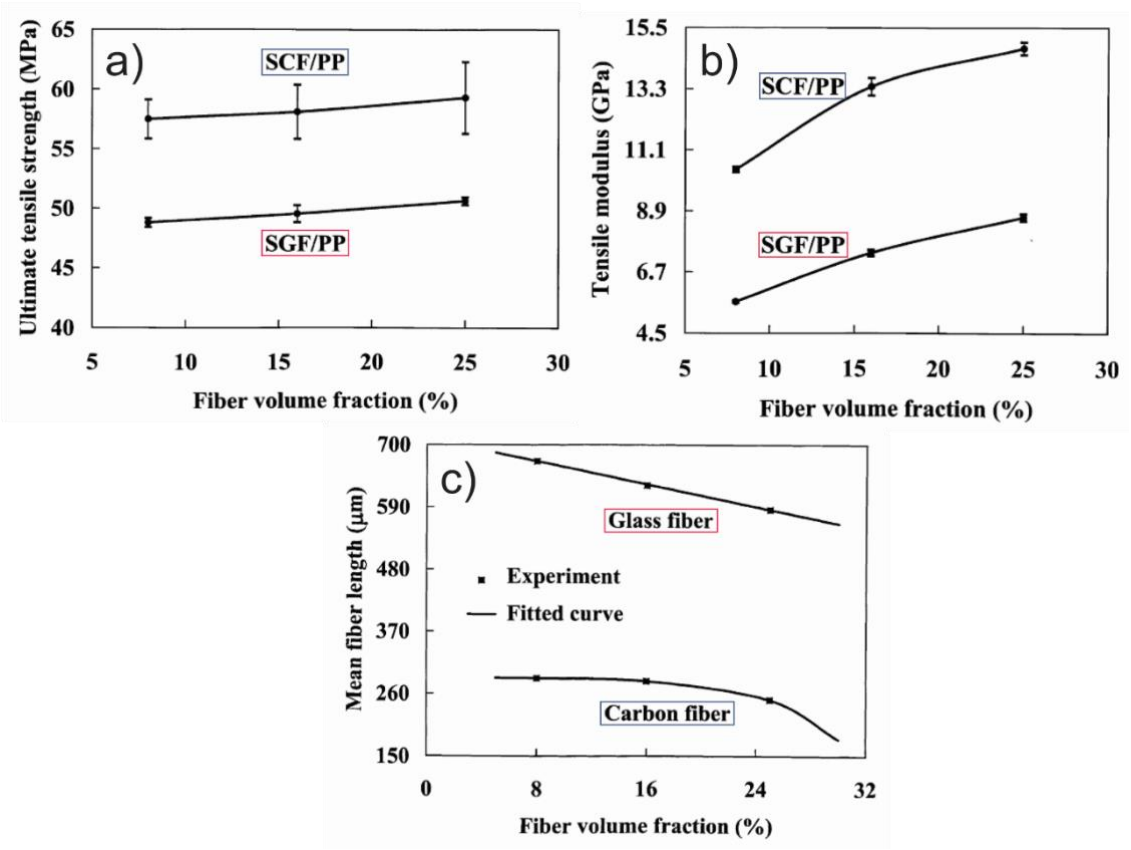


Figure 1.21: a) Tensile strength, b) tensile modulus and c) mean fiber length of the polypropylene (PP) composites reinforced with short glass (SGF) and short carbon fibers (SCF). The tensile strength only slightly increases with increasing fiber content, meanwhile the enhancement of the modulus with a higher fiber content is more pronounced. The mean length of glass and carbon fibers in the PP matrix decreases with increasing fiber content, which demonstrates greater fracture of the fibers during the molding process with increasing fiber fraction. Redrawn after [55].

Moreover, it has been observed that with increasing fiber content in the polymer matrix, the mechanical properties of the composites are improved only to a certain, optimum, fiber content [58, 61, 62].

Sreenivasan et al. [62] investigated mechanical properties of polyester matrix composites reinforced with randomly oriented natural fibers of a given length in the amounts from

10 wt% to 50 wt%. They observed that tensile strength, Young's modulus, flexural strength, flexural modulus and impact strength of the composites increase with increasing fiber content, achieving optimal values at 40 wt% of fibers.

Similarly, Thomason [58] demonstrated that in PP composites reinforced with glass fibers in fractions from 0 wt% to 73 wt% the tensile and flexural strength reached peak values at 40 wt% – 50 wt%, see Figure 1.22. Further decrease in mechanical strength was attributed to the reduction of fiber length at higher fiber contents.

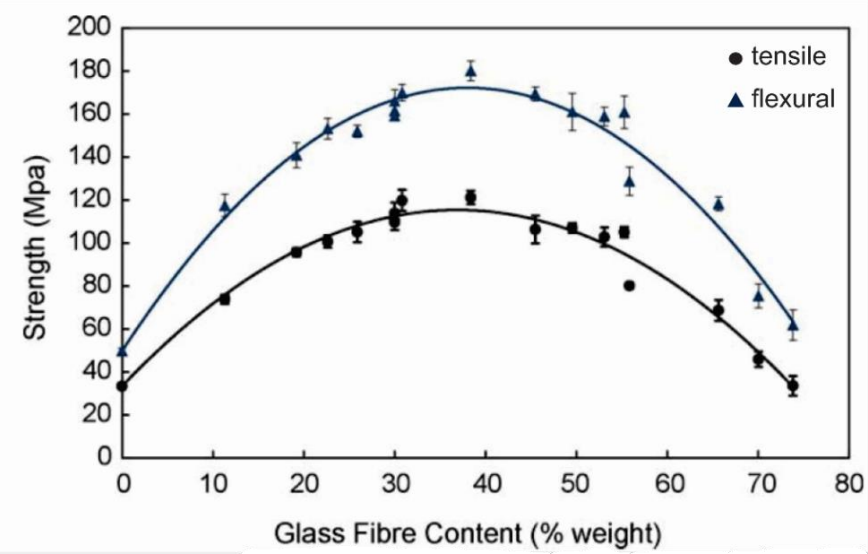


Figure 1.22: Tensile and flexural strenth of polypropylene (PP) composites reinforced with glass fibers. The highest tensile and flexural strength is achieved at fiber weight fraction of 40 %– 50 %. Redrawn after [58].

In the study of the effect of basalt fiber length (4/10/21/50 mm) and content (from 21 wt% to 71 wt%) on the mechanical properties (tensile, flexural and impact strength) of polyester-based composites Amuthakkannan et al. [61] found that the best combination of flexural and tensile properties is achieved at the fiber length of 10 mm and at 68 wt% of fibers. They observed voids due to fiber pull-out, fiber fracture and matrix-rich areas in the SEM micrographs of the fractured composites. The authors related the failure at fiber contents above the optimum to a weak adhesion between the fibers and the matrix and to inhomogeneous distribution of fibers.

A non-uniform fiber distribution can result in fiber clusters and fiber-depleted areas. Such microstructural diversity can lead to local variations in stress concentration that can result in deteriorated mechanical response of the material. Mishnaevsky Jr. et al. [63] investigated, numerically and analytically, the effect of particle arrangement (random uniform or clustered) in modelled microstructures of silicon carbide/aluminum matrix composites with different fractions of the dispersed phase. The probability of failure was higher in the microstructures with the clustered distribution of particles.

1.4.1 Influence of the microstructure on dynamic mechanical properties

The mechanical response of PMCs is strongly related to the viscoelastic behavior of the polymer matrix. The viscoelastic behavior is described by the dynamic mechanical properties: storage modulus (E') and loss modulus (E'') as respective measures of material's elastic and viscous character, respectively, and their ratio, expressed as the loss factor ($tan\ \delta$) [64]. For details refer to 4.2.8.1.

Budai et al. [65] investigated composites consisting of the unsaturated polyester matrix reinforced with varying contents of E-glass fibers. Dynamic mechanical properties of one of the investigated composites[7] is shown in Figure 1.23. The storage modulus at temperature up to about 30 °C was between 4 and 7 GPa – the higher value corresponding to the higher glass fiber content, i.e. 26 wt%. At higher temperatures, a steep decrease in the storage modulus was attributed to the glass transition (T_g)[8] due to the enhanced movement of polymer molecules. The loss modulus increased with increasing glass fiber content as a consequence of internal frictions between the glass fibers, reaching the values from around 0.58 GPa to 0.81 GPa for 14 wt% and 26 wt% fiber contents, respectively. The authors reported that the T_g was around 70 °C independent of the glass fiber content.

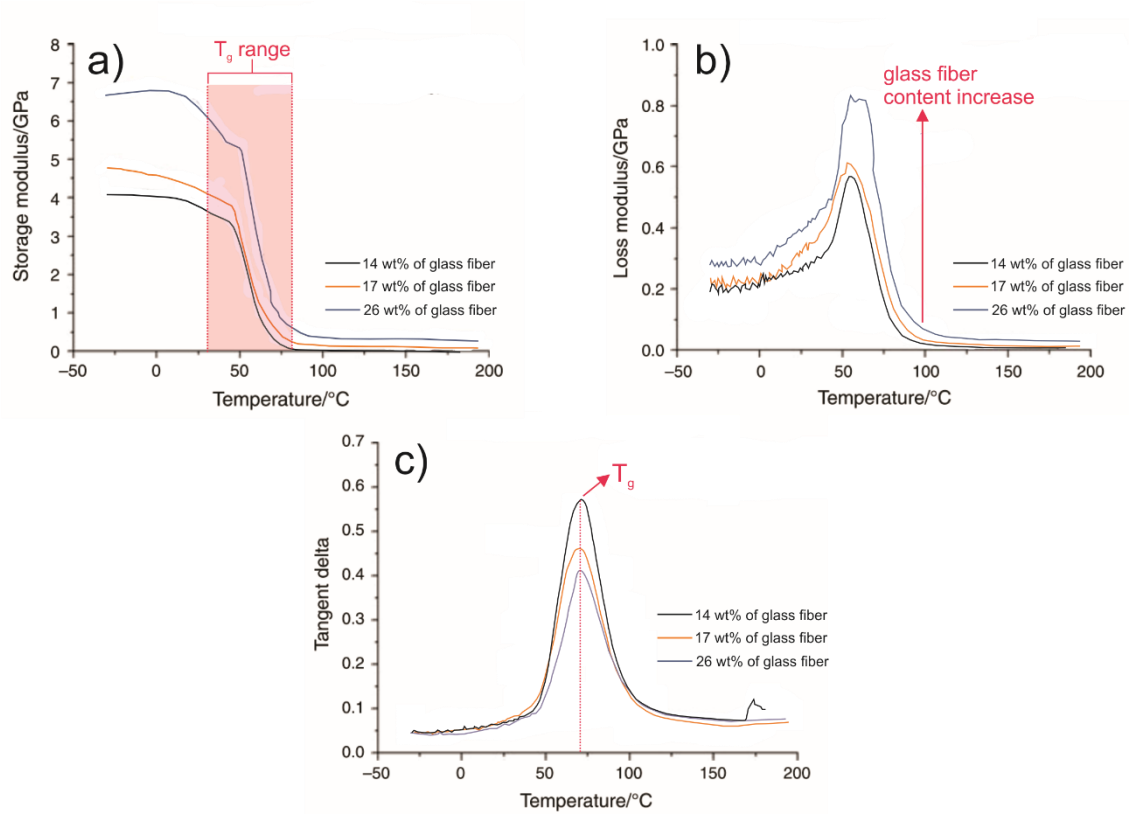


Figure 1.23: The influence of glass fiber content on dynamic mechanical properties. The storage (a) and loss modulus (b) increase with increasing glass fiber content. Glass transition temperature (T_g) determined from the $tan\,\delta$ curves (c) is not affected by the glass fiber content. Redrawn after [65].

Idicula et al. [66] studied the dynamic and static mechanical properties (tensile, flexural and impact) of plain polyester resin and short banana/sisal hybrid fiber-reinforced composites with fiber volume fractions from 0.19 to 0.48. The storage modulus below the T_g for the plain polyester and the fiber-reinforced composites were very close to each other and decreased with temperature. Above the T_g the drop in the storage modulus was significantly larger for the plain polymer (178 MPa) than for the composites (2818 MPa for the volume fraction of fibers of 0.40) – indicating the reinforcing effect of the fibers.

[7] denoted as VIAPAL VUP4627 BEMT/56+M134.

[8] The glass transition temperature (T_g, also known as α-transition): transition from the glassy to the rubbery state. The glass transition extends over a narrow temperature range, however the T_g is determined as a midpoint of the transition range [11].

The authors also calculated the coefficient of reinforcement C that represents the effectiveness of the fiber reinforcement,

$$C = \frac{\left(E'_g / E'_r\right) composite}{\left(E'_g / E'_r\right) resin} \tag{1.2}$$

where E'_g and E'_r are the storage modulus values in the glassy and rubbery state, respectively. A lower value indicates a higher reinforcing effect [67–70]. The calculated C values for the composites were from 0.65 to 0.7, where the composite with 0.40 vol% of fibers reached the lowest value, i.e. the highest reinforcement. At that fraction also the flexural strength reached the peak value, 62 MPa.

Similar dependencies of dynamic mechanical properties on the fiber content in polymer-matrix composites were reported also by Houshyar et al.[70] and Sreenivasan et al. [71].

1.5 Thermal Properties

Thermal properties of polymer-matrix composites are important for their reliable and safe utilization. For example, in applications in electro and automotive industry, the composite material should effectively dissipate the heat generated during the operation of the device to avoid possible defects. Moreover, higher thermal transport properties of the composite contribute to a more efficient molding process. Thus, composite materials should be thermally stable in the temperature range of the device operation and should have high thermal conductivity.

1.5.1 Thermal conductivity

Thermal conductivity (λ) is a measure of a material's ability to transfer heat. How the transport of thermal energy in composite materials will take place depends on the materials composition, content and morphological parameters of the individual phases as well as on a selected processing technology [72–75].

Generally, polymers are good thermal insulators having very low thermal conductivity (0.1 – 0.5 W/mK). The latter can be enhanced by incorporating second-phase inclusions[9] with higher thermal conductivity, for example carbon fibers, carbon black powder, silver, copper and alumina, into the polymer matrix [13, 76–80]. However, λ of such composites does not reach the intrinsic values of the fillers because the second-phase inclusions are insulated by the polymer matrix. Although the heat transfer within individual inclusions is fast, it is slow between them. For example, S. Li et al. [80] reported an increase in the λ of novolac-matrix composites filled with boron nitride (BN) particles with λ = 33 W/mK from ~0.11 W/mK to only ~0.48 W/mK for 0 wt% and 80 wt% of BN, respectively.

Another study by Weidenfeller et al. showed that the thermal conductivity of talc-filled polypropylene is twice higher than the thermal conductivity of copper-filled polypropylene, i.e. 2.5 W/mK and 1.25 W/mK, respectively. In both cases the content of the filler was 30 vol%. One would expect the opposite, since the thermal conductivity of copper is much higher than that of talc, 400 W/mK versus 10.6 W/mK. The authors explained that such behavior is a consequence of higher inter-connectivity between the platelet-shaped talc particles as compared to copper particles [81]. The study demonstrates that the size and the shape of the dispersed phase(s) strongly influence the formation of the thermally conductive path. In general, the smaller the distance between individual inclusion, the

[9] The term second-phase inclusions refers to either fibers or mineral filler particles.

higher the thermal conductivity of a composite [75, 82]. As shown in Figure 1.24, higher aspect ratio of the inclusions at a given fraction increases the heat transfer, meaning that composites with longer fibers have higher thermal conductivity in the fiber direction [75].

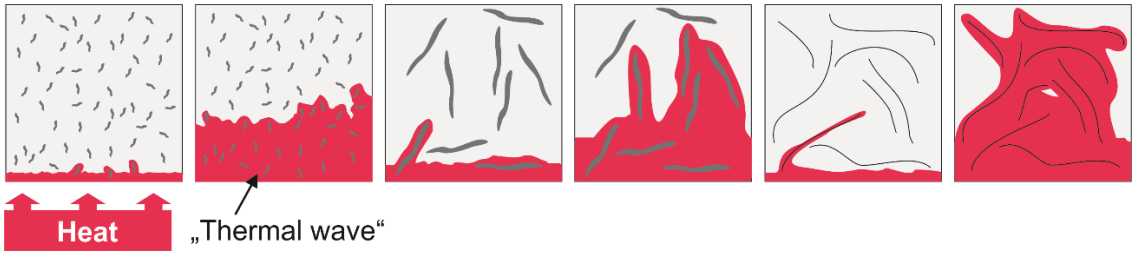


Figure 1.24: The mechanism of heat transfer in polymer-matrix composites: the size and the shape of the inclusions influence the thermal conductivity. Redrawn from [75].

1.5.2 Thermal stability and decomposition

During operation conditions the composites are exposed to elevated temperatures that can deteriorate their physical and mechanical properties. The thermal behavior of polymer-matrix composites is mainly dependent on the polymeric part of the material. When composites are exposed to elevated temperatures, the mechanical and physical properties can change due to breaking of primary (covalent bonds and cross-linking bonds) and secondary (hydrogen bonds, Van der Waals bonds, dipole interactions) bonds in the polymer matrix. Polymers are usually stable up to temperatures of 80 °C or some even up to ~350 °C [83], but when heated over this temperature, the organic matrix starts to decompose. Decomposition temperature (T_d) is defined as the temperature at which a material undergoes chemical and physical changes.

Thermosetting polymers undergo various transitions during heating: glass transition (T_g), leathery to rubbery transition and rubbery to decomposed transition. In Figure 1.25 these transitions are illustrated by changes in the storage and loss moduli [84]. When the material is in the glassy state, the storage modulus is the highest. With increasing the temperature, the secondary bonds in the polymer matrix start to break. At this point, the transition from the glassy to the leathery state is accompanied by a steep decrease in the storage modulus. Upon further heating the material transforms to the rubbery state, wherein the storage modulus is nearly the same as in the leathery state. With further temperature increase also the covalent bonds break and the material decomposes. The T_d is indicated by another decrease in the storage modulus.

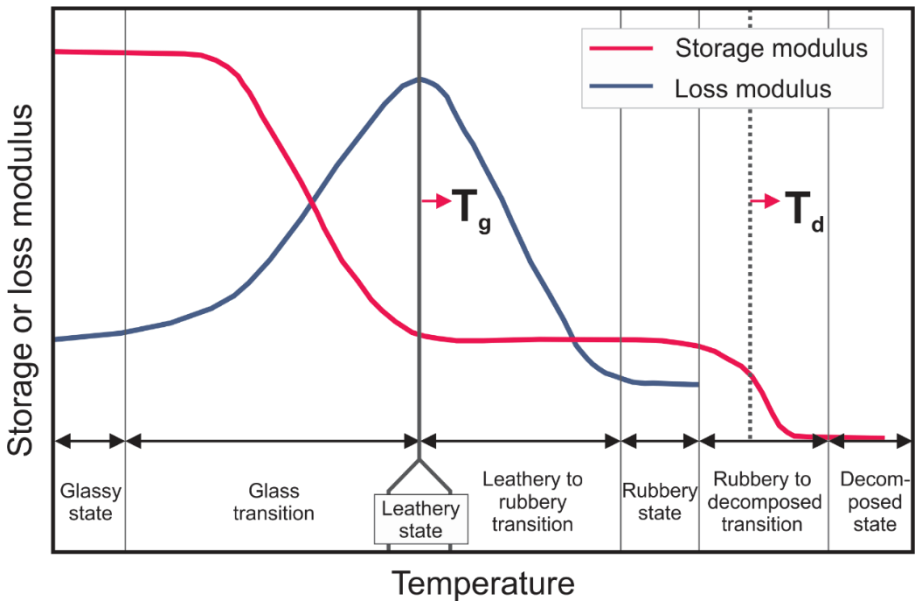


Figure 1.25: Representation of different states and transitions in a thermosetting polymer during heating. Redrawn after [84].

The decomposition of a polyester resin starts at about 350 °C and is completed at about 480 °C as reported by Mouritz et al., leaving less than 5 % char residue of the initial mass [85]. The majority of the mass loss is attributed to the volatilization of low molecular weight hydrocarbons [86]. Another study by Kandare et al. reported that decomposition of an unsaturated polyester resin in air takes place between 120 °C and 600 °C, namely in three stages that correspond to dehydration (120 °C–275 °C), polymer chain-scission (275 °C–460 °C) and char oxidation (460 °C–600 °C) [87].
Laoubi et al. studied the thermal behavior and change in mechanical properties of composites based on unsaturated polyester matrix and reinforced with E-glass fibers when subjected to moderate (up to 100 °C) and to elevated temperatures (200 °C and 280 °C). They reported that the decomposition of the composites is a two-step process that takes place between 130 °C–200 °C and between 250 °C–440 °C. The tensile strength, elastic modulus and flexural strength of the composites were improved after heating up to 100 °C, for example the tensile strength of the polymer increased from ~61 MPa to ~69 MPa. This is attributed to additional cross-linking of the thermoset resin. But when exposed to higher temperatures, the tensile strength of the composite decreased from about 130 MPa to about 115 MPa at 100 °C and 280 °C, respectively [86].

Chapter 2

Environmental Considerations in Manufacturing and Waste Management of Polymer-Matrix Composites

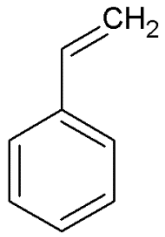
2.1 Styrene

Styrene emissions are one of the major environmental concerns in the manufacturing of glass-fiber-reinforced composites (GFRC). During the molding process, a part of styrene evaporates from the unsaturated polyester resin and causes dangerous vapors in the workplace. Exposure to styrene emission affects the health of workers, however, the main concern is related to its possible carcinogenicity.

Styrene is one of the most important industrial unsaturated aromatic monomers, widely used in production of various plastics, for example polystyrene and expanded polystyrene, styrene copolymers and unsaturated polyester resin. At room temperature, styrene is a colorless liquid hydrocarbon that evaporates easily and has a distinctive, sweet odor. The main properties of styrene monomer are listed in Table 2.1. Styrene is synthesized by dehydrogenation of ethylbenzene in the presence of polymerization inhibitors. Small amounts of styrene are naturally present in some foods, such as legumes, beef, clams, eggs, nectarines and spices. Small amounts can also be present in packaged foods due to the migration from the polystyrene packaging material. It is also present in combustion products, such as cigarette smoke and automobile exhaust [88].

Due to its reactive double bond, styrene very easily polymerizes, even at room temperature. Due to high reactivity and relatively low cost, it is widely used as a crosslinking agent and viscosity modifier in unsaturated polyester resin.

Table 2.1: Properties of styrene monomer.

Property	Data
Chemical structure	
Molecular formula	C_8H_8
Chemical structure	$C_6H_5CH{=}CH_2$
Molecular weight	104.14
Physical state	colorless to yellowish oily liquid (at room temperature)
Boiling point	145-146 °C
Odor threshold	0.036 mg/m^3
Freezing point	-30.6 °C
Density	0.9059 g/cm^3
Vapour pressure at 20 °C	0.6 kPa
Reactivity	Readily polymerizes when heated or exposed to light; releases heat and may be explosive

2.1.1 Occupational exposure

The occupational exposure to styrene is most extensive during the handling of the unsaturated polyester resin and manufacturing of objects from the GFRC. There are several factors that influence the level of styrene concentration in workplace air and the exposure of workers, namely processing technique, ventilation system, materials composition (% of styrene content) and personal protective equipment. Depending on the material composition, unsaturated polyester resin may contain up to 40 wt% of styrene, of which 10 wt% can evaporate into the workplace air during the manufacturing [88].

The highest levels of styrene exposure were measured in open mold processes, such as in hand lay-up. This technique is used for manufacturing of large objects, such as boats, truck parts, wind turbine blades, baths, etc., where the UP resin is manually sprayed onto the fibers by workers. A survey from reinforced plastic plants in the USA has shown that in the open mold processes the average exposure to styrene was two or three times higher than in the press-mold processes (24–82 ppm versus 11–26 ppm) [88, 89]. The typical values of styrene loss in open-mold processes are from 8 to 14 %, in SMC and BMC processing from 1 to 2 % and in closed mold processes less than 1 % [90]. However, over the past years, styrene emissions in industry have declined as a result of improved industrial hygiene, improved processing technology, polymer resins with lower styrene content and stricter regulations.

2.1.1.1 Workplace exposure limits

Occupational exposure limits (OEL) define the allowable concentration of hazardous compounds in workplace air and are intended to protect workers from exposure to toxic

chemicals. The national authorities and institutions, such as Occupational Safety and Health Administration (OSHA) and The National Institution for Occupational Safety and Health (NIOSH) provide guidelines and standards for EOL. The exposure limits, as defined by Association Advancing Occupational and Environmental Health (ACGIH), are [91]:

- **Time-weighted average concentration** (TWA) is the value to which the workers may be exposed repeatedly, day after day, without adverse health effects. The concentration may not be exceeded in any part of the 8-hour workday during the 40-hour workweek.
- **Short-term exposure limit** (STEL) defines the maximum allowable concentration to which the worker may be exposed over a short period of time, usually 15 min.
- **Ceiling limit** (C) is the concentration value that should not be exceeded during any part of the working day.

However, the EU commission did not determine neither indicative nor mandatory TWA concentrations and STEL for occupational styrene exposure. The exposure limits were defined in internal acts of the individual EU member states and thus, the range of OEL values is quite broad, as listed in Table 2.2. In Slovenia, the TWA concentration of styrene exposure has decreased from 100 ppm to 20 ppm[10] [92] in the year 2001. The Labor Inspectorate of the Republic of Slovenia carries out the control of exposure limits in industry.

Table 2.2: Styrene concentration limits, for 8-hour exposure TWA and STEL (or C when STEL data is not available) in different countries across Europe [90].

Country	8-hour TWA (ppm)	STEL or C (ppm)
Belgium	50	100
Denmark	25	-
Finland	20	50
France	50	-
Germany	20	40 (30 min)
United Kingdom	100	250
Slovenia	20	80
Italy	20	40 (15 min)
Norway	25	37.5
Poland	12	47
Portugal	20	40
Hungary	12	12

2.1.1.2 Health effects of styrene exposure

The most common route of styrene exposure is by inhalation and in minor extent via skin contact. The occupational exposure occurs mainly via the lungs, where pulmonary uptake of styrene ranges from 60% to 70% of the inhaled dose [93]. Health effects are determined by the dose, duration and the route of exposure. Dermal exposure to styrene, either vapor or liquid, causes skin irritation, burns and acute dermatitis. Short-term health effects to styrene exposure at concentrations below 50 ppm include eye, nose and throat irritation,

[10] 20 ppm = 86 mg/m^3

increased nasal secretion, wheezing and coughing. Styrene is neurotoxic and many studies reported that exposure to styrene affects the central nervous system [93].

Exposure to larger amounts can lead to "styrene sickness" that is manifested in the form of headache, nausea, vomiting, weakness, dizziness, fatigue and ataxia [94]. Symptoms like drowsiness, lightheadedness, dizziness, headache, tiredness and balance disturbances were reported in reinforced plastic workers exposed to concentrations above 100 ppm [88]. Pulmonary oedema, cardiac arrhythmia, memory loss and a progressive loss of consciousness leading to comma were also reported as a consequence of severe inhalation styrene vapors [94].

The United States Environmental Protection Agency (US EPA) and International Agency for Research on Cancer (IARC) have classified styrene as a possible human carcinogen (group 2B) with limited evidence on carcinogenicity in experimental animals and inadequate evidence in humans [89]. When styrene is absorbed through the body, it undergoes metabolic oxidation to styrene 7, 8-oxide. The majority of concerns related to carcinogenicity from styrene exposure are related to 7, 8-oxide metabolite which can covalently bond to DNA. 7, 8-oxide is classified by IARC as probably carcinogenic to humans (group 2A) [89]. 7, 8-oxide is further metabolized into urinary metabolites, namely mandelic acid, phenyl glycolic acid and hippuric acid [94].

2.1.2 Monitoring exposure to styrene emissions

Sampling and measuring of styrene exposure is usually done by absorption on solid sorbents, such as charcoal. The samples are then desorbed with carbon disulfide and analyzed by gas chromatography using a flame ionization detector (OSHA Method OR6-09) [95]. The sampling may be active where the air is pumped through the sorbent tube. This sampling is faster and is useful in cases where large sample volumes are needed. In passive sampling, styrene penetrates into the sorbent by diffusion which makes the sampling quite long and is often used for measuring the mean concentration in long-term exposure [96]. When workers wear personal equipment, the exposure to styrene is usually biologically monitored by measuring the concentration of the main styrene oxidation metabolites in urine, i.e. mandelic and phenyl glycolic acid. The measurements are done after the workday.

2.1.2.1 Exposure to styrene emissions in the company

The monitoring of worker's exposure to styrene emissions in the company was performed in February 2014. The active sampling was done by the help of personal pumps that were worn by workers for 45 min. The monitoring was carried out on five different workplace locations. The samples were analyzed as described in the OSHA Method OR6-09. All the measured TWA styrene concentrations were below the OEL, as listed in Table 2.3.

Table 2.3: Results of worker's exposure to styrene emissions.

Sampling place	TWA (mg/m^3)
1	3.6
2	19.3
3	8.7
4	9.2
5	3.5

2.2 Waste Management of Composites

The growing market and increased use of composites are concurrently leading to a higher volume of composites waste. In Europe, landfill and incineration have been the main disposal routes for end-of-life composites, accounting for about 98 % in the year 2003 [97].

However, stricter environmental regulations and legislations increase the responsibility of the producer, decrease the landfill disposal and increase the options for more sustainable solutions of waste management. End-of-Life Vehicles directive (ELV) (2000/53/EC) is a European Union (EU) directive that greatly impacts the composite industry [98]. It states that in the year 2015, 95% of a vehicle by weight should be reused or recovered and 85% of a vehicle by weight should be reused or recycled, meaning that only 5% is sent to landfill. Use of fiber-reinforced composites in automotive industry has been steadily increasing over the past years due to their advantages (especially light weight) they bring to increase fuel efficiency and to reduce CO_2 emissions in order to comply with EU legislations (from the present 130 g/km CO_2 to 95 g/km CO_2 in 2021)[6]. In 2011, a vehicle produced in Europe consisted of 120 kg of plastics, 20 % accounting for fiber-reinforced composites [99].

The EU directive on Waste Electrical and Electronic Equipment (WEEE) (2002/96/EC) [100] also applies to composites since they are widely used in electronic and electrical appliances. WEEE directive states that the recovery of components from electrical and electronic equipment should be at least 80 % by an average weight per appliance and, furthermore, the reuse and recycling should be from 50 % to 75 % by an average weight per appliance, depending on the category of WEEE.

The EU Waste framework directive (2008/98/EC) [101] classifies waste management in five priority levels with the most desirable being the waste prevention and waste minimization and the least landfill disposal and incineration (see Figure 2.1).

In most EU countries the landfill taxes are about 30 euros per ton of waste, however they are rising and are, in some countries, ~50–70 euros per ton of waste [102]. Moreover, in Germany, the landfilling of composite waste is already forbidden since the year 2005. Besides that, incineration has become limited by the energy content obtained and according to the amount of generated pollutants. The calorific value from combustion of GFRC mainly depends on the amount of the polymer content. High inorganic content (up to ~80%) in BMCs and SMCs absorbs a high amount of energy during combustion and decreases the calorific value of the polymer matrix, which was reported to be around 30.000 kJ/kg for polyesters, vinyl esters, phenolic and epoxy resin [5].

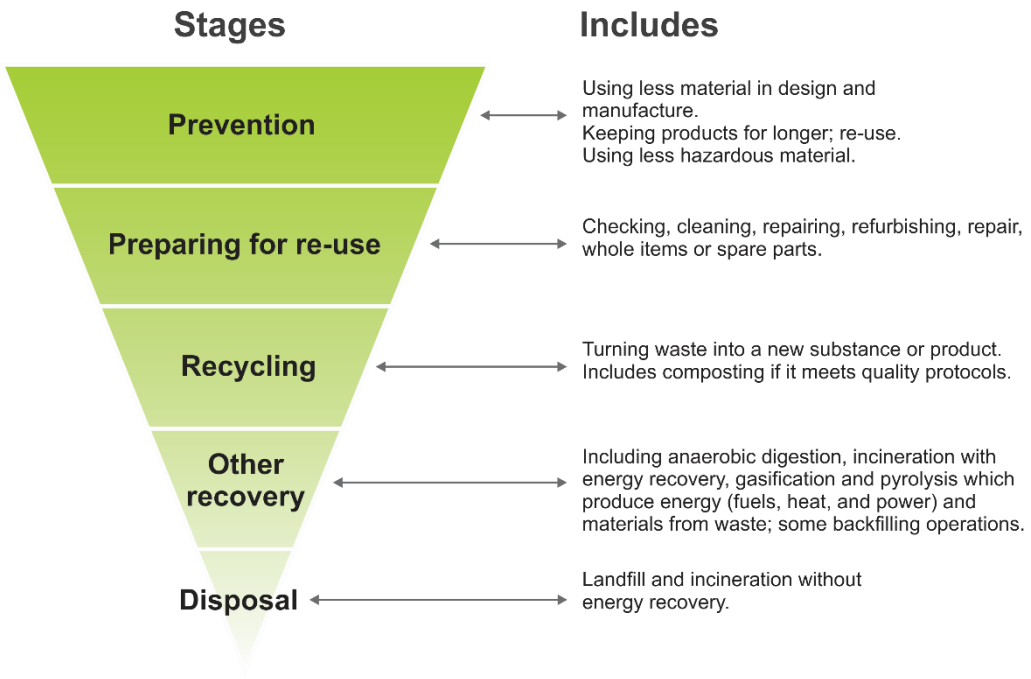


Figure 2.1: EU waste hierarchy: stages and associated actions. Redrawn after [103].

2.2.1 Recycling of fiber-reinforced composites

Recycling of glass fiber composites is challenging and hard due to their multiphase composition which is especially the case for the thermoset-based composites, since they cannot be re-melted or re-molded again as compared to the thermoplastics. Another reason is that composites are usually fastened or bonded to other materials or they contain metal fixtures. Therefore, before the composite can be recycled, the parts have to be de-bonded, disassembled and separated. Another issue is inadequacy of recycling processes for recovery of composites in order to retain original properties of the material as well as of individual constituents and a lack of suitable products for the recycled materials.

In general, recycling processes for thermoset matrix composites can be separated into mechanical, thermal and chemical recycling [5, 104].

Mechanical recycling involves down-cycling or size reduction of composite waste. The composite waste is shredded, ground and milled into fractions of different sizes. Coarser fragments can be used as reinforcement in new composites, more fine graded fractions can be a partial replacement for $CaCO_3$ mineral filler in new BMCs and SMCs or in concrete and cement mixtures for nonstructural applications where mechanical properties are not of priority importance [99, 105].

Besides the combustion with energy recovery, thermal recycling includes two other methods, i.e. fluidized bed process and pyrolysis [5, 99, 104]. The main goal is to separate and retain the fibers and fillers from the polymer matrix. However, due to high temperature (450 °C–600 °C) that may damage the fibers, their reuse is limited. The products of the polymer matrix volatilization, i.e. gases and liquids, can be further used as fuels and additives in other chemical processes and materials.

In chemical recycling different solvents are used to depolymerize the matrix and to obtain fibers, fillers as well as monomers from the polymer matrix decomposition. Depending on the solvent used, which can be water, glycols or acid, chemical treatment can be defined as hydrolysis, glycolysis and acid digestion, respectively. Studies have also been done using water under subcritical conditions [106]. Research has only been done on the laboratory scale, and the development and improvement of the process efficiency are still ongoing. Although the temperatures are lower as compared for example with thermal recycling, the glass fibers still degrade during the treatment, thus the method is more suitable for the carbon fibers.

Some of the recycling methods for GFRC have been commercialized, such as mechanical recycling by ERCOM (Germany), Phoenix Fiberglass (Canada) and Mecelec (France). It turned out that not all the projects were as successful as expected, namely ERCOM and Phoenix Fiberglass terminated. On the whole, the main constraints for the wider utilization of composites recycling are cost effectiveness, i.e. price and quality of the recycled material, transportation to distant processing facilities, and a lack of markets for the recycled materials [5].

Currently, a viable option for GFRCs is recycling in cement kilns, where the polymer matrix burns off providing energy and inorganic residue for the cement clinker which is further ground to form cement [107], or they are combusted and converted into fuel for industry [108].

The recycling of carbon FRCs is more widespread. Some companies offer recycling with pyrolysis, for example ELG Carbon Fibre in United Kingdom, Karborek in Italy and CFK Recycling in Germany. Carbon fibers are more valuable as well as their recycling was supported by the aerospace industry which all contributed to higher commercialization [107].

Chapter 3

Aims and Hypotheses

The microstructure of bulk molding compound (BMC) composites is formed during the molding process and depends on several factors, such as the weight content of individual constituents – fillers and E-glass fibers as the reinforcing phase, their shape, size, orientation and distribution, as well as on the molding conditions during manufacturing and the geometry of the mold cavity. Depending on the shape, curvature and thickness of the molded part, the microstructure can be quite complex and different across local areas. Furthermore, variations of the microstructure influence the functional properties of BMC products, predominantly used in automotive, electrical and appliance industry.

The thesis addresses the analysis of the microstructure of BMC composites containing different proportions of E-glass fibers. The image analysis, tessellation methods and statistical descriptors that were found useful in this work could be applied to characterize the microstructure of BMC parts manufactured in serial production. The aforementioned methods could be used as a support in the design of BMC parts, in adjusting the molding conditions or in optimizing the material composition. In this way we could have a certain and better control over the microstructure formation that can subsequently contribute to higher quality of the molded products.

The main hypothesis for the first part of the thesis is that the level of microstructure uniformity of polymer-matrix composites is strongly influenced by the glass-fiber weight content and distribution. Therefore, the aims in this part include:

- To investigate the influence of E-glass fiber content and distribution on the microstructure of BMC composites by means of different microstructural descriptors.
- To derive microstructural and statistical descriptors that can be used to distinguish between the microstructures of composites with different levels of uniformity.

The mechanical, viscoelastic properties, and thermal properties of the composites depend on the glass fiber content, and the latter is consequently related to the degree of microstructural uniformity. Our hypothesis was that the optimum mechanical properties, i.e. the highest flexural strength and the highest reinforcing effect (the lowest value of coefficient of reinforcement) are obtained in the sample with the highest level of microstructural uniformity. Thermal conductivity of the BMC composites depends not only on the fiber fraction but also on the distribution of the fibers in the microstructure.

The following aims were constructed for the second part of the thesis:

- To investigate the influence of E-glass fiber content and distribution on the mechanical and viscoelastic properties of BMC composites by measurements of flexural strength and dynamic mechanical analysis.
- To analyze the relation between the thermal conductivity, E-glass fiber content and distribution in the composites with different fiber contents.

Chapter 4

Materials and Methods

In this chapter we describe the preparation and molding of BMC composite samples containing different proportions of glass fibers and mineral filler content. We review the methods used for the microstructural characterization and measurement of physical properties.

4.1 Sample Preparation

For the purpose of this work three series of BMC composite samples with varying glass fiber and mineral filler content were commercially prepared (Tetradur Gmbh, Hamburg, Germany). The ratios of individual constituents for all BMC samples are presented in Figure 4.1. The first series of BMC composite material included samples with 15 wt%, 20 wt%, 25 wt%, 30 wt% and 35 wt% of glass fibers. The second series of samples was prepared with 5 wt%, 10 wt% and 15 wt% of glass fiber content. Here, an additional reference sample containing only a mineral filler and a polymer resin was also prepared (0 wt%). The third series consisted of BMC samples with 5 wt%, 7.5 wt%, 10 wt%, 12.5 wt%, 15 wt% and 20 wt% of glass fibers. The first and the second series of the samples were fabricated in the amount of 20 kg, while the last one was fabricated in the amount of 5 kg for the individual composition.

In all cases the glass fibers were electrical grade glass fibers (further in the text denoted as EGF). According to the manufacturer's information, the initial length of fibers was 4.5 mm with a diameter of approximately 10 µm as determined by scanning electron microscope (SEM). The mineral filler was $CaCO_3$ with the particle size ranging from a few microns up to a few tens of microns, also determined by SEM. The polymer matrix (PM) was based on thermosetting unsaturated polyester, styrene and additives, comprising 21 wt% of the overall composite material in all samples. All composites were routinely analyzed by an internal method proposed by the supplier of the material. The thrust force is the force needed for a certain amount of material to go through a cylinder of specific dimensions. The results showed that with increasing the fiber content, the thrust force increased from ~1000 N to ~1700 N for the sample with 5 wt% and 35 wt%.

The test specimens were fabricated by transfer molding, in accordance with the standard ISO 3167 [109]. About 42 g of the compound was placed into a mold cavity that was heated to around 165 °C and pressed at a molding pressure of 20 MPa on a hydraulic compression press (HPK 100/6, Bussmann, Munchen, Germany) with a cure cycle of 2 minutes. After molding, the test specimens were cooled down to room temperature. The scheme in Figure 4.2 indicates the dimensions of the samples and the filling direction of the material during the molding process. Molded test specimens of selected composites are shown in Figure 4.3.

We would like to point out that selected properties of BMC composites (i.e. flexural strength and thermal conductivity) of the samples with the same content of EGFs were not reproducible between individual series. We noticed that the values of selected properties were different, however the trends were similar. Therefore, we could not compare the samples from all three series of composites in terms of absolute values. In the chapters, where the selected properties are discussed, the difference is pointed out and the results are presented for individual sample series, otherwise the results are presented as a function of EGF weight content.

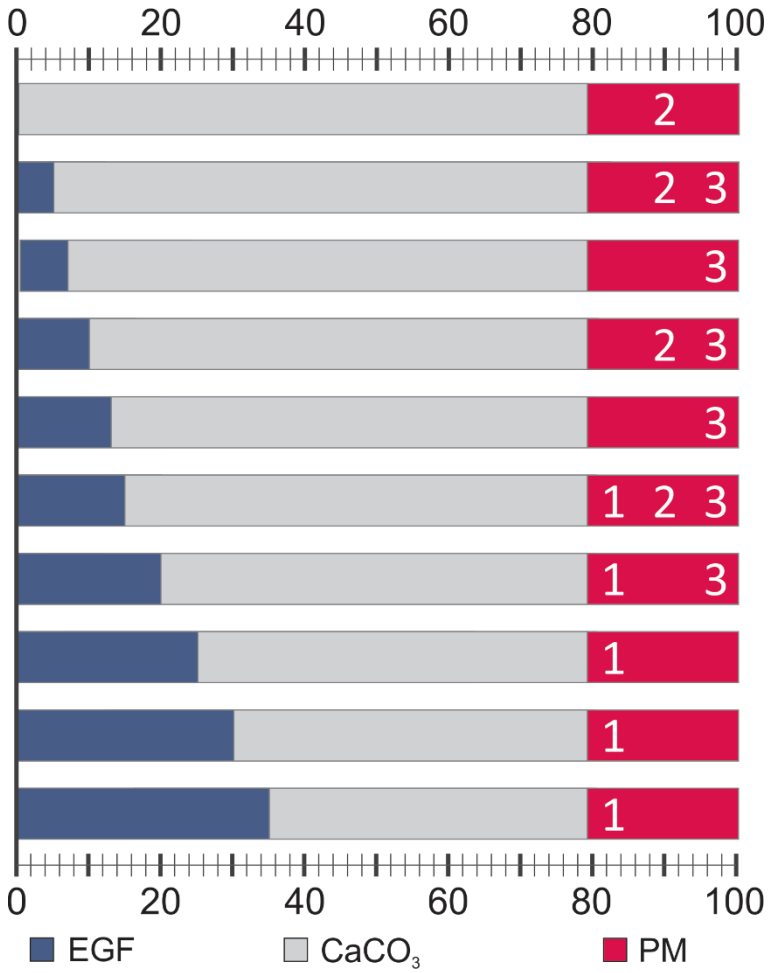


Figure 4.1: Composition of BMC composite samples with varying EGF (0/5/7.5/10/12.5/15/20/25/30/35 wt%) and $CaCO_3$ content. The number denotes the number of the series.

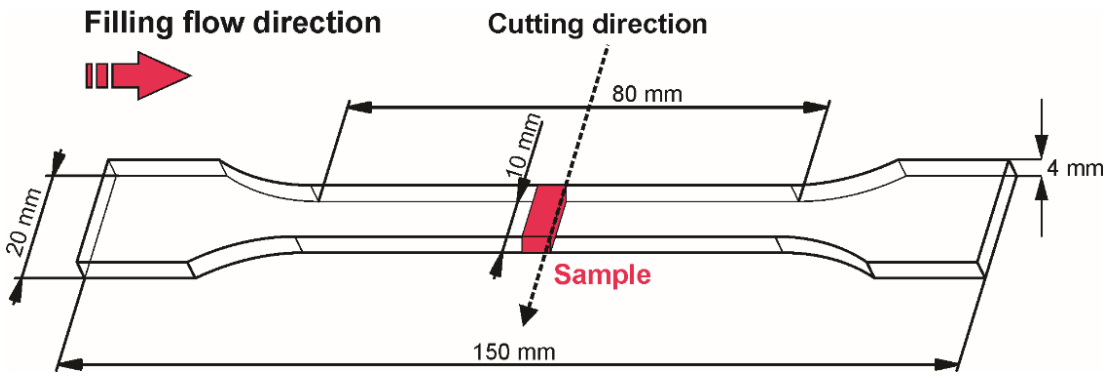


Figure 4.2: Schematic representation of the filling flow direction of BMC material during transfer molding, dimensions of the test specimen, cutting direction and sample position.

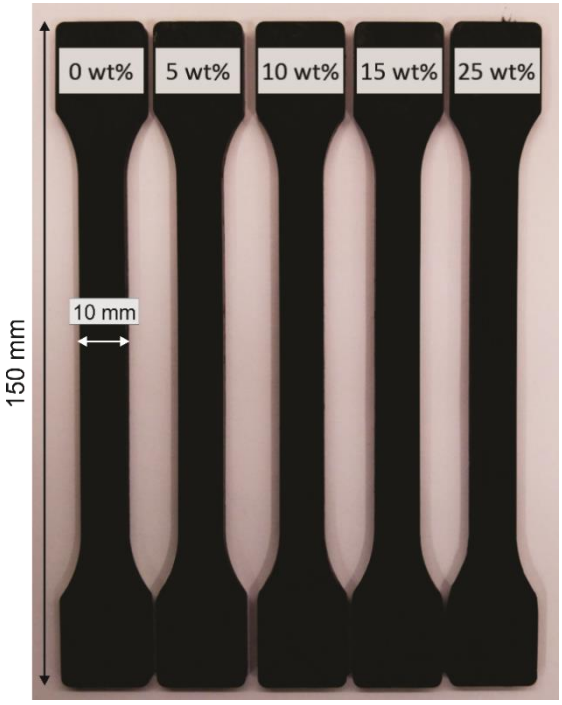


Figure 4.3: Molded test specimens of BMC composites with 0 wt%, 5 wt%, 10 wt%, 15 wt% and 25 wt% of EGFs.

4.2 Characterization Methods

4.2.1 Density measurements

The densities of the samples were determined by water immersion technique (Archimedes' principle). The samples were first weighed in air and then when immersed in water. The density was calculated according to the equation,

$$\rho_{=} \frac{m_{air}}{m_{air} - m_{water}} \times \rho_{water} \tag{4.1}$$

where ρ is the density of the sample in g/cm^3, m_{air} is the mass of the sample in the air, m_{water} is the mass of the sample when immersed in the water and ρ_{water} is the water density at room temperature (0.99705 g/cm^3 at 25 °C) [110].

4.2.2 Scanning Electron Microscopy

The microstructures of BMC samples were investigated using Field-Emission Scanning Electron Microscope FE-SEM (JSM-7600F, Jeol Ltd., Tokyo, Japan) or in some cases by JSM 5800 (Jeol Ltd., Tokyo, Japan).

Prior to the SEM investigation the test specimens were cut perpendicular to the filling-flow direction, as represented in Figure 4.2, to yield a cross-sectional area with dimensions of 10 mm × 4 mm. Special attention was paid to the standard metallographic technique normally used for the preparation of flat surfaces for the SEM investigation in order to establish the best conditions for the grinding and polishing of the samples' cross-sections. BMCs require careful handling, since the fibers could be easily removed from the polymer matrix, leaving an empty space and giving a misleading picture of the sample quality. The grinding and polishing steps were performed on an automatic grinding machine (EcoMet/AutoMet 250, Buehler, Lake Bluff, Illinois). The best conditions, which gave satisfactory results, i.e. high quality of the cross-section surfaces for the SEM analysis, are explained further on: firstly, the samples were ground on silicon carbide (SiC) 180/P180 grit paper followed by 280/P320 grit paper. Then, the samples were subsequently polished on a polishing cloth partially covered by diamond suspension with particle size of 9 µm and 3 µm for several minutes. MetaDi fluid extender was used in both polishing steps. The final step included polishing with colloidal silica polishing dispersion (0.02 µm particle size).

The polished cross-section surfaces were sputter-coated with a thin carbon layer to achieve electrical conductivity and to avoid charging. The micrographs were taken in the backscattered-electron mode (composition contrast mode - COMPO) at an accelerating voltage of 15 kV.

The samples' cross-sectional areas were divided into quarters, whereas the bottom quarter was further divided into 9 segments as shown in Figure 4.4. The sampling included capturing 9 SEM images from an individual segment. Each SEM image was of dimensions 481 µm × 361 µm. The overall investigated area for each sample was 1.6 mm^2.

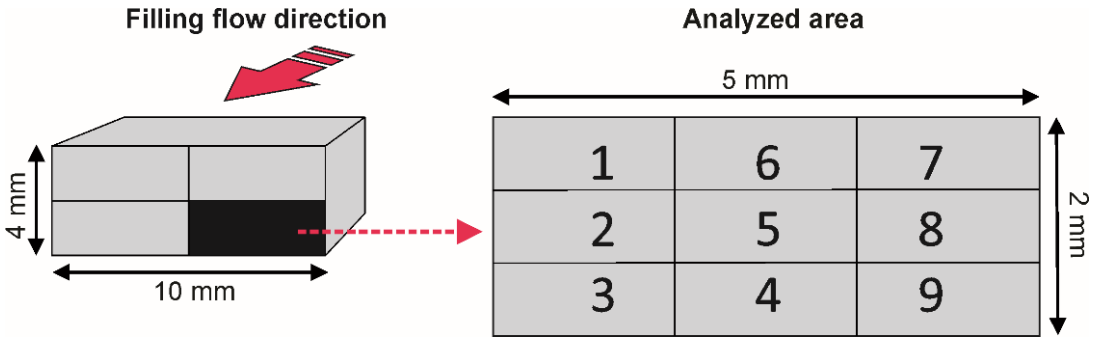


Figure 4.4: Sampling scheme of the cross-sectional area for the microstructural analysis.

4.2.3 Image analysis

4.2.3.1 Voronoi diagrams

Voronoi diagrams were generated from the SEM micrographs of the samples with different EGF weight contents. For individual sample 9 SEM micrographs were used (taken from 9 different segments, as previously shown in Figure 4.4).

The construction of the Voronoi diagrams proceeded as follows (see Figure 4.5):

- The center of each glass fiber on the SEM micrograph (a) was marked with a black point using Corel Paint Shop Pro X7 software. The oval-shaped and elongated fibers were treated in the same way, meaning that the point mark was put at the center of the intersection area of each fiber.
- The point-pattern images (b) were saved as binary images and subsequently employed to construct the Voronoi polygons (c) using ImageJ software [111].
- The area of each Voronoi polygon was measured using Image Tool software [112].
- The absolute areas were then normalized to relative polygon areas, according to equation: $A_r = A_p N / A_{total}$, where A_p is the absolute polygon area size, N is the number of polygons in the sample and A_{total} is the area size of the sample. The number of polygons included in the calculations was from ~500 to ~2000 for the composites with 5 wt% and 20 wt% of EGF, respectively.

The mean area size (μ_A) and standard deviation (σ_A) of the Voronoi polygons area size were calculated according to:

$$\mu_A = \frac{1}{N} \cdot \sum_{i=1}^{N} x_i \tag{4.2}$$

$$\sigma_A = \sqrt{\frac{1}{N-1} \cdot \sum_{i=1}^{N} (x_i - \mu_A)^2} \tag{4.3}$$

where A denotes area, x_i is the area size of the polygon i, and i is the number of polygons ($i = 1, \ldots, N$).

The homogeneity parameter HP_A was calculated according to Equation 1.1, listed in Chapter 1.3.2.1.

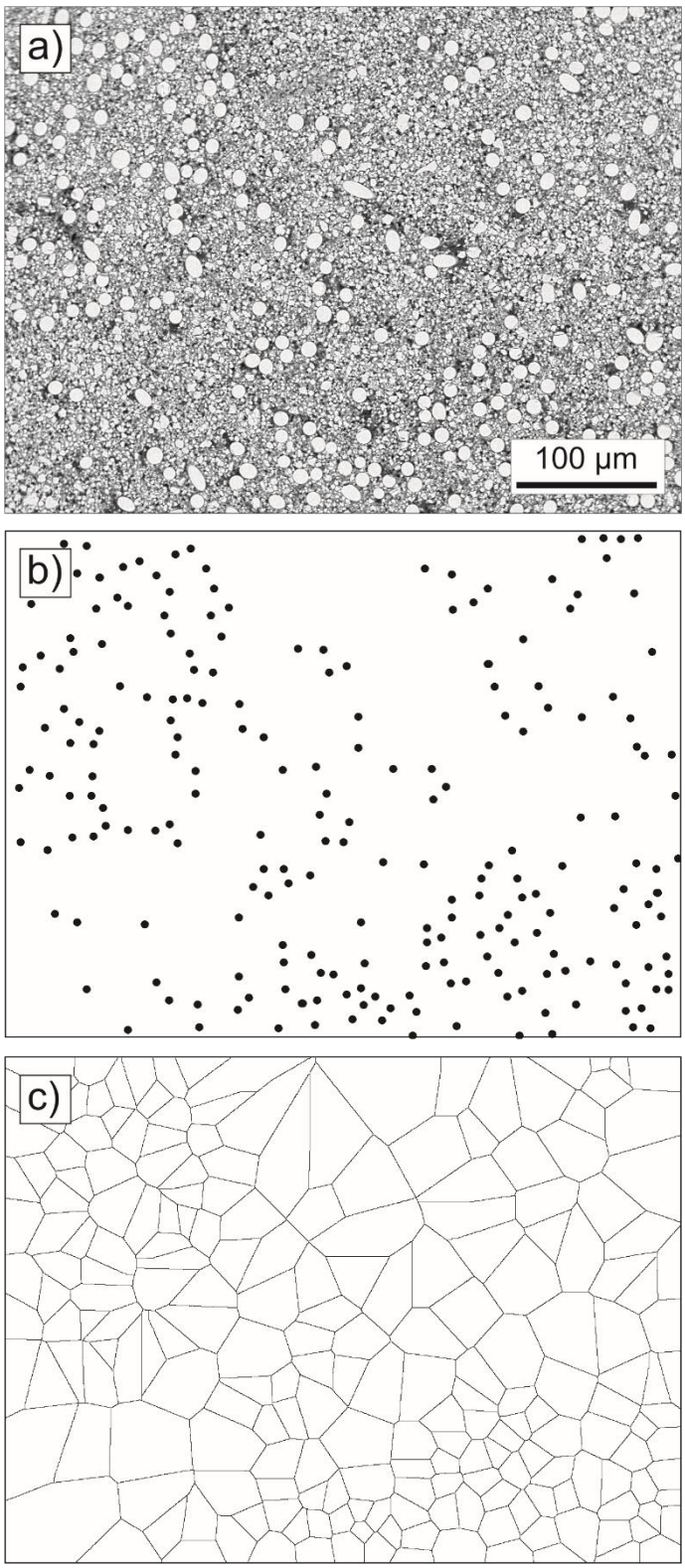


Figure 4.5: Steps in construction of Voronoi diagrams: SEM micrograph (a), binary point-pattern image (b) obtained from the SEM micrograph by point marking of each fiber and the Voronoi diagram (c) generated from the point-pattern image.

4.2.4 Computer-simulated microstructures

Monte Carlo method is based on computer algorithms used to model complex systems involving random variables in order to model the probability of possible results. It was used to simulate a system of randomly distributed disks for each composition of the BMC material.

The model is built up by assigning random values to variables that define the system. First, a simulation box and initial random state of particles/discs is constructed; in another step the particles are randomly moved to get a new state. The steps of random movement of particles are repeated. In each simulation state, the position of a particle is described by two randomly generated numbers, one for the x-coordinate and one for the y-coordinate. The obtained numerical results are time-average values of all possible states of the system [49], uniformly distributed over the interval [0,1].

Therefore, if we want to compare the positions of particles in a given simulation step with the experimental microstructures, we can create an image on the basis of the obtained coordinates by using a suitable software [49]. Just like the experimental, also the simulated microstructures can be quantitatively described by RDF and Voronoi diagram analysis.

As shown in Figure 4.6, the Voronoi diagrams were generated from the modeled microstructures. A sample area of 481 µm × 361 µm and a disk diameter of 11 µm were chosen which correspond to the SEM image size and fiber diameter, respectively. Between 250 and 1000 realizations were used to ensure good statistics. The same as in the experimental data, the Voronoi polygon areas were measured and normalized.

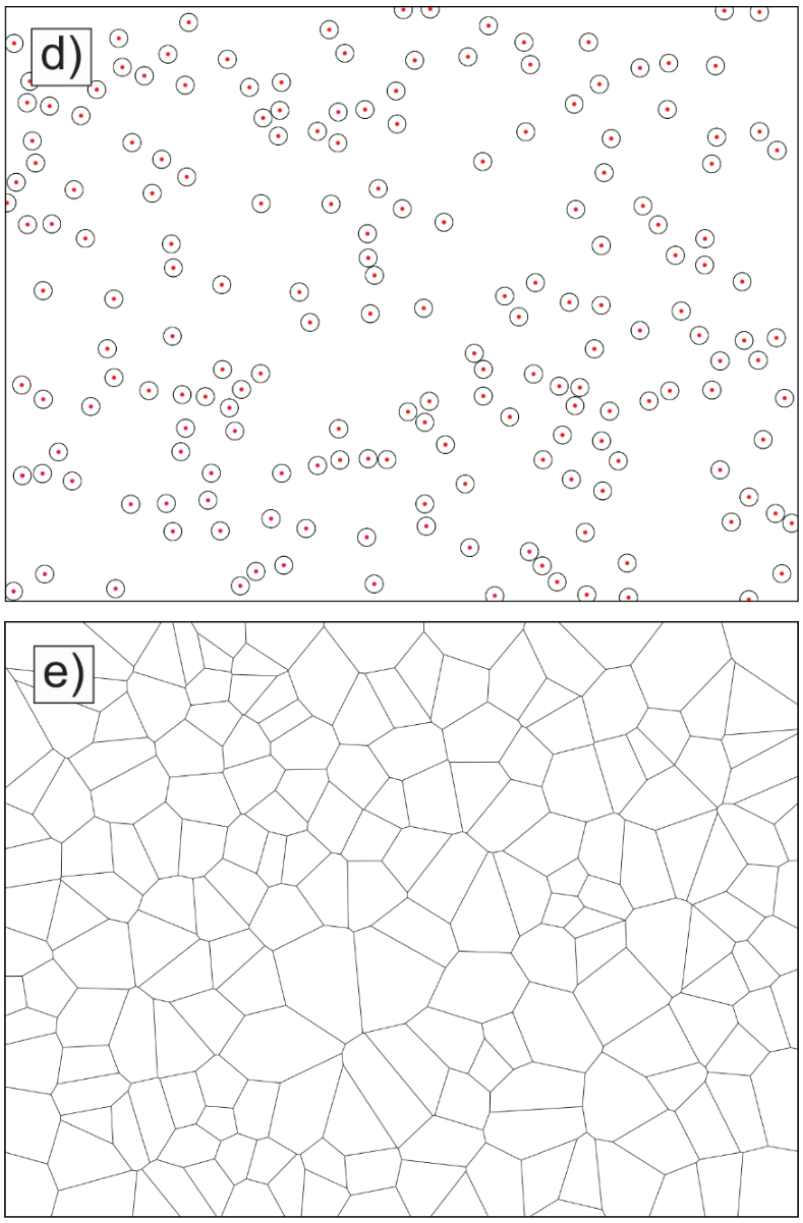


Figure 4.6: Modeled random distribution of disks (d) and a corresponding Voronoi diagram (e).

4.2.5 Radial distribution function

RDF was applied to experimental and modeled microstructures with randomly distributed disk patterns in order to quantitatively describe the microstructures. As previously described in Chapter 1.3.2.2 the RDF measures the density of particles at a specific distance from the center of a reference particle. The random distribution of points in the modeled microstructures yielded RDF to be equal to 1 in the whole interval which enabled the detection of possible fiber clustering in the experimental samples.

4.2.6 Stereological analysis

Stereological analysis was performed in order to gain a better insight into how the fibers in the composites are oriented. As presented in Figure 4.7, the individual fibers on the SEM micrographs (a) were outlined in black in order to obtain binary (black fiber on a white background) images (b) of the microstructures. A stereological analysis was performed using the Image Tool program [112]. The elongation parameter (EP) was determined as the ratio of the longest and the shortest axis of the fiber cross-section.

Here, we would like to note that we tried to determine the three-dimensional fiber orientation in the composites with X-ray microtomography. However, it turned out that because of the high concentration of $CaCO_3$ mineral filler in the material, which has a similar density as EGF and thus similar energy absorption, the detection of fibers was not possible.

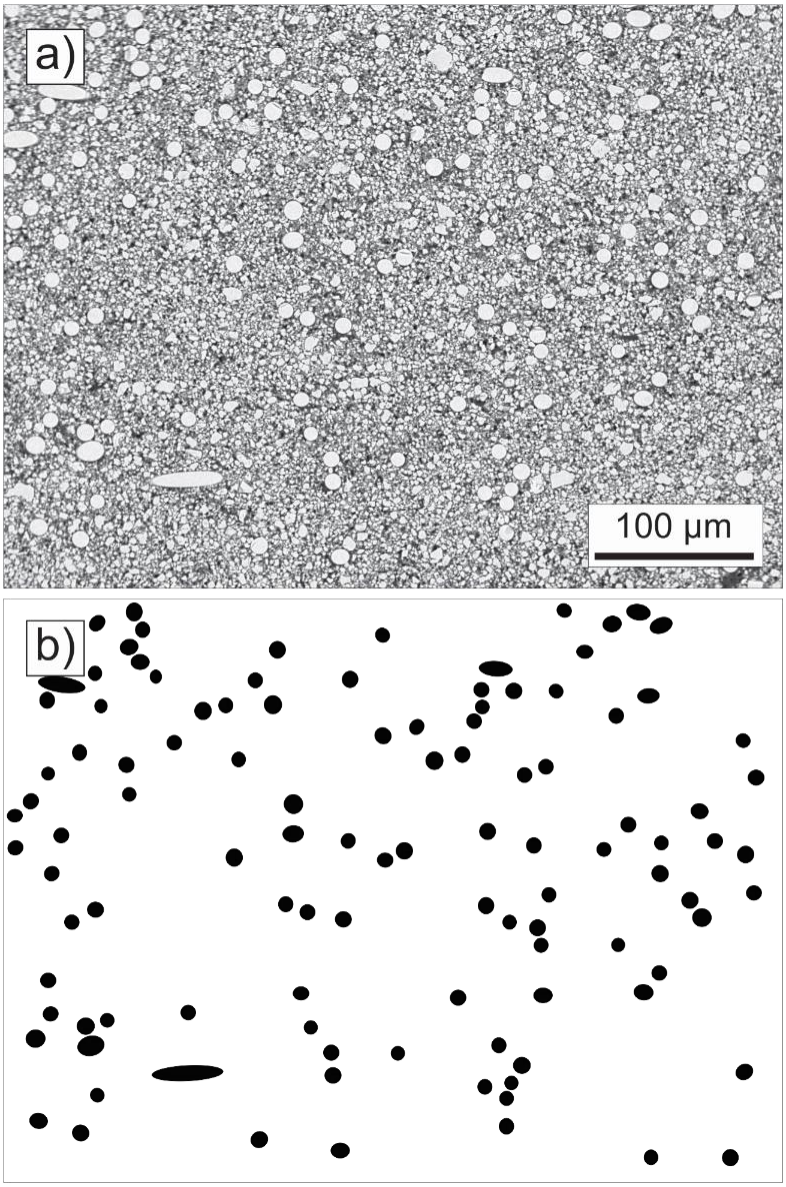


Figure 4.7: Stereological analysis. The fibers on the SEM micrograph (a) are outlined in black (b).

4.2.7 Three-point bending test

Three-point bending test (Alpha 50-5, Messphysik Materials Testing Gmbh, Fürstenfeld, Austria) was used to determine the flexural strength of the BMC composite samples. The test was carried out in accordance with the standard ISO 178 [113]. A span support of 64 mm and a crosshead speed of 2.0 mm/min were used during testing. The test was carried out under ambient conditions using 15 test specimens for each formulation of the BMC material. The flexural strength was calculated using:

$$\sigma_f = \frac{3Pl}{2bh^2} \tag{4.4}$$

where σ_f is the flexural strength (GPa), P is the maximum fracture load (N), l is the span between the supports (mm), b is the width of the sample (mm) and h is the thickness of the sample (mm).

4.2.8 Thermal analysis

4.2.8.1 Dynamic mechanical analysis

The dynamic moduli (E' and E'') and the damping behavior ($tan\ \delta$) of the BMC composites were determined by DMA on a TA Q800 thermal analyzer (Q800 DMA, TA Instruments, New Castle, Delaware, United States). Before the measurement the standard test specimens were cut with a diamond blade saw to the length of 60 mm and thinned to 3.5 mm by grinding (the width remained the same, i.e. 10 mm). The test was carried out at a frequency of 1 Hz and at strain amplitude of 10 µm using a three-point bending mode. The properties were measured in the temperature range from 20 °C to 200 °C at a heating rate of 2 °C/min.

The storage modulus E' is a measure of the sample's elasticity and is related to the stiffness of the material. It is calculated from the stress-strain behavior according to the equation

$$E' = \frac{\sigma_0}{\varepsilon_0} \times \cos\delta \tag{4.5}$$

where σ_0 is the stress, ε_0 is the strain and $\cos\ \delta$ is the phase angle.

The loss modulus E'' describes the viscosity of the sample and is a measure of how much applied energy a material will dissipate. Usually it is related to the molecular mobility of polymer chains and polymer relaxations. It is calculated from the equation

$$E'' = \frac{\sigma_0}{\varepsilon_0} \times \sin\delta \tag{4.6}$$

The ratio between the loss and storage modulus is the loss factor $tan\delta = E''/E'$ and is a measure of the materials damping behavior. It is associated with the molecular movements, fiber-matrix interphase adhesion, phase boundaries and defects like dislocations [114].

The coefficient of reinforcement C was calculated from the storage modulus values in the glassy and rubbery range of the BMC composites, according to Equation 1.2.

4.2.8.2 Thermogravimetry and Differential Thermal Analysis

Thermal stability and decomposition of BMC samples were studied by simultaneous Thermogravimetry and Differential Thermal Analysis (TG/DTA, Netzsch STA 409 PC). The samples of about 5 mm in diameter and the thickness of approximately 3 mm were

placed into platinum-rhodium (PtRh) crucibles and heated from room temperature to 650 °C (some to 900 °C) at a heating rate of 5 K/min in synthetic air atmosphere.

4.2.8.3 Differential Scanning Calorimetry

Differential scanning calorimetry (DSC) was used for two purposes: firstly, to follow the thermal effects that occur during the heating of the uncured BMC composites up to 200 °C and secondly to measure the specific heat capacity (c_p). The analysis was performed on differential scanning calorimeter DSC 204 F1 (Netzsch, Germany).

In the first case, about 28 mg of the uncured BMC composite material was placed into Al crucibles with pierced lids and heated from room temperature to 200 °C with a heating rate of 10 K/min.

For measuring the specific heat capacity, the samples of about 5 mm in diameter and the thickness of ~1 mm were cut from the test specimen, put in Pt crucibles with lids, and heated in a calorimeter with a heating rate of 2 K/min from room temperature to 180 °C. To determine the specific heat capacity of the BMC composites, sapphire (Netzsch, diameter of 5.2 mm, thickness of 1 mm) was used as the standard material. The specific heat capacity was calculated from the measured DSC curve,

$$c_p = c_p^{standard} \times \frac{DSC_{sample}}{DSC_{standard}} \tag{4.7}$$

where $c_p^{standard}$ is the specific heat capacity of a standard, DSC_{sample} and $DSC_{standard}$ are the measured DSC curves of the sample and standard, respectively [115]. The c_p values at 20 °C, 100 °C and 180 °C were extracted from the linear fits of the c_p curves [116].

4.2.9 Thermal conductivity measurement

Thermal conductivity of BMC composites was measured with a transient plane source technique [117] by using the HotDisk TPS 2500S equipment (Hot Disk AB, Gothenburg, Sweden) at room temperature. As well as the standard test specimens, also the samples for measuring the thermal conductivity were prepared by transfer molding. However, they were of larger dimensions, i.e. 340×80×4 mm. During the HotDisk measurement a thin disk sensor (Kapton, 2 mm diameter), used both as the heat source and the temperature monitor, was sandwiched and pressed between two individual samples as shown in Figure 4.8. The material was heated at 50 mW for 5 seconds. The length of the current pulse was chosen short enough so that the sensor could be considered in contact with an infinite solid throughout the transient recording. In this way the thermal properties of the surrounding material could be determined by measuring the temperature increase of the disk sensor in a short period of time. The results are given as the average of five measurements.

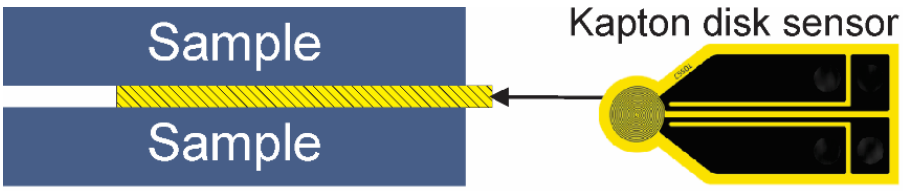


Figure 4.8: Schematic representation of the HotDisk measurement.

4.2.10 X-ray powder-diffraction analysis

The residues obtained after the TG/DTA (i.e. after heating the BMC samples to 900 °C) were analyzed by the X-ray powder diffractometer (PANalytical X`Pert PRO MPD, Almelo, Netherlands, Bragg-Brentano geometry using $CuK_\alpha$ radiation and X`Celerator detector configured in reflection geometry). The parameters used for the step scan mode were $2\theta = 0.034°$ and integration time 100s. The angular range was $2\theta = 5 - 85°$. The phase identification was done by a software package X`Pert High Score assisted by reference patterns database (PDF-2) [118].

Chapter 5

Results and Discussion

5.1 Microstructure

This chapter discusses characterization of microstructures of BMC composites containing different EGF weight fractions. First, we describe the microstructures of composite samples with 0 wt%, 5 wt%, 15 wt% and 30 wt% of EGFs. Next, the Voronoi diagram analysis and RDF analysis were used to characterize the experimental as well as modeled random microstructures that served as a reference in order to disclose differences in microstructure patterns, i.e. fiber distribution uniformity, fiber clustering and local disorder. Furthermore, we calculated the elongation parameter to describe fiber orientation in composites. In the second part, the microstructures of the samples with higher fiber content, namely 25 wt%, 30 wt% and 35 wt%, are presented. The scheme in Figure 5.1 shows the selection of BMC samples and performed methods.

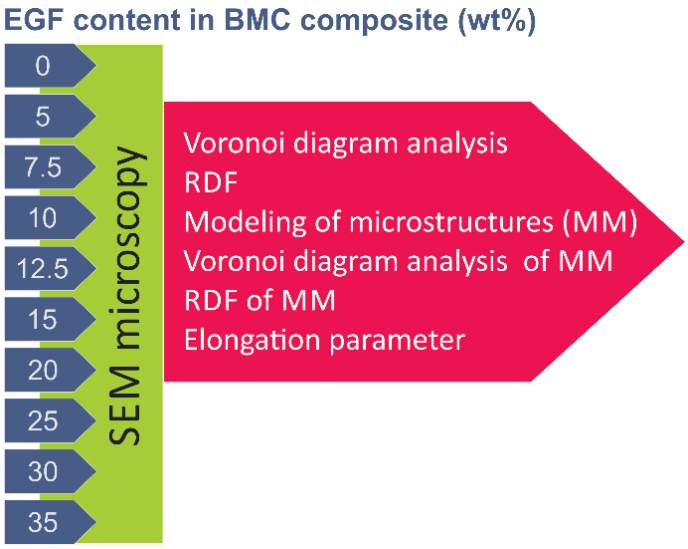


Figure 5.1: Representation of the selected BMC samples and methods that were used and performed for microstructural analysis.

The SEM plan-view and cross-section micrographs of representative BMC composite samples with 0 wt%, 5 wt%, 15 wt% and 30 wt% of EGF content are shown in Figure 5.2. In the case of the BMC sample without EGF (0 wt%), the microstructure contains only irregularly shaped $CaCO_3$ filler particles distributed in the PM. Their sizes range from a

few µm up to a few 10 µm. Note that the plan-view and cross-sectional areas of the said sample are very similar (here, only the cross-sectional micrograph is shown), meaning that the distribution of the filler particles does not depend on the compound filling direction.

From the plan-view micrographs of the samples with 5 wt%, 15 wt% and 30 wt% of EGF content it is evident that the fibers are predominantly aligned parallel to the filling flow direction of the molding compound during processing. Such orientation is apparent from the surface intersections of the fibers where the fibers are visible as long oval-shaped rods. Accordingly, in the microstructures of the cross-sections the intersections of fibers are visible as circles when they are aligned perfectly perpendicular to the cutting position (see Figure 4.2), and as ellipses when they are cut at an angle as shown in Figure 5.2 (right) where the fiber intersections are lined with red.

A marked variation, i.e. the difference in fiber areal density, can be found in the microstructures with increasing EGF content. At a first glance, the fibers in the samples with 5 wt% and 15 wt% of EGF are quite uniformly distributed. However, when looking at the sample with 30 wt% of EGF we can observe some irregularities, such as voids that most likely occurred due to high fiber packing and entrapment of volatiles and air. The density values of all BMC composites are in a range from 1.86 to 2.04 g/cm^3 with no significant differences when EGF content is increased. However, slight deviations could be related to the presence of voids. The density values of commercially available BMC composites containing 20 wt% of EGFs are reported to be 2.0 g/cm^3 [119].

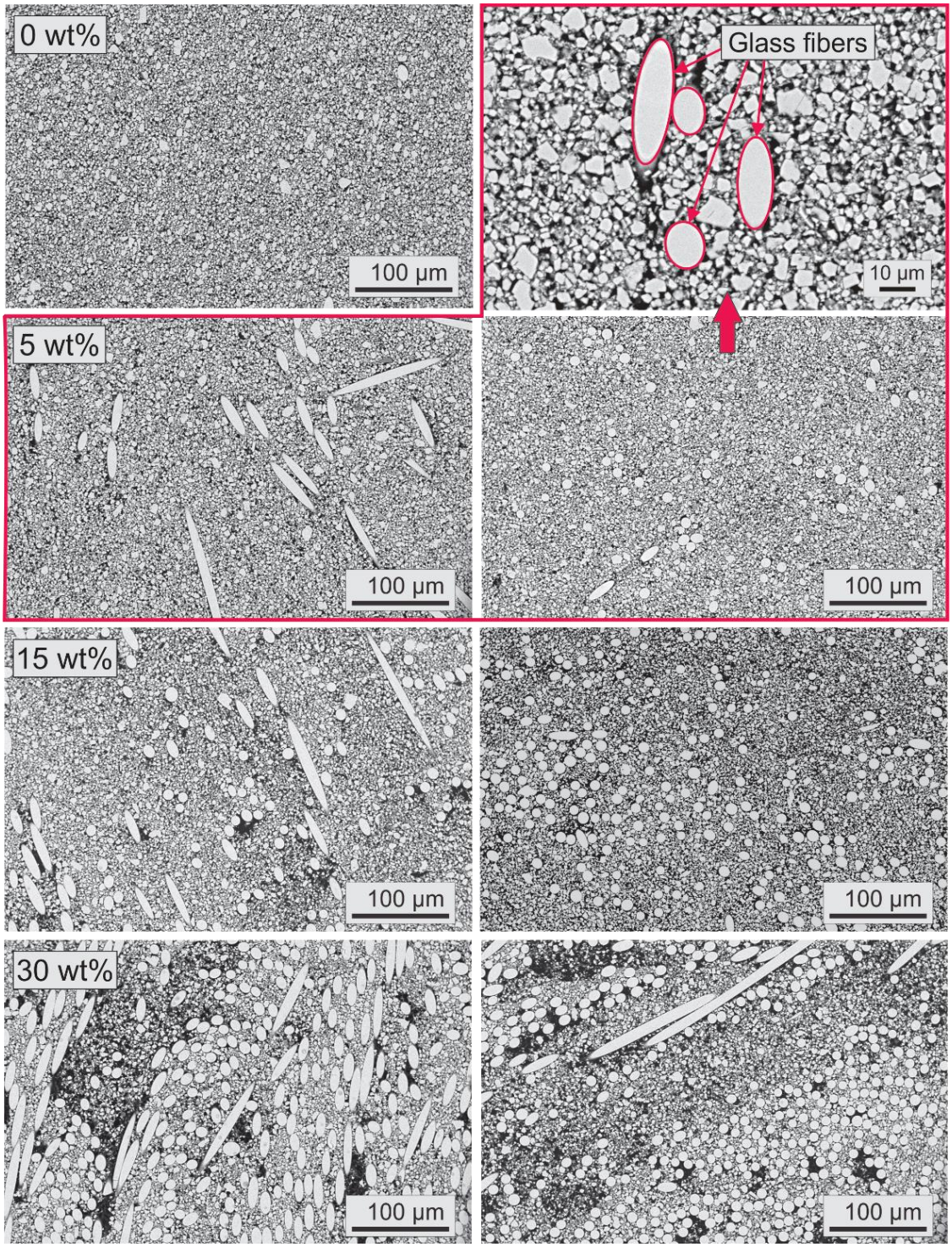


Figure 5.2: Plan-view (left) and cross-sectional (right) SEM micrographs of BMC composite samples with 5 wt%, 15 wt% and 30 wt% of EGF content. For the BMC composite with 0 wt% of EGFs the cross-section microstructure is shown.

5.1.1 Microstructure of BMCs with EGF weight content from 5 % to 20 %

In this subchapter we address the characterization of microstructures of BMC composite samples with EGF weight percent from 5 to 20. The fiber distribution homogeneity or uniformity in the matrix was characterized by Voronoi diagram analysis and was carried out for:

- *characterization of fiber distribution across different areas in the selected cross-section of BMC composite sample;*
- *characterization of fiber distribution in a larger area of the selected cross-section of BMC composite sample;*
- *characterization of fiber distribution in the modeled random microstructures.*

The extent of fiber clustering and the rate of local disorder in composites was described by RDF analysis. The experimental results from both, the Voronoi and RDF analysis were compared with the results extracted from modeled random microstructures. Furthermore, fiber orientation in composites was characterized by elongation parameter derived from the stereological analysis.

5.1.1.1 Voronoi diagram analysis of BMC composite in different areas of sample cross-section

In order to see if and to what extent the fiber distribution homogeneity [120] changes across the cross-section of individual BMC sample, different areas (see Figure 4.4) from the central, middle and edge region, namely 1, 5 and 9, of the samples with 5 wt%, 10 wt%, 15 wt% and 20 wt% of EGFs were compared. We note that the homogeneity of the material structure is treated as the property of the structure without any statistically significant differences across the examined material [120]. SEM micrographs of the investigated areas are shown in Figure 5.3. From the micrographs it is noticeable that the distribution as well as the number of fibers is not identical from area to area of the individual composite. As the fiber content increases, the variation in fiber arrangement in different areas becomes more pronounced, as in the case of the sample with 15 wt% and 20 wt% of EGFs. Furthermore, it is evident that the fiber orientation also varies from area to area. This feature is discussed in Chapter 5.1.1.4.

To evaluate the uniformity of fiber distribution Voronoi diagrams were constructed from the microstructures and further on color classified according to the area size of the Voronoi polygons as shown in Figure 5.4. The number of fibers (N_f) and the values of σ_A and μ_A that were used in the calculations are listed in Table 5.1. The level of fiber distribution homogeneity or uniformity is expressed by the homogeneity parameter HP_A, i.e. the ratio of the standard deviation (σ_A) and the mean area size (μ_A) of Voronoi polygons.

Since the number of fibers was found to be different in areas 1, 5 and 9 within a selected sample, the mean areas were different; this effect was corrected by introducing the HP_A. As mentioned in the introduction, Heijman et al. demonstrated that the HP_q parameter calculated either from the area (A) or perimeter (l) of the Voronoi polygons can be successfully used to evaluate the level of microstructural uniformity [42] where smaller HP_A value indicates higher fiber distribution uniformity.

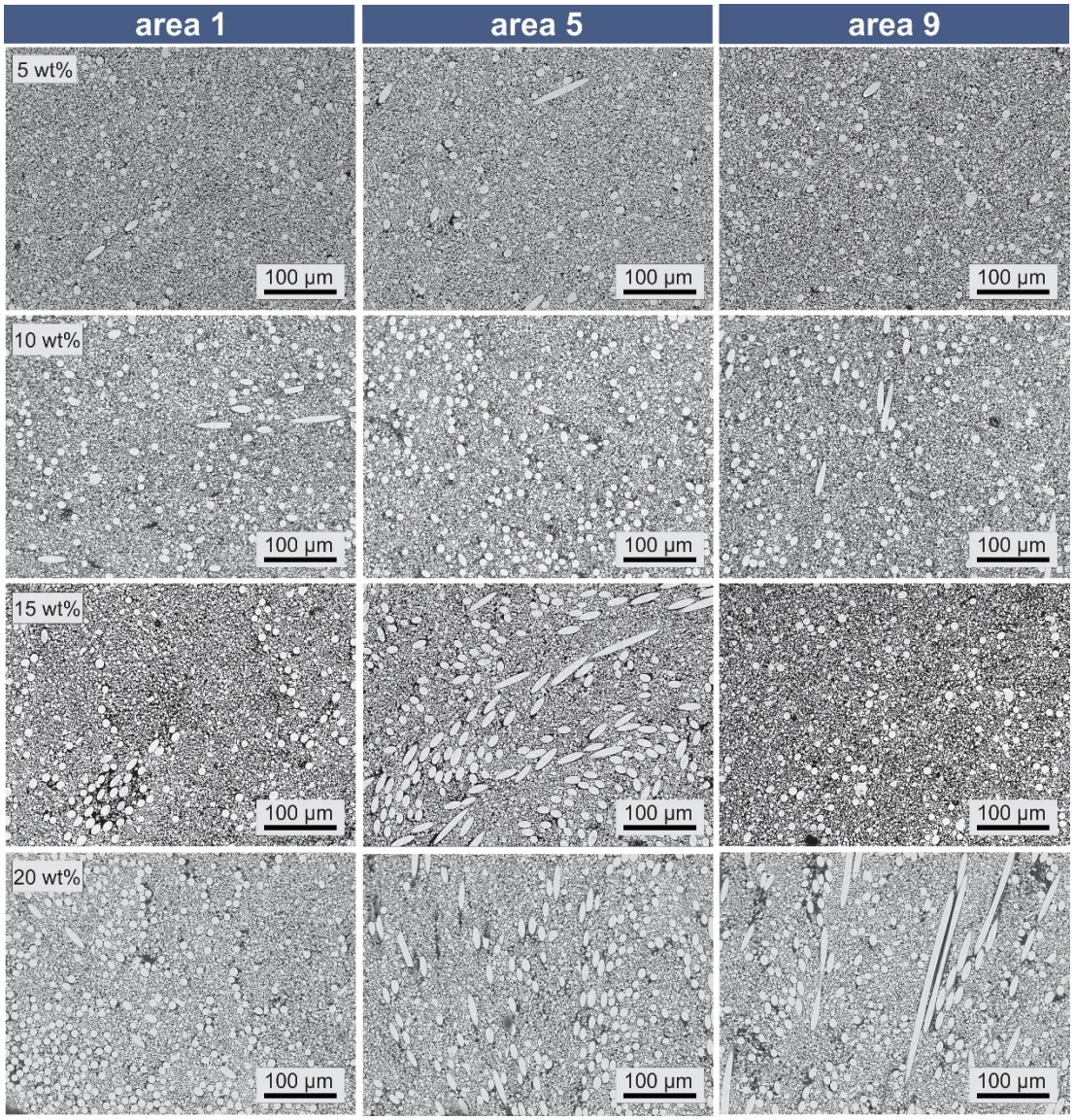


Figure 5.3: SEM micrographs of areas 1, 5 and 9 of the samples with 5 wt%, 10 wt%, 15 wt% and 20 wt% of EGFs.

The HP_A values of the sample with 5 wt% of EGFs are 0.63, 0.58 and 0.60 for the areas 1, 5 and 9, respectively. This indicates that the fiber distribution uniformity slightly varies between local areas of this sample, and the lowest HP_A value was found for the area 5 having the most homogeneous fiber distribution. The Voronoi diagram of this particular area shows fairly large Voronoi polygons (>3000 µm^2) demonstrating that the number of fibers in this area is lower as compared to areas 1 and 9. Taken as a whole, the sample with 5 wt% of EGFs possesses quite homogeneous and uniform fiber distribution. Due to a low fiber content, the microstructure contains large areas filled only with $CaCO_3$ mineral filler and polymer resin (around isolated fibers) as indicated by large Voronoi polygons.

Quite similar results were obtained for the sample with 10 wt% of EGFs, however the Voronoi polygons are smaller due to the higher number of fibers when the fiber content increases. The HP_A values were 0.57, 0.75 and 0.62 for the areas 1, 5 and 9, respectively. If we look at the Voronoi diagram of the area 5, we can see some relatively small polygons in

a size range from 200 µm^2 to 400 µm^2 (orange colored) illustrating smaller spatial distances between neighbouring fibers. This can be related to minor fiber clustering that disturbs the microstructural uniformity, as supported by the higher value of HP_A.

As the EGF content increases above 10 wt%, the difference in fiber spatial distribution becomes more apparent and can be clearly observed from the Voronoi diagrams. The HP_A value varies from 1.03 to 0.61, for area 1 and area 5, respectively. Such a small HP_A value in area 5 means that the distances between the neighboring fibers are quite uniform throughout the entire area, which is also evident from the more equally sized Voronoi polygons. On the contrary, higher HP_A value for the area 1 can be explained by the coexistence of fairly large and small Voronoi polygons that are a consequence of isolated fibers on the one side and fiber clustering on the other, respectively.

As observed from the Voronoi diagrams of the sample with 20 wt% of EGFs, the presence of smaller Voronoi polygons (200–400 µm^2 and <200 µm^2), especially in areas 1 and 5, could be related to the fiber clustering. In these two areas, the deviation from the mean value was the highest as demonstrated by the higher HP_A value.

In our case, it would be unlikely to expect that the distribution of fibers would be consistent across the whole cross-section of the sample of a selected composition. Due to the complex rheology of the molding compound during the molding process the fiber fraction can slightly deviate in local areas although the mold geometry is simple and symmetrical and induces high alignment of fibers in the mold filling direction [27]. Therefore, the number of Voronoi polygons was found to be different in the edge, middle and central regions of the test specimen cross-section due to varying fiber areal density.

As demonstrated by the values of HP_A, the differences in fiber distribution between the areas 1, 5 and 9 become more pronounced and also the increase of fiber distribution inhomogeneity is observed. Hendriks et al. [121] reported the decrease in microstructural homogeneity of the palladium yttria-stabilized zirconia composites as the fraction of the second phase particles increased from 0 to 30 vol%. The HP_A values were ~0.27 and ~0.39, respectively.

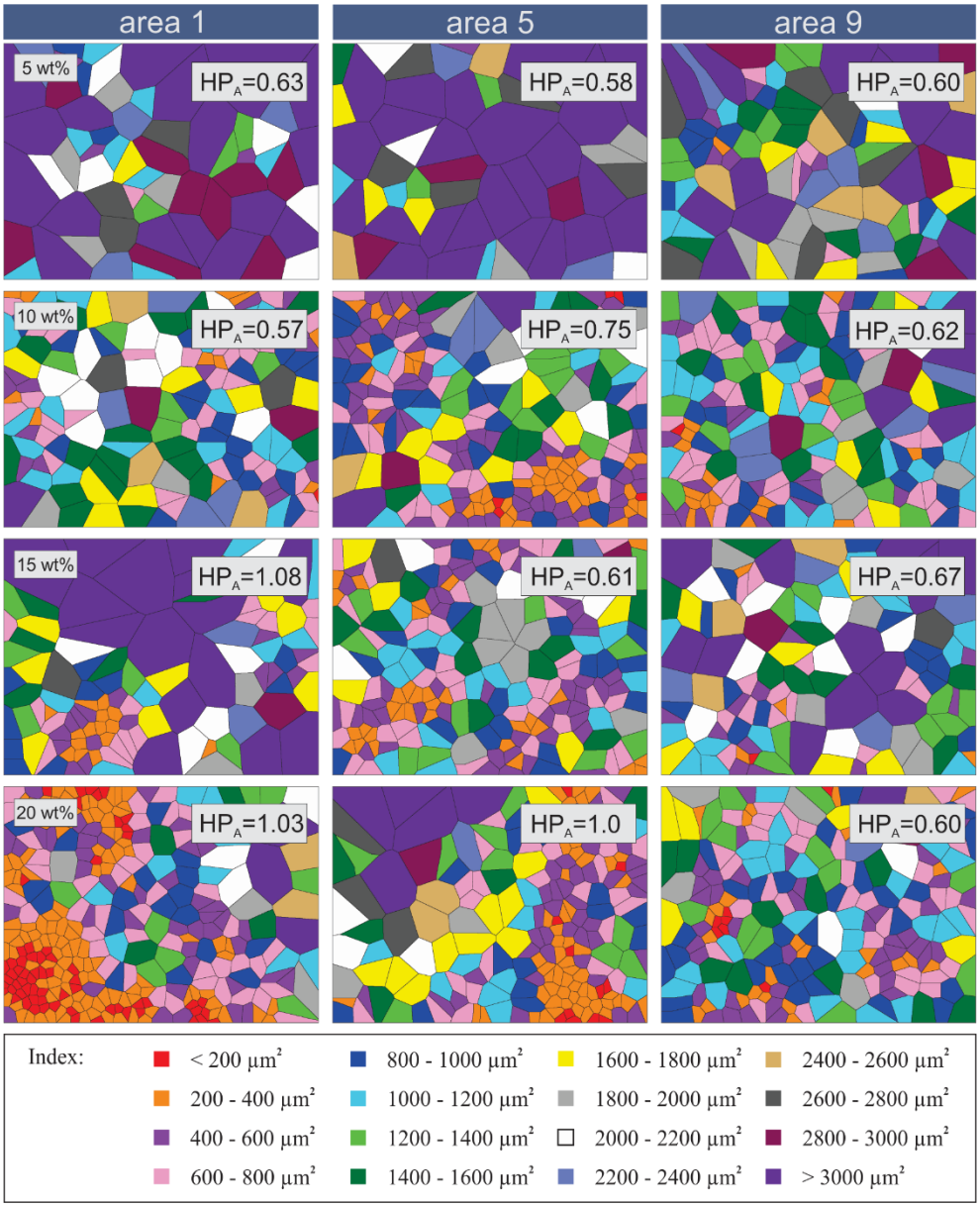


Figure 5.4: Voronoi diagrams constructed from SEM micrographs of areas 1, 5 and 9 of the samples with 5 wt%, 10 wt%, 15 wt% and 20 wt% of EGFs. The fiber distribution uniformity was evaluated by the homogeneity parameter HP_A.

Table 5.1: Number of fibres (N_f), mean area size (μ_A) and standard deviation (σ_A) of Voronoi polygons used in calculations of HP_A.

	EGF content (wt%)											
	5			10			15			20		
	A1	A5	A9	A1	A5	A9	A1	A5	A9	A1	A5	A9
N_f	63	52	90	150	215	168	109	200	113	327	202	200
μ_A	2718	3299	1896	1131	785	1008	1564	845	1507	513	837	845
σ_A	1701	1910	1129	646	592	629	1695	517	1014	528	839	503
HP_A	0.63	0.58	0.60	0.57	0.75	0.62	1.08	0.61	0.67	1.03	1.0	0.60

5.1.1.2 Voronoi diagram analysis of experimental and modeled microstructures

In order to discriminate between more homogeneous and uniform fiber distribution and microstructures, where the fibers tend to cluster together, the experimental Voronoi polygons are compared to Voronoi diagrams constructed from modeled microstructures, i.e. point patterns representing random distribution of fibers that serve as a reference [45, 48, 122].

The SEM cross-section micrographs and the corresponding Voronoi diagrams are shown in Figure 5.5 and in Figure 5.6 (first and second column). Area 4 of the overall analyzed positions (see Figure 4.4) was chosen to represent the microstructure of BMC composites and the distribution of EGFs in the matrix. Modeled patterns and the corresponding Voronoi diagrams are presented in Figure 5.5 and Figure 5.6 (third and fourth column). At lower weight fractions of EGFs, i.e. at 5 wt% and 7.5 wt%, the areas of Voronoi polygons are quite large and similar for both, experimental and modeled Voronoi polygons. As the EGF weight fraction in the composites increases, the spatial distances between the fibers become smaller which is reflected in smaller polygon areas of Voronoi diagrams. In experimental diagrams, particularly marked differences in the size of the polygon areas are observed in the Voronoi diagrams of the composites with 15 wt% and 20 wt% of EGF (Figure 5.6, second column). Here, the relatively small polygons that are surrounded by larger polygons indicate clustering of fibers in the matrix, which probably arises from the insufficient space for the fibers to orient and regularly distribute at higher weight fractions. Pronounced increase and grouping of smaller Voronoi polygons with increasing the volume fraction of the second phase particles was observed by Spitzig et al. They reported that when the sulfur volume fraction in steels increased from 0.004% to 0.028%, the sulfur particles tend to cluster together, thus forming an inhomogeneous microstructure [123]. In contrast, more uniform fiber distributions, which are reflected in equally sized polygons across the whole pattern, can be seen in the Voronoi diagrams obtained from the modeled random distribution of fibers (Figure 5.6, fourth column).

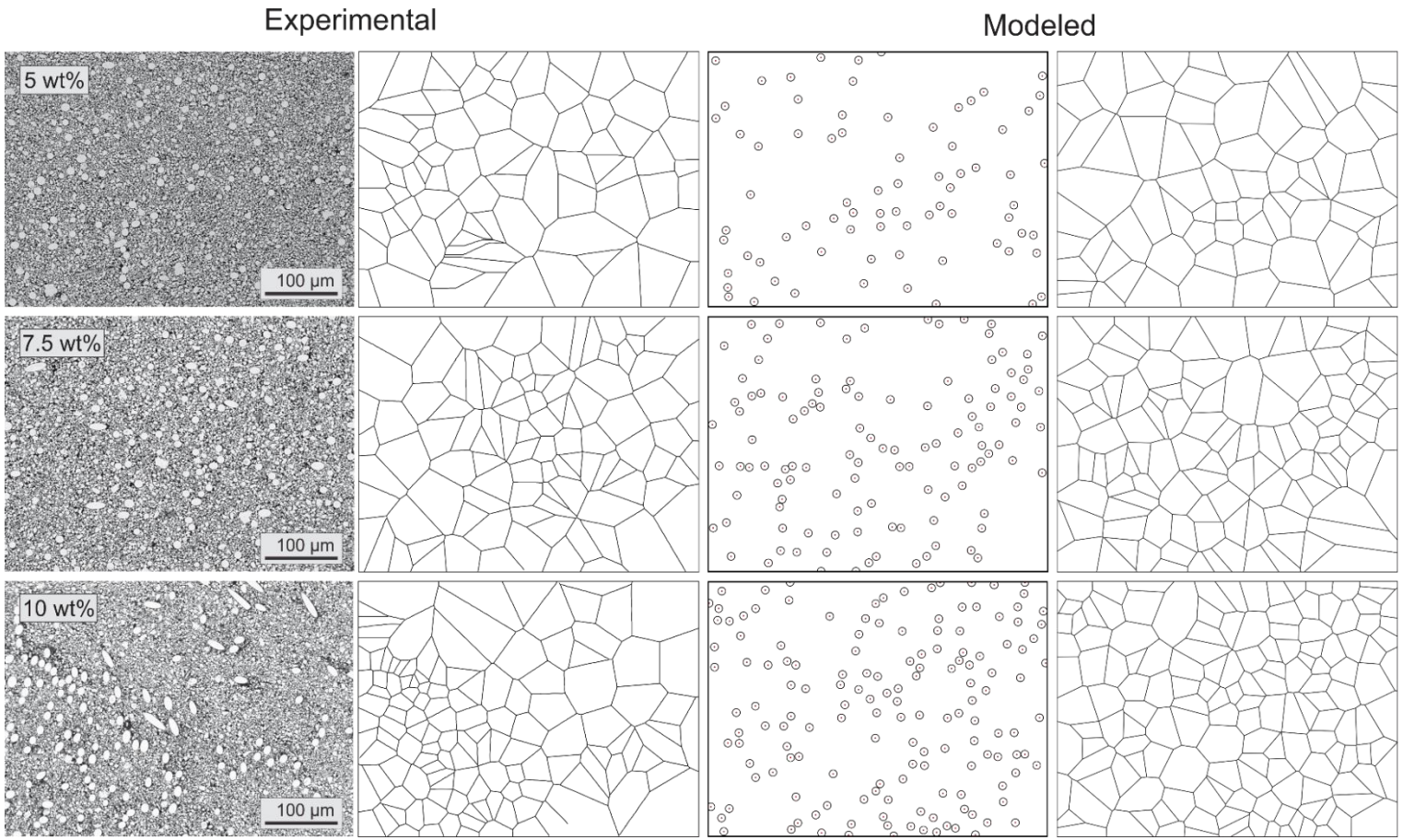


Figure 5.5: Cross-section micrographs (first column) of BMC composite samples with 5 wt%, 7.5 wt% and 10 wt% of EGFs and corresponding Voronoi diagrams (second column). Modeled patterns of fiber distribution and corresponding Voronoi diagrams are shown in the third and fourth column, respectively.

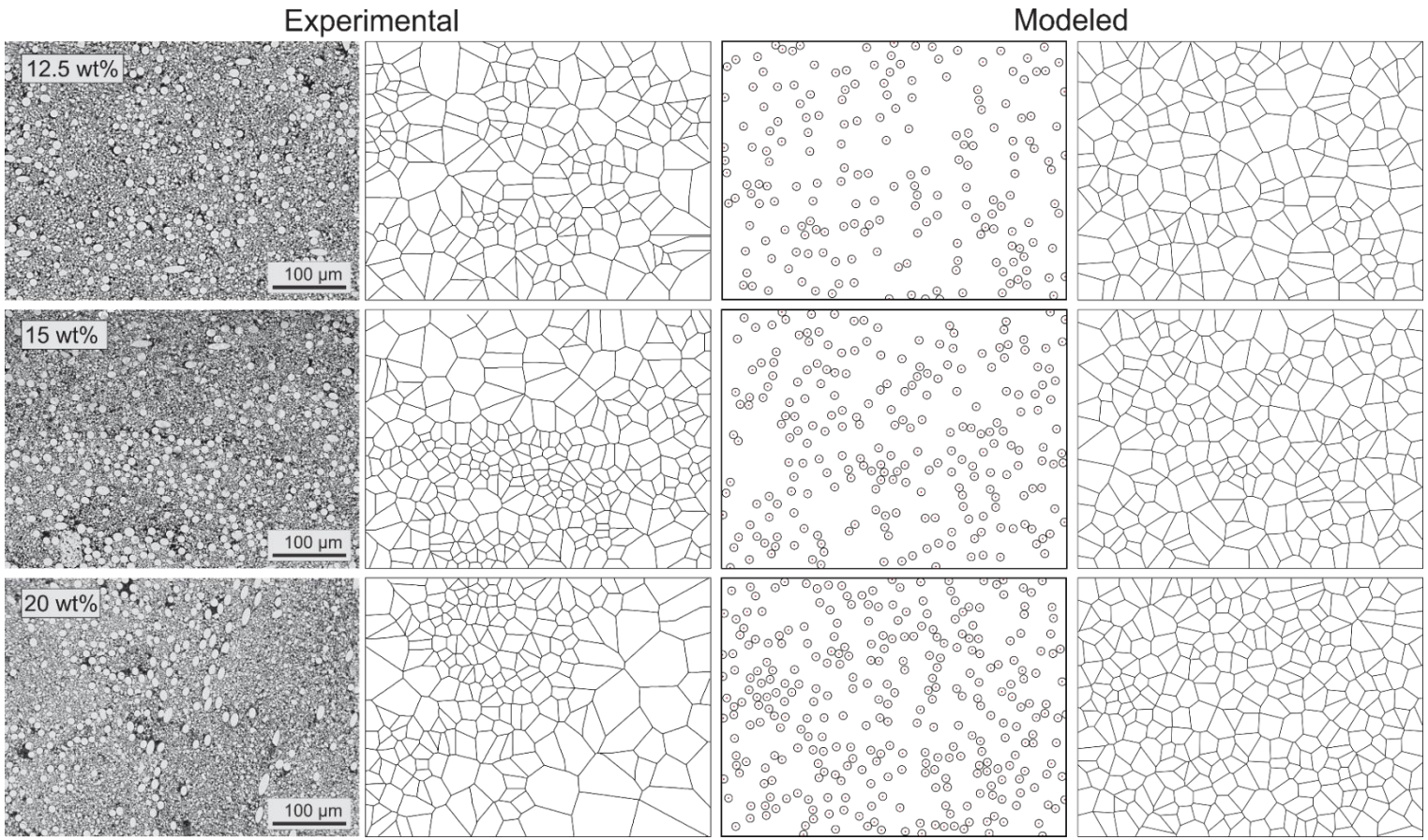


Figure 5.6: Cross-section micrographs (first column) of BMC composite samples with 12.5 wt%, 15 wt% and 20 wt% of EGFs and corresponding Voronoi diagrams (second column). Modeled patterns of fiber distribution and corresponding Voronoi diagrams are shown in the third and fourth column, respectively.

To gain deeper insight into the fiber distribution in composites with varying EGF content, a larger area of about 1.6 mm^2 was further analyzed with the Voronoi diagram analysis. In this case, all 9 areas of the cross-sectional positions of the individual BMC composite sample were included in the analysis. The mean average size, standard deviation and HP_A of Voronoi polygons are listed in Table 5.2. The relative frequencies of the Voronoi polygon size areas from experimental and computer simulated microstructures are presented in Figure 5.7. The deviation of the experimental distribution from the modeled one is a measure of randomness and pronounced fiber clustering.

The distribution of Voronoi polygon size areas in the composite with 5 wt% of EGF is quite broad due to a high number of smaller and larger polygons. This is a consequence of the local areas filled only with polymer resin and mineral filler that are present in the microstructures at lower weight fractions of EGF. Therefore, individual fibers are more isolated and to a greater extent surrounded by the matrix as previously shown in Figure 5.4. Hence, the spatial distances between the fibers are quite large in some areas, resulting in larger areas of the Voronoi polygons as supported by large mean value of polygon area size (2158 µm). If we compare the experimental and modeled distributions of Voronoi polygon areas, the distributions are very similar.

Even greater coincidence of the experimental and modeled distributions is observed in the sample with 7.5 wt% of EGF – meaning that the distribution of fibers in the experimental microstructures most closely approximates to random. Both distributions are also slightly narrower due to a higher number of fibers and thus smaller polygon areas (see Table 5.2). The most homogeneous fiber distribution in this sample is supported by the lowest HP_A value (0.68).

Further on, as the EGF content increases from 10 wt% onwards, the histograms of the experimental distributions again become broader, containing smaller and larger polygon areas. Conversely, the histograms of the modeled random distribution become narrower, with the peak shifting towards higher values.

Due to closer packing of the fibers at higher weight content of EGF, the areas of Voronoi polygons become smaller. The mean value of the Voronoi polygon area size drops from 1121 µm to 619 µm for the samples containing 12.5 wt% and 20 wt% of fibers, respectively. Moreover, also the HP_A values confirm the trend of increasing inhomogeneous fiber distribution with increasing fiber content [121]. Likewise, at higher EGF content, i.e. at 15 wt% and 20 wt%, the divergence of the experimental distribution from the modeled one is even more apparent. This could be primarily related to the fiber clustering in the microstructure, where the distances between the fibers are equidistant only locally rather than across the whole pattern. Especially pronounced occurrence of smaller polygons is found in the case of the composite with 20 wt% of EGF, where the peak maximum in the experimental distribution shifts towards a smaller polygon area and which is indicative for fiber clustering. Similar findings were found in [43, 45], where the distribution of Voronoi polygon areas for an inhomogeneous microstructure was broader, with a tail extending to larger polygon areas. These observations, the coexistence of relatively small and large Voronoi polygons, which results in a broad distribution, are characteristic for the clustered patterns, as was demonstrated by Tanaka et al. who analyzed computer-simulated clustered point patterns [122].

In general, one can observe that the histograms of modeled random fiber distributions are narrower and their peak is higher when the fiber content is increased. These observations suggest more uniform fiber distribution at higher fiber content, which is the consequence of more equidistant fibers in a smaller available space for each fiber. For comparison, in a perfectly ordered point pattern the distribution of polygon areas would be expressed by a single peak [122], meaning that all the distances between the second phase inclusions are equal. On the other hand, the experimental histograms have a similar

width and a shift to smaller polygon areas at higher fiber content. This behavior shows that in the experimental samples, the clustering, which counteracts the uniformity, is much more prevalent with increasing fiber content [123].

Table 5.2: Mean area size (μ_A), standard deviation (σ_A) and homogeneity parameter HP_A of Voronoi polygons.

	EGF weight content (wt%)					
	5	7.5	10	12.5	15	20
μ_A (µm)	2158	1573	1112	1121	857	619
σ_A (µm)	1536	1076	836	905	837	697
HP_A	0.71	0.68	0.75	0.81	0.98	1.13

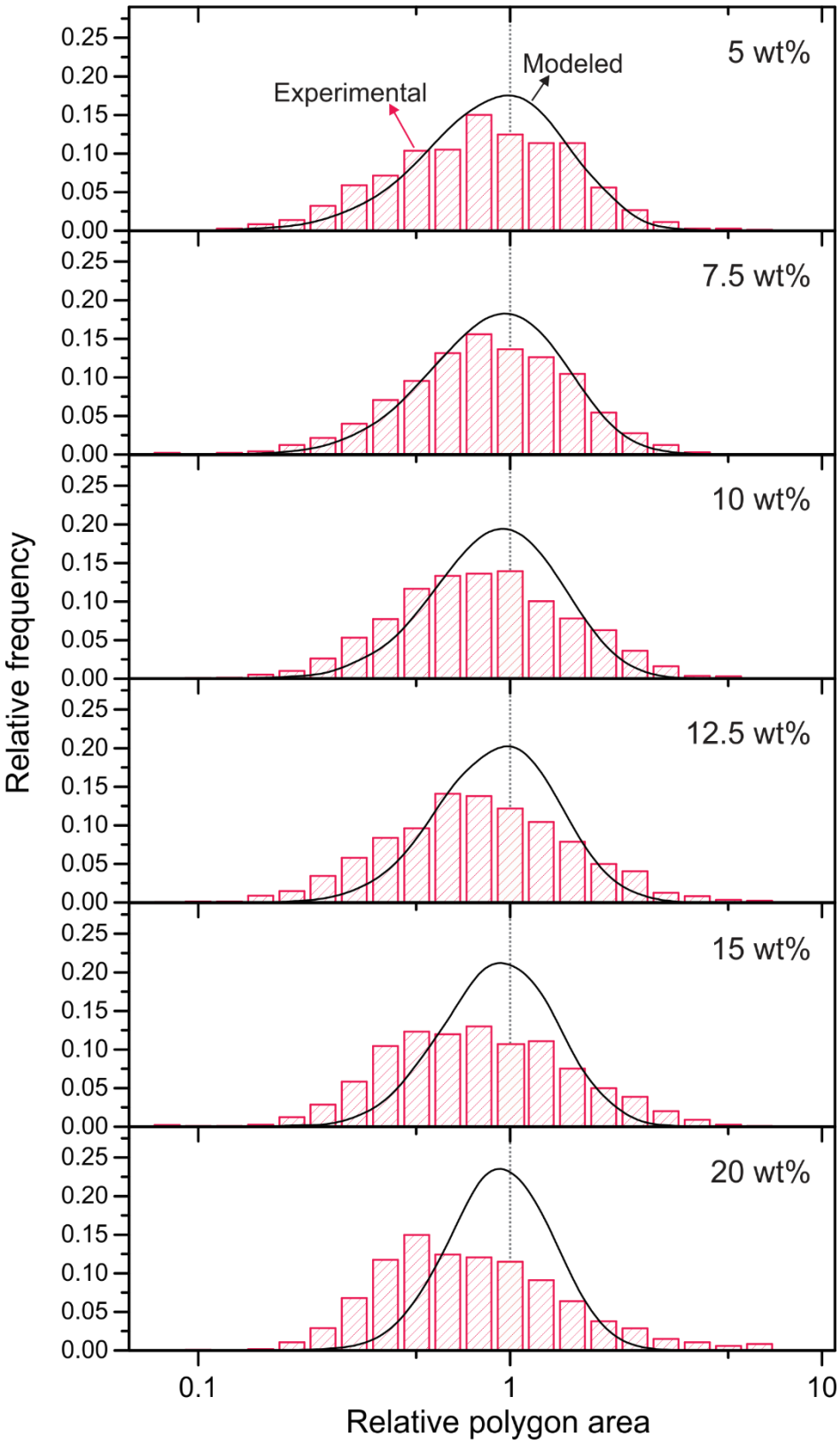


Figure 5.7: Distribution of Voronoi relative polygon areas of experimental and modeled fiber distributions of BMC composites with varying EGF weight content.

5.1.1.3 Radial distribution function

In addition to Voronoi diagram analysis, the fiber arrangement, fiber clustering and local disorder in composites were characterized by RDF. The RDFs of experimental and modeled random patterns with varying EGF weight fractions are presented in Figure 5.8. The experimental RDFs include all 9 analyzed areas of BMC composite samples with EGF content from 5 wt% to 20 wt%.

Applying to all BMC samples, the experimental and modeled RDFs at distances below the fiber diameter (<10 µm) are equal to 0, due to the constraint that the fibers cannot interpenetrate each other. The RDFs of modeled random distributions are flat and almost equal to 1 in the entire distance range, which coincides with the data reported in the literature for the random patterns. A subtle deviation from the value 1 at a distance of ~10 µm–20 µm is due to the Hard Core model that restricts the overlapping of fibers [48, 51].

After the distance of the closest approach, i.e. of about 10 µm, the experimental RDFs increase rapidly above 1, exhibiting a large maximum, meaning that the number of fibers found at this particular distance is much higher as compared to the random model. Or otherwise, every maximum and minimum in the RDF over the distance range corresponds to the most frequent and to the least frequent distances between the reference fiber and neighboring fibers, respectively. Therefore, every peak maximum in the experimental RDF indicates that the fiber density at this specific distance is considerably higher than the average density calculated from the modeled random fiber distribution.

As shown in Figure 5.8, the experimental RDF values are higher than the RDF values calculated from modeled random patterns in all composite samples, especially at short range distances (for example below 40 µm). At a long range, as the distance r grows, RDF declines and approaches to a constant value of 1 implying that the variations in fiber density are dissipating with increasing distance [52, 124] which is characteristic for a statistically homogeneous microstructure [48, 52].

The data points of the experimental RDF of the sample with 5 wt% of EGFs are quite scattered along the entire distance range as compared to RDFs of other samples. Moreover, high peak maximum at ~11 µm, exceeding the value of 1.75, demonstrates increased fiber density. This could be explained by the presence of areas containing only matrix on the one side and areas where the number of fibers is relatively higher on the other. Such fiber distribution at 5 wt% of EGFs is evidenced from the SEM micrographs and from the size of the Voronoi polygons in the previous chapter (see Figure 5.4 and Figure 5.5). At a lower fiber content, the fibers tend to be more isolated or arranged into smaller groups surrounded by a larger area of the matrix, which is expressed as the scattering of RDF values confirming that the microstructure is not uniform.

A good agreement between the experimental and modeled RDFs is found for the sample with 7.5 wt% of EGFs, demonstrating that the fiber distribution in this sample most closely approaches the random fiber distribution. Moreover, as previously confirmed with the Voronoi diagram analysis, the fiber distribution was the most homogeneous in this particular sample (see Figure 5.7).

As the fiber content in the composites increases above 10 wt%, the peak at the distance just above the fiber diameter becomes even higher and the difference between experimental and modeled RDFs becomes more apparent. This is especially pronounced at 15 wt% and 20 wt% of EGFs where the RDF peak maximum at ~11 µm is considerably higher. These results, which affirm the increased fiber clustering at higher fiber content, are in agreement with the study of Pyrz [52] who demonstrated that the RDF peak intensity of modeled point patterns is higher in clustered distributions as compared to the random point distribution. Furthermore, the experimental RDF values reach the values of modeled RDF

at larger distances (i.e. above 100 µm for the sample with 20 wt% of EGF) as compared to the samples with a lower EGF content. According to Pyrz [48], the distance r at which the experimental RDF first reaches the constant value of the modeled random RDF, defines the scale of local uniformity. These distances are indicated by arrows in Figure 5.8. It follows that the local disorder of composite microstructures is increasing with increasing fiber content. Short to medium range (<90 µm) local disorder is observed in composites with fiber fractions up to 12.5 wt%, where the smallest coincidence distance (~40 µm) was found for the composite with 7.5 wt% of fibers. However, the exception is the composite containing 5 wt% of EGF, where distribution function exhibits quite large fluctuations over the distance range. As explained earlier, in this sample the homogeneity or uniformity of the microstructure is disrupted by the presence of large matrix areas that are surrounding isolated fibers or groups of fibers. The extent of local microstructure disorder is especially noticeable in the composites with 15 wt% and 20 wt% of EGF, where the coincidence of the experimental and random RDF is reached at larger distances of ~100 µm and ~130 µm, respectively.

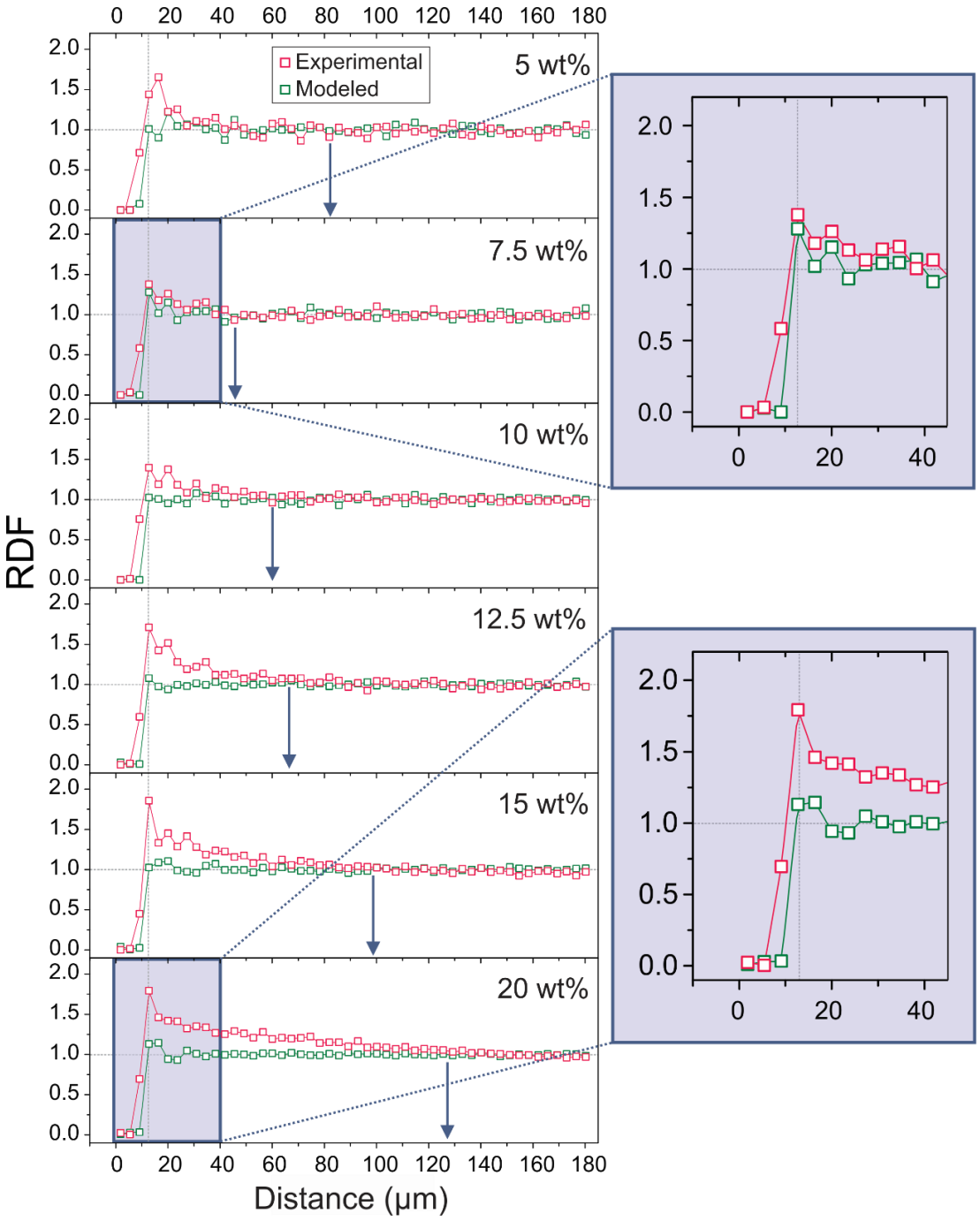


Figure 5.8: RDFs of experimental and modeled fiber distributions (from 5 wt% to 20 wt% of EGFs). The RDFs of the samples with 7.5 wt% and 20 wt% of fibers in the distance range from 0 μm to 40 μm are enlarged on the right. In the first case the experimental and modeled RDFs are very close, meanwhile, when the fiber content increases, the difference between the experimental and modeled RDFs becomes more pronounced indicating inhomogeneous fiber distribution. The arrows denote the scale of local microstructure disorder.

5.1.1.4 Elongation parameter

The mean value of the elongation parameter (EP) and the EP distributions for BMC composite samples containing 5 wt% to 20 wt% of EGFs are shown in Figure 5.9 and Figure 5.10. The EP is expressed as the ratio of the longest and the shortest axis of the fiber intersection and equals to 1 for a perfect circle. Most of the studies described fiber orientation with orientation tensors [26] or orientation angles derived from the measurement of circular or elliptical fiber profiles, but we could not find any work where EP was introduced as the descriptor for fiber orientation characterization.

For the sample with 5 wt% of EGFs the mean EP is 1.18 which demonstrates that the fiber intersections are mostly circular and thus predominantly aligned parallel with the filling flow direction during the molding process. Similar results are observed in the case of the sample with 7.5 wt% of EGFs, where a slightly higher EP value, i.e. 1.21, is calculated. These observations are in agreement with the work of Fu et al. [55], where the authors observed preferential fiber alignment in the flow direction from the SEM micrographs of the fractured specimens of polypropylene composites reinforced with 8 vol% of short glass fibers. Fiber orientation in the direction of the filling flow was also observed by Takahashi and Choi [27] in short glass fiber reinforced poly(ethylene terephthalate) composites.

When the fiber weight content increases, the mean value of EP shifts towards higher values and is in a range from 1.30 to 1.42 for the sample with 10 wt% and 20 wt% of EGFs, respectively.

The EP distributions of composites with different fiber fractions are shown in Figure 5.10. From the histograms of all composites, it is evident that the fibers are predominantly oriented parallel to the filling flow direction which is indicated by a peak value slightly above 1. The peak intensity is higher when the fiber content is low (5 wt%), meaning that the majority of fibers are visible as circles in the samples cross-section. However, since the fibers have quite a lot of available space to orient, we can find some exceptions (fibers aligned perpendicular to the filling direction) as indicated by higher values found in the EP distribution (see the inset of the sample with 5 wt% in Figure 5.10). When fiber content in composites increases, the peak intensity just above 1 is gradually decreasing and the distribution is becoming broader as evident from the insets in Figure 5.10. The peak intensity is the lowest and the distribution is the broadest in the composite containing 20 wt% of fibers. This demonstrates that there is still a majority of fibers oriented parallel with the filling flow, but there is an increasing number of fibers oriented transversely to the flow. As in agreement with SEM micrographs, round to highly elongated intersections of fibers are found in the cross-section of the microstructure (see inset in Figure 5.9).

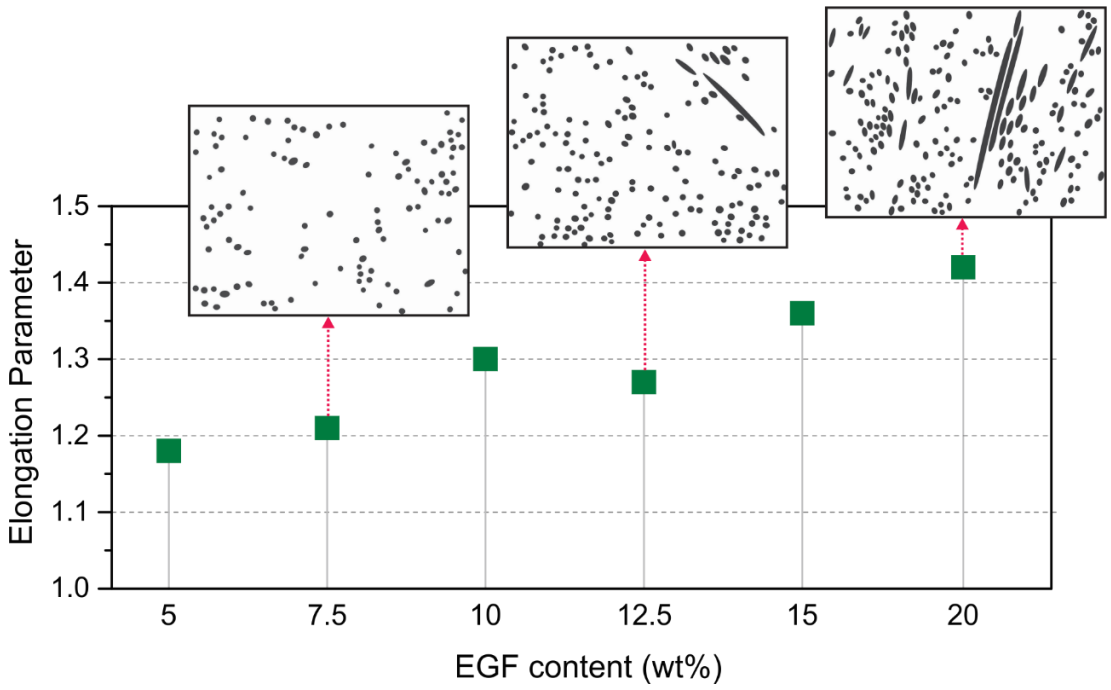


Figure 5.9: The mean values of EP of BMC composites with different EGF weight fractions showing that the EP is increasing with increasing fiber content. As evident from the representative BMC microstructures (insets of black fibers on white background), at higher fiber content some of the fibers also orient in different directions as a consequence of smaller available space.

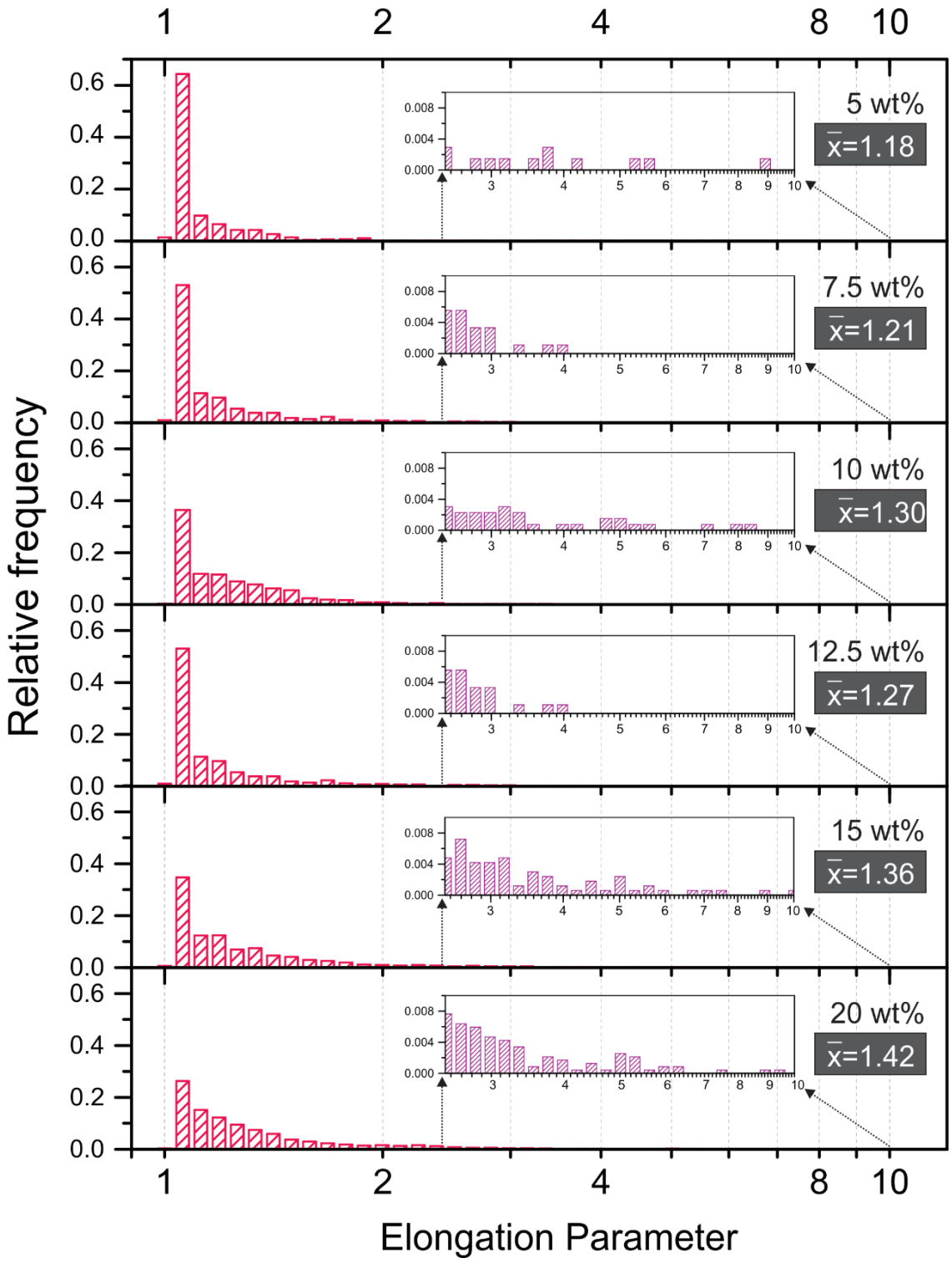


Figure 5.10: EP distributions of BMC composite samples with 5 wt% to 20 wt% of EGF content.

5.1.2 Microstructure of BMCs with EGF weight content from 25% to 35%

The microstructures of composites with higher fiber weight fractions were not quantitatively characterized. The reason is that a high disorder as well as faults in the material were already visible from the SEM micrograph. Moreover, the molding of BMC composites with fiber weight fractions above 25 % becomes difficult and complicated, as discussed later in this section.

SEM images of plan-view and cross-sectional areas of BMC composite samples with EGF content from 25 wt% to 35 wt% are shown in Figure 5.11. The micrographs were taken arbitrarily across the sample surface and the cross-section area.

Microstructures of composites having a high fiber content show a dense fiber arrangement in the matrix. As evident from the plan-view microstructures (left side in Figure 5.11), the fibers are grouped in clusters having the same preferred fiber orientation direction as indicated by arrows in Figure 5.11. However, the majority of fibers is still oriented parallel with the direction of the molding compound flow during manufacturing. This is evident from the cross-sectional microstructures (right side in Figure 5.11) displaying predominantly circular fiber intersections. Nevertheless, there is also a larger number of fibers oriented transversely or perpendicular to the filling flow, which contributes to the occurrence of regions filled only with the matrix phase. As already shown in the previous section, the increase in fiber content gives rise to the inhomogeneous microstructure and increased fiber clustering. Figure 5.12 shows two arbitrary taken SEM micrographs of the cross-sectional area of BMC composite sample containing 30 wt% of fibers. The difference in fiber density is clearly seen, which confirms high local disorder of the microstructure.

In SEM micrographs (see Figure 5.11) of all composites we observed insufficient wetting of fibers and the presence of voids, which are visible as dark fields between the individual fibers. High fiber content presumably leads to the faults in the composite material and results in a weak adhesion between the fibers and the matrix, which strongly influences the mechanical response of composites, as discussed later in Chapter 5.2. Our observations are consistent with the findings of Salman et al. [125] who studied the influence of kenaf fiber content, i.e. from 10 wt% to 60 wt% with a 10 wt% increase, on mechanical and morphological properties of polymer-matrix composites. The authors reported an increase in tensile, flexural and impact strength with increasing kenaf fiber content up to 40 wt%. Afterwards the mechanical properties were decreased. The authors reported that the reason for failure of composites with fiber content above an optimum value are insufficient wetting of fibers with the polymer matrix and too small spacing between the neighboring fibers in order to effectively transfer the stress between the fibers and the polymer matrix. The morphological characterization of composites with fiber content above the optimum (50 wt% and 60 wt%) revealed entanglement of fibers, poor wetting and increased porosity.

Moreover, SEM micrograph of the BMC composite with 30 wt% of EGFs in Figure 5.13 shows micro cracking and bending of fibers. It was demonstrated that higher fiber content leads to increased fiber damage and fiber breakage [55, 58], and this is also evidently happening in our case.

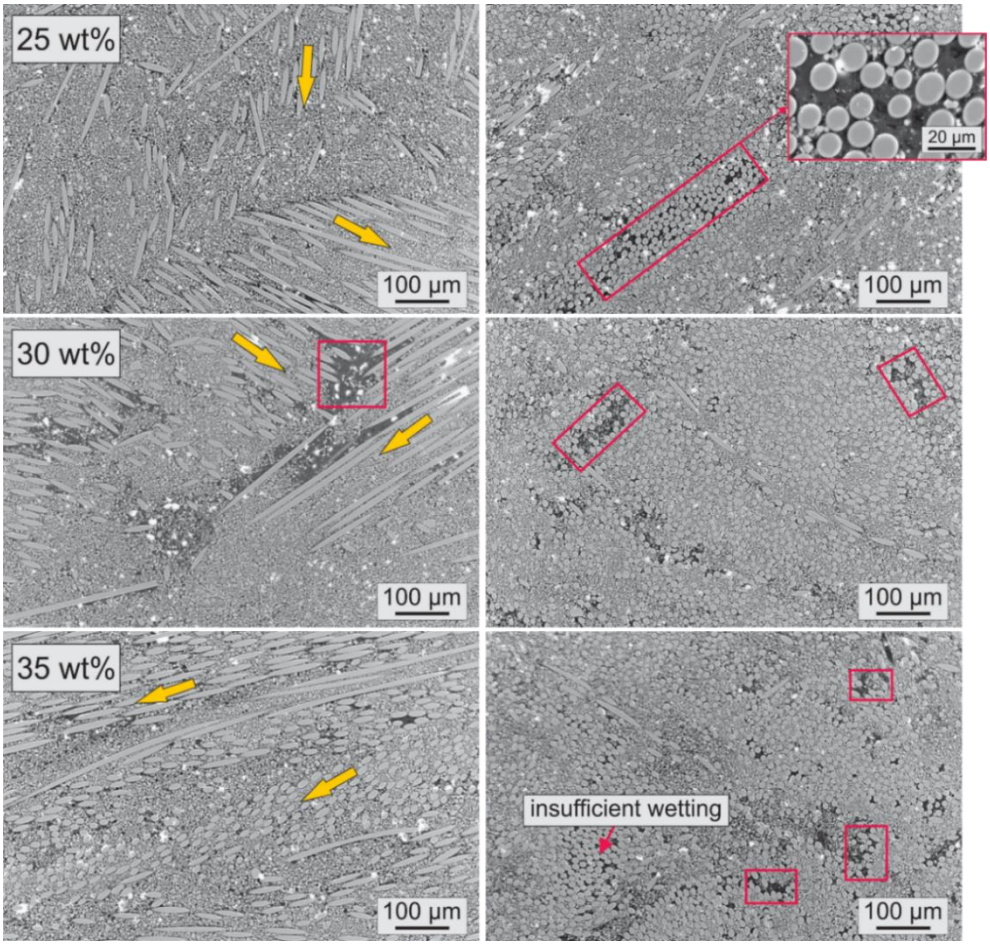


Figure 5.11: Micrographs of the plan-view (left) and cross-section areas (right) of BMC composite samples with 25 wt%, 30 wt% and 35 wt% of EGFs. At higher fiber weight fractions the microstructure is highly disordered, resulting in groups of fibers with the same orientation direction, poor wetting of fibers and increased porosity.

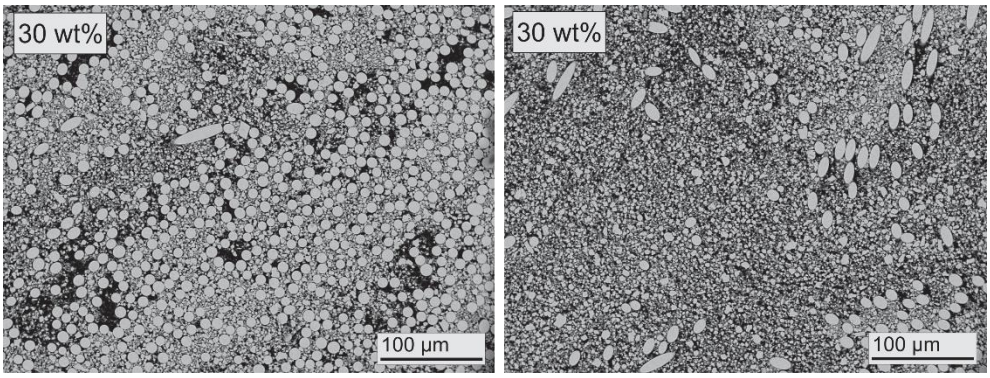


Figure 5.12: Cross-section SEM micrograps of BMC composite sample containing 30 wt% of EGFs where the difference in fiber density is clearly seen. These observations confirm high local disorder of the microstructure.

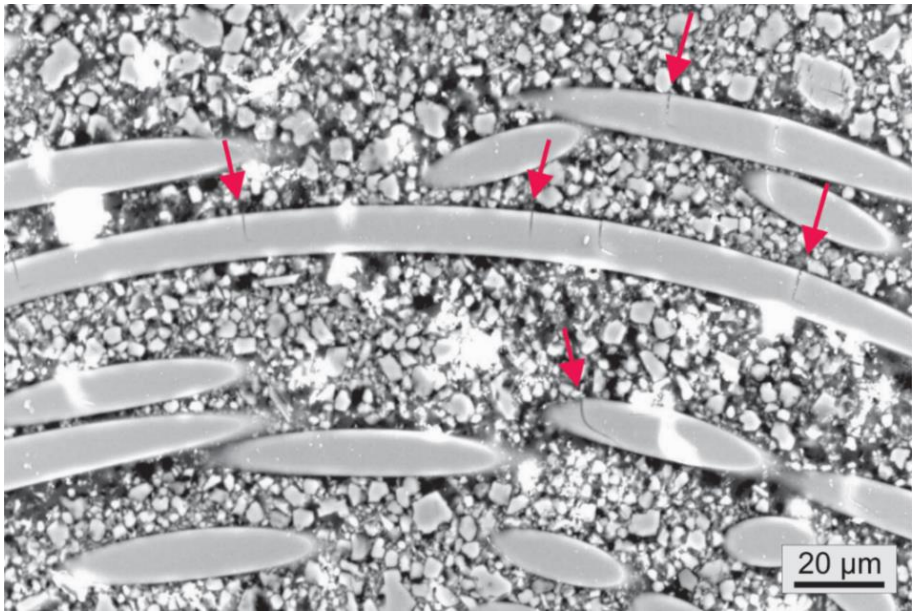


Figure 5.13: Micro cracks of EGFs observed in the sample with 30 wt% of fiber content. At higher fiber content the fibers are heavily loaded and bent which results in increased fiber cracking and breaking.

5.1.3 Summary

In this section we addressed the microstructural characterization of BMC composite samples with varying glass fiber weight fractions. Different tessellation-based methods, statistical methods and stereological analyses were applied in order to characterize the microstructures of BMC composites with fiber content from 5 wt% to 20 wt%. The modeled random distribution of fibers, constructed for individual composition, served as a reference in order to evaluate uniformity of fiber distribution. The main findings of this chapter are summarized hereafter.

Voronoi diagram analysis

- The mean area size of Voronoi polygons decreased with increasing fiber content (5 wt% → 20 wt%) due to a higher number of fibers present in the material and thus smaller distances between the neighboring fibers.
- Fiber distribution in the individual composite (5 wt%, 10 wt%, 15 wt% and 20 wt%) varies locally as evident from the comparison of cross-sectional areas 1, 5 and 9. Local microstructure disorder is to a greater extent expressed in composites with higher fiber content (15 wt% and 20 wt%), as confirmed by higher and more scattered HP_A values.
- Fiber clustering, expressed as the presence of small and large Voronoi polygons, was pronounced at higher fiber content, especially in composites with 15 wt% and 20 wt% of EGFs.
- As confirmed by the HP_A values the uniformity of fiber distribution in the matrix gradually decreased with increasing fiber content. The HP_A values were from 0.71 to 1.13 for the composite with 5 wt% and 20 wt% of EGFs. However, among all the samples, the HP_A value for the composite containing 7.5 wt% of fibers was the smallest (0.68) implying the most homogeneous fiber distribution.

- The deviation of the experimental Voronoi polygon area size distribution from the modeled one is becoming more pronounced with increasing fiber content. The distribution becomes broader with a peak maximum shifting to smaller polygon areas, which is characteristic for increased fiber clustering. Such observations were particularly evident in the composite with 20 wt% of EGFs. The best coincidence of the experimental and modeled distribution was found for the sample with 7.5 wt% of fibers.

Radial distribution function

- The difference between the experimental and modeled RDF becomes more apparent with increasing fiber content – the peak at the distance of the closest approach, 11 µm, is shifting to higher values suggesting inhomogeneous fiber distribution and more pronounced fiber clustering. The best compliance between the experimental and modeled RDF was observed for the composition with 7.5 wt% of EGFs.
- The range of local microstructure disorder is broadening with increasing fiber content. The distance at which the experimental RDF reaches the modeled one was found to be around 100 µm and 130 µm for composites with 15 wt% and 20 wt% of fibers, respectively. The scale of local disorder was found to be the smallest in the composite containing 7.5 wt%, ~40 µm.

Elongation parameter

- The fibers in composite samples are mostly oriented parallel with the flow direction of the molding compound during the molding process, especially at lower EGF contents as demonstrated by the EP mean value (1.18). With increasing fiber content, the EP increases to the value of 1.42 for the composite with 20 wt% meaning that some fibers orient in other directions as well.
- However, even at higher fiber content the majority of fibers in a particular composite are oriented parallel with the filling flow, as evidenced from the EP distribution where the peak maximum at a value of 1 is pronounced.

The microstructures of composites with high EGF content from 25 wt% to 35 wt% show dense fiber packaging and a highly disordered microstructure. The fibers are grouped into clusters and although the fiber packaging is quite dense, areas filled only with matrix phase are also found. Faults in the composites, such as poor wetting of fibers, increased porosity and fiber damage were observed from the SEM micrographs.

5.2 Mechanical Properties

5.2.1 Flexural strength

Flexural strength and flexural modulus of BMC composites with EGF weight fractions from 0 wt% to 35 wt% in 5% intervals are shown in Figure 5.14. The flexural strength of the composite containing no fibers is 55 MPa. With the addition of 5 wt% of glass fibers the flexural strength increases to 73 MPa. The flexural strength strongly increases with increasing EGF content, reaching the peak values between 110 ± 8 MPa and 121 ± 16 MPa for the EGF fractions between 10 wt% and 15 wt%, respectively. With further EGF content increase, the flexural strength noticeably decreases, reaching the value of 72 MPa for the sample with 35 wt% of EGFs, which is similar to the value obtained for the sample with the lowest fraction of EGFs. Flexural modulus of the composites also increases with

increasing EGF weight content and the enhancement is the greatest at lower fiber weight fractions. The addition of 5 wt% of fibers into the matrix increases the flexural modulus from 14 GPa to 15 GPa, respectively. Further on, the flexural modulus increases to 17 GPa for the composite with 15 wt% of fibers, and with further EGF content the modulus remains almost unchanged.

Here, we would like to note that we observed a variation in flexural strength between different series of composite samples. While the values for the samples from the first two series were reproducible, the third series of the samples with 5, 7.5, 10, 12.5, 15 and 20 wt% of EGFs exhibited lower values that are listed in Table 5.3. A probable reason for such difference is attributed to differences in the compounding process – namely the mass of individual compound batches in the third series was four times less than in the first two, 5 kg versus 20 kg. Although the strength values in the third series are downshifted, the flexural strength dependence on the EGF fraction follows a similar trend as evident in Figure 5.14: the existence of a peak strength value at a certain EGF content.

The increase in flexural strength only to a certain content of fibers, followed by a decrease, is in accordance with other studies [58, 61, 62, 70, 125] investigating the effect of fiber content on mechanical properties. Similarly, the almost linear increase of flexural modulus for up to 15 wt% is consistent with [58].

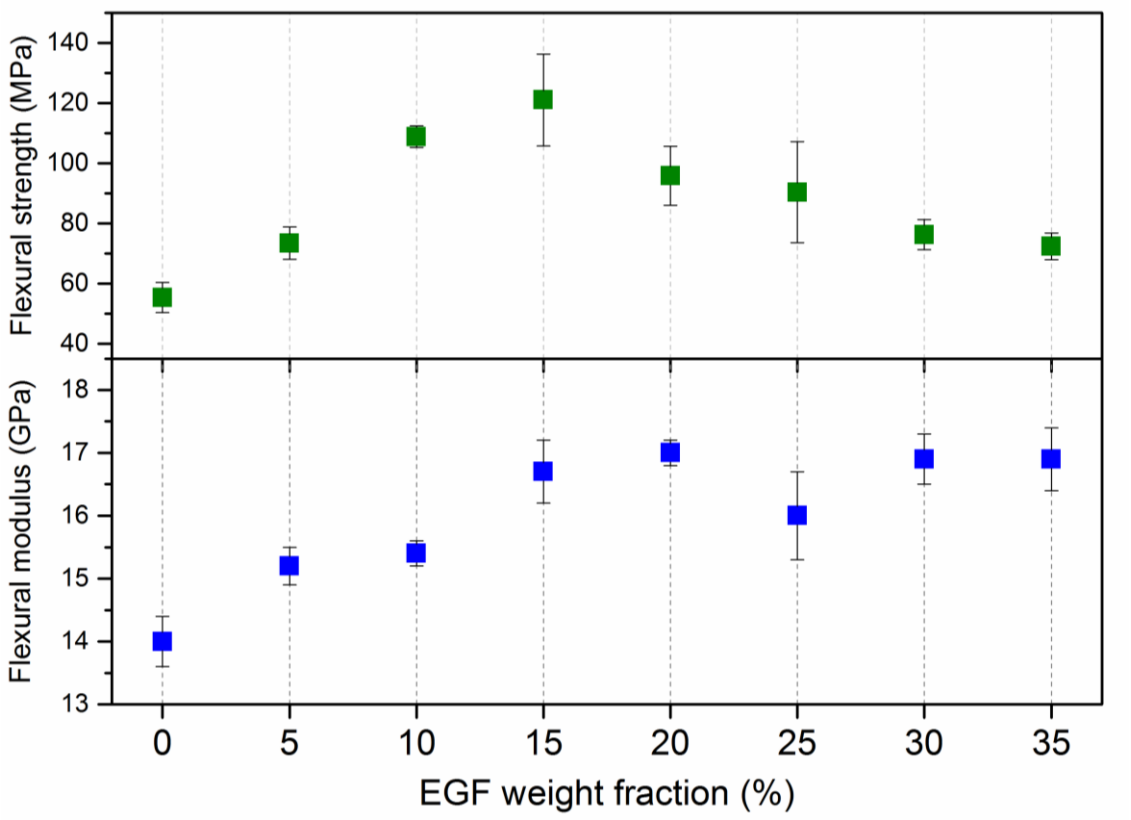


Figure 5.14: Flexural strength and flexural modulus of BMC composites as a function of EGF content. Flexural strength is increasing with increasing EGF weight fraction, reaching the peak value at 15 wt% of EGFs. Flexural modulus also increases with increasing EGF content up to 20 wt% and with further increase in EGF content it remains constant.

Table 5.3: Flexural strength of BMC composites with 5 wt%–20 wt% of EGFs (the third series of BMC samples).

EGF (wt%)	5	7.5	10	12.5	15	20
σ_f (MPa)	61±3.1	73±6	82±4.7	76±6.6	72±7.2	61±3.3

We note that the compositional range of the highest flexural strength values between 10 wt% and 15wt% is shifted to slightly higher EGF fractions if we compare it with the range of the highest microstructural uniformity. Both Voronoi and RDF analyses revealed that the microstructure exhibiting the highest level of homogeneity, i.e. the best match with the modeled microstructures, was at 7.5 wt% of EGFs, compare Figure 5.7 and Figure 5.8. This means that in addition to a homogenous distribution, a certain high enough fraction of EGFs is needed to reach a high flexural strength.

The reason for the flexural strength reduction at EGF fractions exceeding 15 wt% can be explained by the fiber distribution inhomogeneity and fiber clustering. The latter are especially pronounced in the composites with ≥ 20 wt% of fibers as confirmed in the previous chapter by Voronoi and RDF analyses. The non-uniformity of the microstructure, i.e. clustering of the second phase inclusions, which results in fiber-depleted and fiber-rich areas, or presence of defects, such as voids, detrimentally influence the mechanical strength [24, 42, 63, 70].

The scheme in Figure 5.15 shows how the increase in the strength of composites depends on the fiber orientation at a given fiber fraction [22]. In case where the fibers are oriented in the direction of the applied stress, the enhancement in the strength is the highest, as opposed to the case where the fibers are aligned in the perpendicular direction. The microstructural analysis revealed that in the samples with high EGF contents some fibers orient almost across the filling flow direction, see Figure 5.2, Figure 5.3, and Figure 5.11. This is further evidenced by the elongation parameter analysis, which revealed broadening of the distribution of the EP values with increasing EGF content, see Figure 5.9.

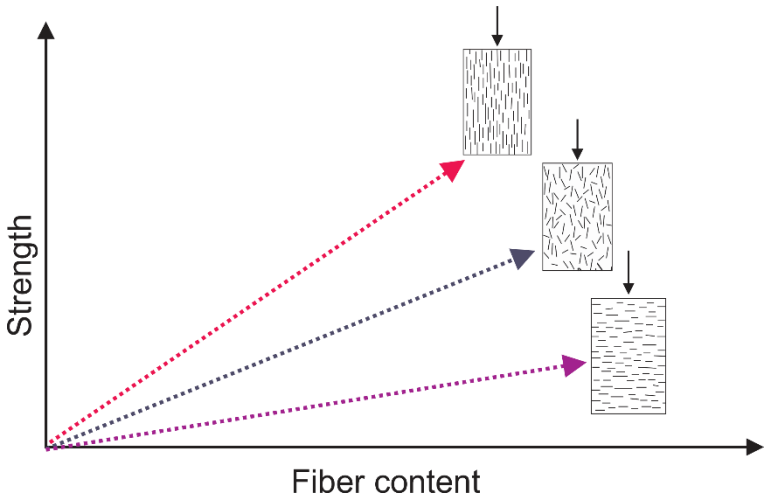


Figure 5.15: Dependence of the mechanical strength of composites on the fiber content. The strength increase depends not only on the fraction of the fibers but also on their orientation. The arrow denotes the direction of the applied stress.

5.2.2 Dynamic mechanical properties

The storage modulus, loss modulus and damping behavior of the studied BMC composites in the temperature range from 25 °C to 190 °C is shown in Figure 5.16. Evidently, the storage moduli of the composites increase with increasing EGF content, meaning that the fibers impart stiffness to the composite materials. A gradual increase in storage modulus from ~15 GPa to ~17.5 GPa is observed for the composites with fiber weight content from 0 % to 25 %, respectively, below the glass transition temperature at ~90 °C, see Table 5.4, as discussed later in this section. Above 25 wt% EGFs, the storage moduli decrease to ~16 GPa, presumably due to increased contacts between fibers, which hinder an effective stress transfer.

The storage moduli of the composites decrease with increasing temperature in the measured temperature range from ~16–17 GPa to ~5–6 GPa for the samples with different fractions of EGFs. Such decrease is consistent with literature [65, 66, 70, 71] and related to the transition from the glassy to the rubbery state [65].

The glass transition temperature is indicated by a peak in the loss modulus and $tan\,\delta$ curves and spans from 85 °C to 96 °C for different compositions, see Table 5.4. We observe that the EGF fraction does not have a systematic influence on the glass transition temperature of composites as in agreement with [65], and is thus only dependent on the polymer phase.

The reinforcing effect of the fibers on the storage modulus can be determined by the coefficient of reinforcement C. The values at temperatures of 40 °C and 160 °C were employed as the storage modulus values in the glassy (E'_g) and the rubbery state (E'_r), respectively. The lower the value of C, the higher the reinforcement [67–70]. The results for the studied composites are collected in Table 5.4. The lowest C value of 0.79 was obtained for the sample with 15 wt% of EGFs indicating the highest reinforcing effect. With fiber content above 15 wt% the coefficient of reinforcement gradually increases, reaching the highest value 1.03 for the composite with 35 wt% of fibers.

The loss modulus curves exhibit many fluctuations, especially below the glass transition temperature, see Figure 5.16, second row. At temperatures above the glass transition range (~90 °C) the loss moduli reach the peak values. The peak values span from ~6 GPa and 7.5 GPa for the composites with 5 wt% and 35 wt% of EGFs, respectively. The increase in the loss modulus with increasing fiber content is explained by the increased friction between the fibers and as a consequence more mechanical energy is dissipated [65, 67, 68].

The $tan\,\delta$ of the studied composites increases with increasing temperature. All the curves reach a peak in the temperature range from 91 °C to 103 °C, which corresponds to the glass transition range. The composite without the fiber reinforcement (0 wt%) exhibits the most pronounced damping corresponding to the easy mobility of polymer chains, which is especially pronounced above the glass transition temperature. With the incorporation of fibers such mobility is hindered, as indicated by the decrease in $tan\,\delta$ with increasing fiber content in the range from 5 wt% to 25 wt%. The lower $tan\,\delta$ value thus indicates better fiber-matrix adhesion and improved stress transfer between the fibers as in accordance with Pothan et al. [126]. As indicated by the $tan\,\delta$ values, the stress transfer is the most efficient in the composites with 15 wt%–25 wt% of EGFs. Relatively increased $tan\,\delta$ values for the EGF contents of 30 wt% and 35 wt% indicate weaker adhesion between the fibers and the matrix. This is in consistence with the SEM analysis, which revealed increased porosity, poor wetting of fibers with the matrix and pronounced fiber clustering in comparison to the samples with lower EGF contents (compare Figure 5.11). Similarly, a decrease in the damping behavior with increasing fiber content was reported in [66, 67, 71].

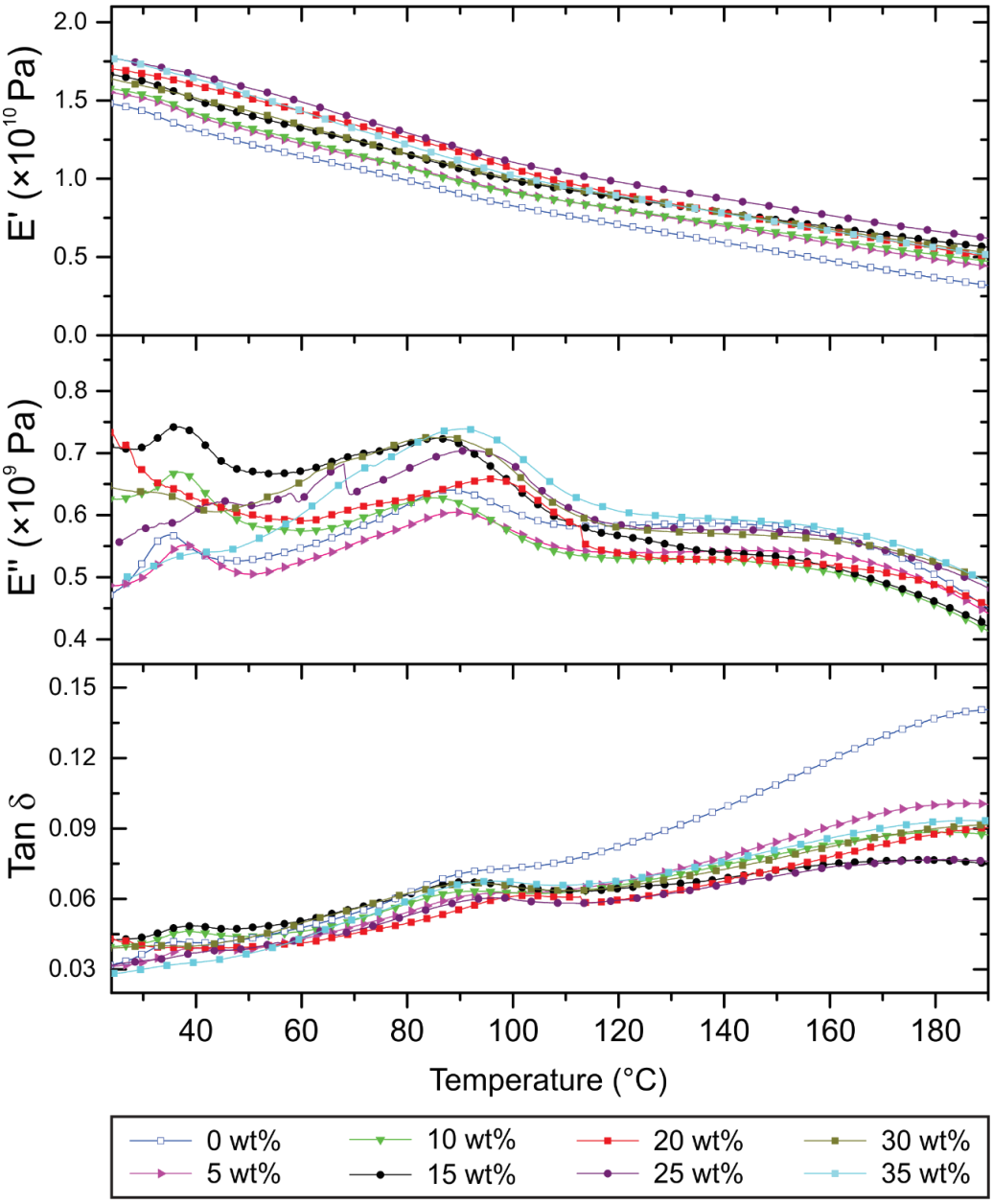


Figure 5.16: Storage modulus (E'), loss modulus (E'') and damping behaviour ($tan\ \delta$) of BMC composites with different fiber weight fractions in the temperature range from 25 °C to 190 °C.

Table 5.4: Glass transition temperature of BMC composites with different EGF weight contents as determined from the loss modulus curves and the coefficient of reinforcement C.

	EGF weight content (wt%)							
	0	*5*	*10*	*15*	*20*	*25*	*30*	*35*
T_g (°C)	87.75	89	84.75	85.75	95.75	90	85.5	88.5
C	-	0.86	0.85	0.79	0.87	0.91	0.93	1.03

5.2.3 Summary

The flexural strength of BMC composites is increasing with increasing EGF fraction, reaching the values of 110–120 MPa at the EGF fractions of 10–15 wt%. With higher EGF fractions the flexural strength progressively decreases. The peak strength value of 121±16 MPa at 15 wt% of EGFs is due to the interplay of the strengthening effect of the fibers, which is clearly more pronounced as the fiber fraction is increased, and microstructural uniformity, the latter being the highest at a slightly lower EGF fraction, at about 7.5 wt%. The decrease of the strength at EGF contents ≥ 20 wt% is a consequence of increasingly pronounced microstructural non-uniformity.
The dynamic mechanical analysis revealed that the storage modulus of the studied composites is increasing with increasing fiber content, meaning that the fibers impart stiffness to composites. The coefficient of reinforcement C, calculated from the respective moduli in the glassy and rubbery state, is the lowest, 0.79, in the composite with 15 wt% of EGFs, meaning that in this composite the reinforcing effect of the fibers is the highest.

Increasing fiber content in the composites contributes to a more pronounced inter-fiber friction and thus to higher losses of mechanical energy, which is especially noticeable at the highest EGF contents (30 wt% and 35 wt%).

5.3 Thermal Properties

In the beginning of this chapter we investigate the effect of EGFs on the crosslinking reaction in the BMC composite materials. We continue with the mechanism of thermal decomposition of the BMC composites. Finally, we explore the influence of different fiber contents on the specific heat capacity and thermal conductivity of BMC composites.

DSC curves of representative BMC composite materials with 0 wt%, 20 wt% and 30 wt% of EGFs recorded between 35 °C and 190 °C are shown in Figure 5.17.

A subtle endothermic event occurs in all samples below 100 °C and is most likely due to the moisture and volatiles evaporation. The onset of the exothermic crosslinking reaction of the unsaturated polyester is at around 125 °C. The crosslinking reaction in the composite with no EGFs (0 wt%) is accompanied by a strong exothermic peak at 131 °C and an even stronger exothermic peak at 153 °C, followed by a shoulder at about 170 °C. In the sample with 20 wt% EGFs the two exothermic peaks are slightly up-shifted, and their relative intensities are reduced. This is especially evident for the lower-temperature peak. In the sample with 30 wt% EGFs we observe only one broad exothermic peak at 162.5 °C. These observations imply that the EGFs hinder the cross-linking reaction of the UP matrix, as evidenced by temperature up-shifting and broadening of the major exothermic effect.

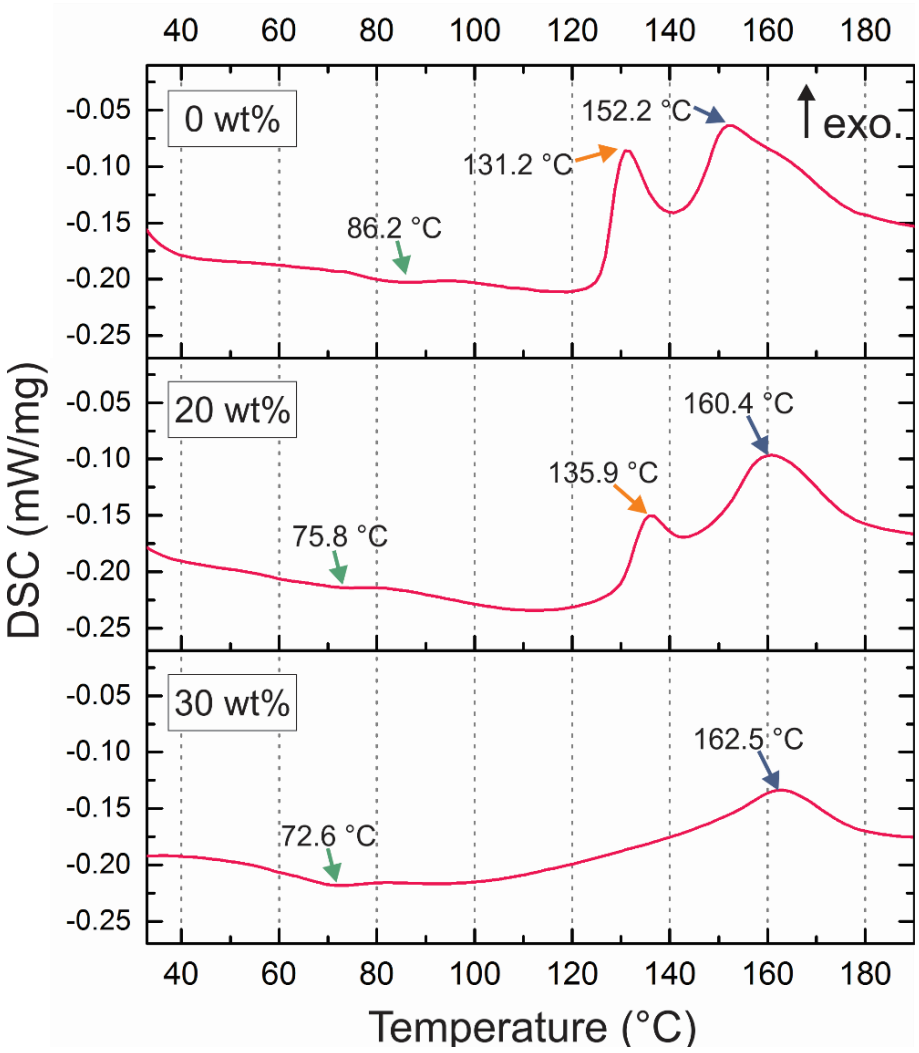


Figure 5.17: DSC curves of BMC composite materials before curing with 0 wt%, 20 wt% and 30 wt% of EGFs.

5.3.1 Thermal stability

Thermal decompositions of selected BMC composites were recorded by TG/DTA and are collected in Figure 5.18. The composites with 0, 10, 20, and 30 wt% EGFs are thermally stable up to ~200 °C with a minor weight loss as a consequence of evaporation of volatile species. Thermal decompositions of the composites with different weight fractions of fibers are similar – the thermal events occur at similar temperatures, only the intensities of DTA peaks at ~350 °C and ~400 °C are different. In all the samples the mass loss at 655 °C is between 20.08% and 21.83%, which is in good agreement with the initial weight content of the polymer phase, 21 wt%. Likewise, thermal decompositions of the samples with other EGF contents exhibit similar thermal decompositions, meaning that different amounts of fibers in the composites do not influence their thermal stability and decomposition.

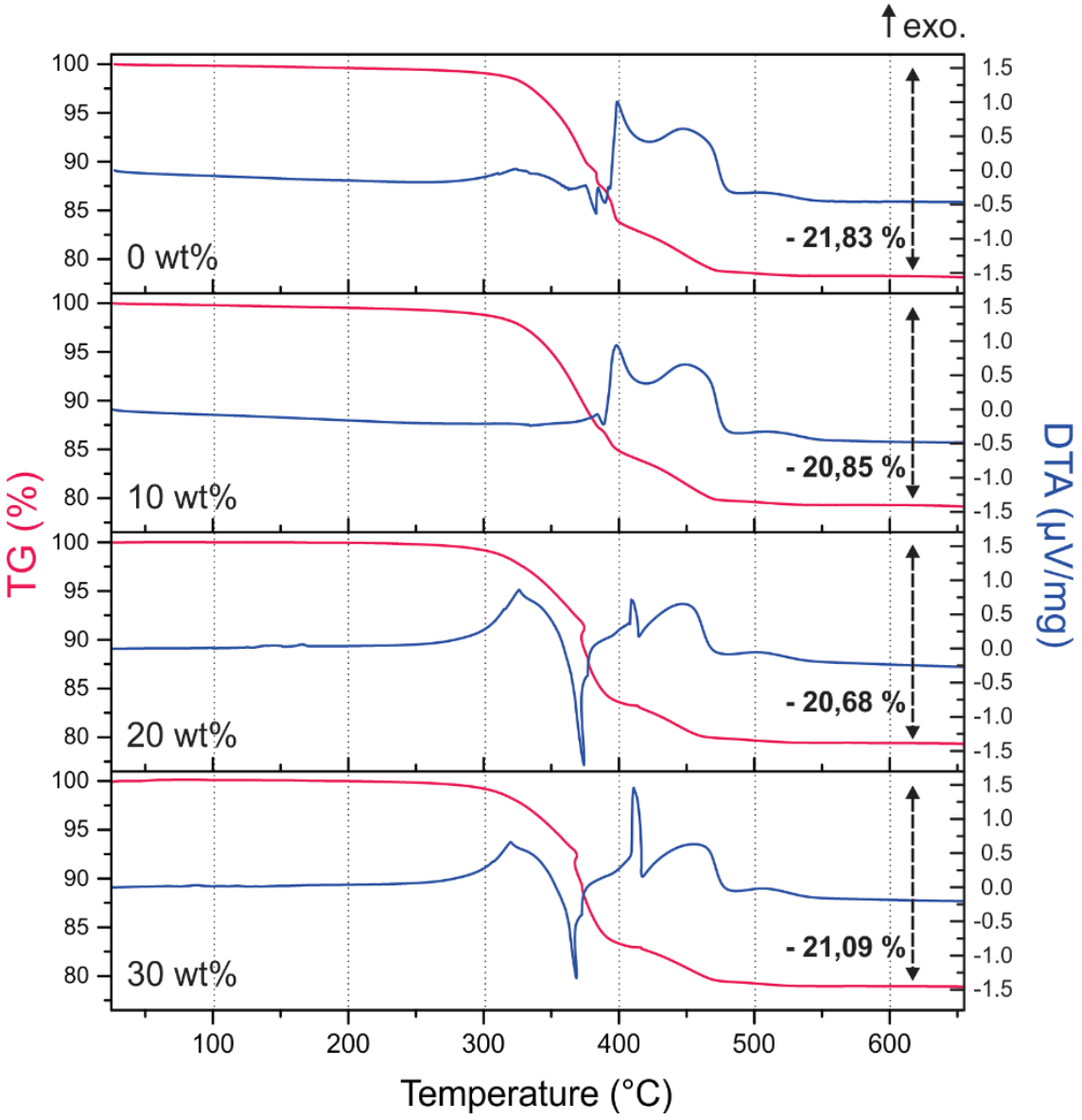


Figure 5.18: TG/DTA curves of BMC composites with 0 wt%, 10 wt%, 20 wt% and 30 wt% of EGFs recorded in synthetic air atmosphere.

A more detailed insight into the thermal decomposition of BMC composites is provided for the composite with 15 wt% of EGFs. The TG/DTA curves in the temperature range from 20 °C to 900 °C are shown in Figure 5.19. Upon heating to ~200 °C a minor weight loss accompanied by a weak endothermic effect is due to the loss of volatile species, i.e. water and entrapped styrene monomer.

The weight loss in the temperature range between ~200 °C and ~570 °C is 20.58%, which is in good agreement with the nominal organic content of 21 wt%. The weight loss is accompanied by endothermic (~367 °C) and exothermic (~332 °C, 414 °C, 456 °C and ~505 °C) events due to polymer chain scission and thermal oxidation [87, 127, 128]. According to Budai et al. [65] the decomposition of polyester starts at about 280 °C, while Evans et al. [129] reported that it starts to degrade at ~200 °C. During thermal decomposition of polyesters, around 90–95% of the initial mass decomposes to volatile

species resulting in a negligible amount of char [127]. According to Mouritz et al. [85] the char residue is less than 5%.

Upon further heating, above 660 °C, the thermal decomposition of the $CaCO_3$ mineral filler occurs, exhibiting an endothermic event at ~840 °C and a weight loss of ~28%, in agreement with [130]. The product of the decomposition, CaO, was confirmed by X-ray diffraction analysis, see Figure 5.20. The latter and the remaining glass fibers correspond to the solid residue of ~51% after the thermal treatment up to 900 °C.

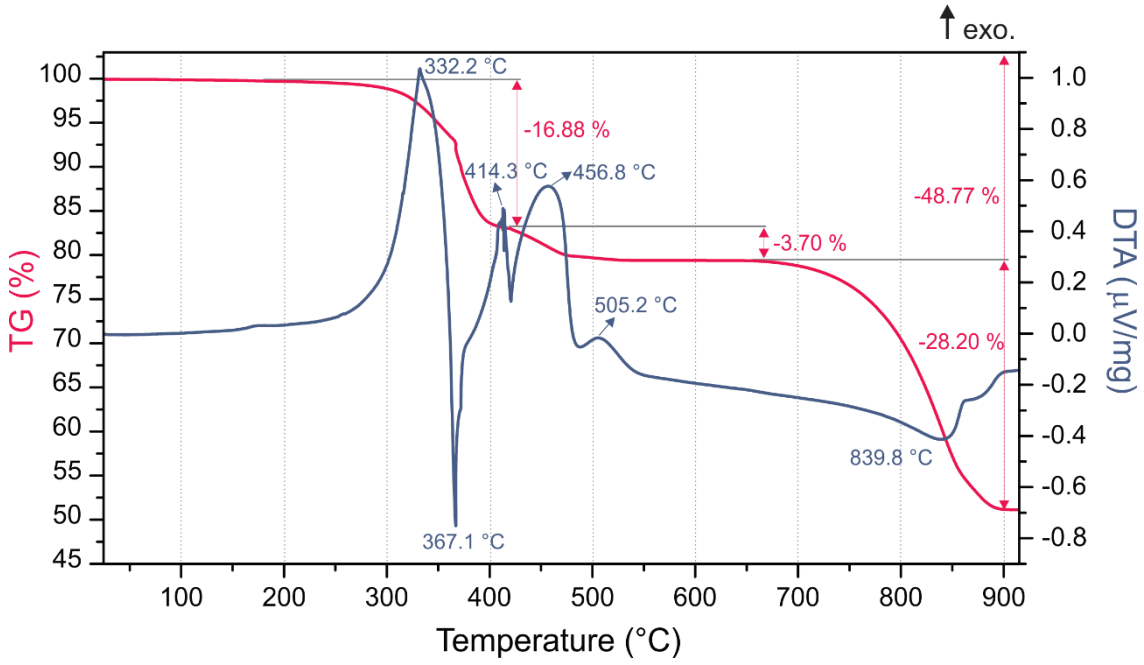


Figure 5.19: Thermal decomposition of representative BMC composite containing 15 wt% of EGFs.

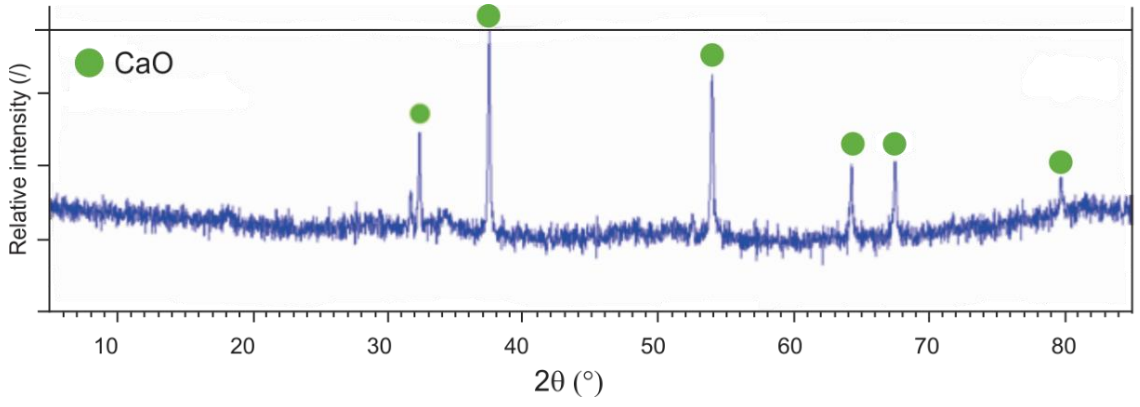


Figure 5.20: XRD pattern of the residue obtained after heating the BMC composite with 15 wt% of EGFs up to 900 °C. CaO is the crystalline phase in the thermal decomposition product.

5.3.2 Specific heat capacity

The specific heat capacity (C_p) values of BMC composites with EGF weight content from 0% to 35% at 20 °C, 100 °C and 180 °C are listed in Table 5.5. The specific heat capacity of all composites is increasing with temperature, in agreement with [131]. The C_p value of the composite without EGFs (0 wt%) is 0.899 J/gK at 20 °C and it increases with temperature to 1.154 J/gK at 180 °C. The values obtained for all composites are almost the same and also very close to the values obtained for the sample without the fibers. The room-temperature C_p values of both $CaCO_3$ and glass fibers are quite similar, 0.8343 J/gK [132] and 0.810 J/gK [133], respectively, which explains very similar C_p values of the composites notwithstanding the EGF content.

Table 5.5: Specific heat capacity of BMC composites with different EGF weight fractions.

	c_p [J/gK]							
	EGF (wt%)							
	0	5	10	15	20	25	30	35
20 °C	0.899	0.903	0.903	0.900	0.893	0.899	0.883	0.907
100 °C	1.027	1.039	1.038	1.044	1.033	1.047	1.018	1.064
180 °C	1.154	1.175	1.174	1.189	1.174	1.195	1.152	1.222

5.3.3 Thermal conductivity

Thermal conductivity, λ, of BMC composites depending on the weight fraction of EGFs is shown in Figure 5.21. We note that the values obtained for a selected formulation within an individual series of samples were not reproduced in other two series, as it is clearly shown in the graph. Nevertheless, all three series show a similar trend of decreasing the thermal conductivity with increasing EGF content. We tentatively ascribe the observed differences to the fluctuations in the industrial-scale processing of BMC compounds.

The thermal conductivity of the composite without EGFs (0 wt%) is 0.960(6) W/mK and as the fiber content increases to 35 wt% it decreases to 0.771(04) W/mK. The high value of λ of the 0 wt%-composite is due to the high thermal conductivity of $CaCO_3$ mineral filler (~4.6–5.6 W/mK) which is about five times higher than λ of EGFs and an order of magnitude higher than of the polymer matrix, see Table 5.6. Note that in our case, the total weight fraction of inorganic phase is 79 %, and while the fraction of $CaCO_3$ mineral filler is increasing, the fraction of glass fibers is decreasing, see Figure 4.1.

In comparison to the polymer matrix the thermal conductivity of $CaCO_3$ mineral filler is high, however, its contribution to the thermal conductivity of the composite is quite moderate. As explained by Burger et al. [75] the incorporation of highly thermally conductive second phase inclusions into the PM usually does not reach its intrinsic thermal conductivity due to the insulating character of the polymer.

Furthermore, the heat transport in composites strongly depends on the connectivity between the second phase inclusions as demonstrated by Weidenfeller et al. [81] and Zhang et al. [82]. If the thermal conductivity of the inclusions is higher than that of the matrix, and if they form a connected network, i.e., if their concentration is above the percolation threshold, the thermal conductivity of the composite will increase with respect to the matrix itself.

In our case, we expect that in the 0 wt%-sample with 79 wt% of the $CaCO_3$ mineral filler particles the latter form an interconnected network. In the composites with glass fibers, the fraction of the mineral filler particles is decreasing with increasing fiber content. The fibers reduce the contacts between the $CaCO_3$ particles and thus hinder the effective

heat transport between them. As the thermal conductivity of EGFs is much lower than that of the $CaCO_3$ filler, the thermal conductivity of the composites decreases with increasing EGF content. Similar findings were reported by Li et al. [134] who studied polyamide-matrix composites that contained a constant weight fraction of alumina, magnesium hydroxide and graphite fillers (45 wt%) and varying glass fiber contents from 0 wt% to 5 wt%. The authors observed a slight decrease of the thermal conductivity of the composites with increasing fiber content from 1.95 W/mK to 1.88 W/mK for the composites with 0 wt% and 5 wt% of glass fibers, respectively, which they explained by the formation of the thermally-resistive network of the glass fibers.

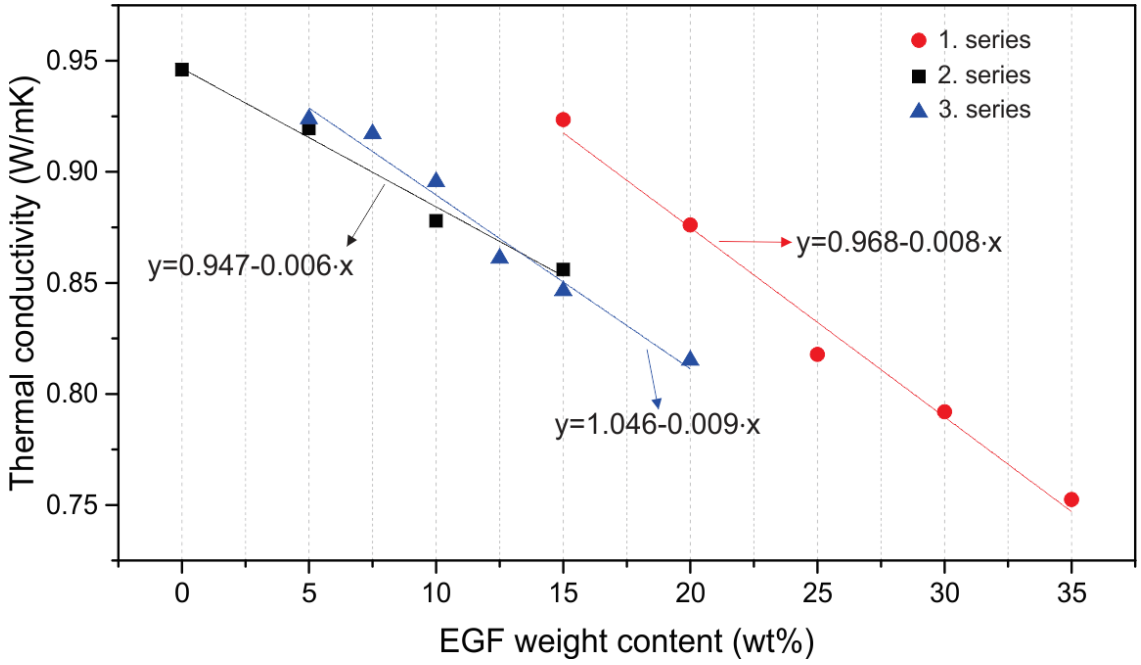


Figure 5.21: Thermal conductivity of BMC composites as a function of the EGF content. The results are presented for individual series of the samples. In all three series the thermal conductivity shows a decrease with increasing EGF content with similar slopes of the fitted lines.

Table 5.6: Thermal conductivity of individual phases in the composite, i.e. polymer, E-glass fibers and $CaCO_3$ mineral filler as reported in the literature.

	PM	EGF	$CaCO_3$
λ (W/mK)	0.12 – 0.50 [22]; 0.3 [135]	1.04 [14]; 1 [136]; 1.1 [134]; 1.3 [137]	5.6 [14]; 4.6 – 5.5 [138]

5.3.4 Summary

The thermal decompositions of all BMC composites are similar. The TG/DTA analysis revealed that the composites are thermally stable up to ~200 °C. The decomposition of the polymer matrix takes place in the temperature range from 200 °C to ~570 °C, with the total weight loss of about 21 %. The latter corresponds well to the initial weight content of the polymer resin, confirming a complete decomposition of the organic phase.

The specific heat capacity of the composites is almost independent of the glass fiber content as a consequence of very similar specific heat capacities of individual constituents.

The thermal conductivity of BMC composites decreases with increasing glass fiber content, and spans from 0.960 W/mK to 0.771 W/mK for the composites containing 0 wt% and 35 wt% of fibers, respectively. The contribution of the $CaCO_3$ mineral filler, which has almost an order of magnitude higher thermal conductivity than the polymer matrix, to the thermal conductivity of the composite is moderate and related to the thermally insulating character of the polymer matrix. In the composites with glass fibers, the fraction of the mineral filler particles is decreasing with increasing fiber content. As the thermal conductivity of the fibers is much lower than that of the $CaCO_3$ filler, the thermal conductivity of the composites decreases with increasing EGF content.

Chapter 6

Summary and Conclusions

In the thesis we address and discuss the relation between the microstructure, mechanical and thermal properties of bulk molding compound (BMC) composites with different weight fractions of E-glass fibers (EGFs), i.e. from 0 wt% to 35 wt%. In the first part of the Thesis, the microstructure of BMC composites with fiber contents from 5 wt% to 20 wt% is quantitatively described. We applied the image analysis techniques, tessellation-based methods and statistical methods to derive quantitative microstructural descriptors that were used to disclose the differences between microstructural patterns in order to determine the level of microstructural uniformity. We compared the experimental microstructures with the modelled uniform microstructural patterns.

The microstructural analysis of BMC composites with EGF contents from 5 wt% to 20 wt% showed that the highest level of microstructural uniformity was obtained in the sample with 7.5 wt% of EGFs and it decreased either with lower or progressively higher glass fiber content, see Figure 6.1.

The difference between experimental and modelled Voronoi polygon area size distributions of the studied samples and respective radial distribution functions (RDF) became more pronounced at higher fiber content, especially above 15 wt%. The distribution of experimental Voronoi polygons broadened and the peak shifted to smaller polygon areas, as characteristic features of fiber clustering. The calculated homogeneity parameter values (HP_A) increased with increasing fiber content and were from 0.71 to 1.13 for the composites with 5 wt% and 20 wt% of EGFs, respectively.

The best coincidence of the experimental and modelled Voronoi area size distributions and RDF was found in the composite with 7.5 wt% of EGFs. The latter composite had the lowest HP_A value (0.68) and the smallest extent of local disorder (~40 µm), as shown in Figure 6.1.

Slightly higher HP_A values, fluctuations over the RDF distance range and a higher extent of microstructural disorder (at ~80 µm) in the composite with 5 wt% of EGFs were attributed to the presence of large matrix areas surrounding isolated groups of fibers, thus contributing to a more non-uniform microstructure.

The RDF confirmed pronounced fiber clustering and increased microstructural non-uniformity with fiber content exceeding 7.5 wt%. The peak at the distance of the closest fiber approach (~11 µm) shifted to higher values and the range of local microstructural disorder became progressively extended; the distance, where the experimental RDF reached the modelled value was found to be the largest in the composite with 20 wt% of EGFs, around 130 µm.

The elongation parameter (EP) of the composite with 5 wt% of EGF was 1.18, confirming that the fibers were predominantly oriented parallel with the filling flow of the molding compound during manufacturing. At fiber contents exceeding 12.5 wt%, the

majority of fibers was still oriented parallel to the filling flow as apparent from the EP distributions. The EP increased to around 1.42 for the composite with 20 wt% of fibers indicating a higher level of fiber misalignment.

The microstructures of the composites with higher fiber contents, i.e. 25 wt% – 35 wt%, were highly disordered. Faults, such as poor fiber wetting, porosity and fiber damage were observed in micrographs, indicating that respective compound formulations were not appropriate for the selected manufacturing technology.

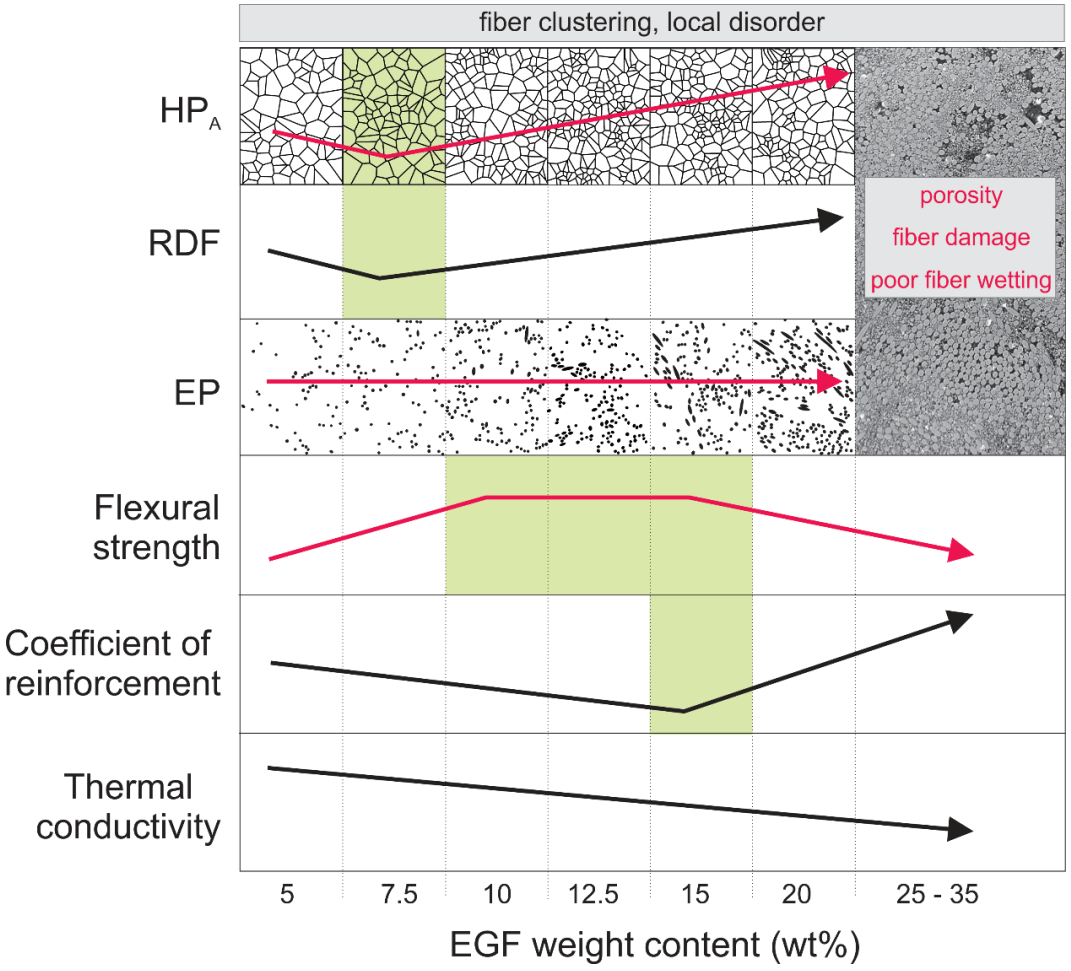


Figure 6.1: Relation between the microstructural descriptors and physical properties of BMC composites as a function of the EGF content.

In the second part of the thesis the mechanical and thermal properties of composites with different weight fractions of EGFs were studied. The flexural strength of BMC composites increased with increasing EGF content, reaching the peak values between 110 $\pm$ 8 MPa and 121 $\pm$ 16 MPa for the EGF fractions between 10 wt% and 15 wt%, respectively (see Figure 6.1). The maximum flexural strength (121 MPa) of the composite with 15 wt% of fibers is a consequence of the combined effect of a large enough fiber weight content and still high enough microstructural uniformity. As the fiber content increased above 20 wt%, the flexural strength of the composites decreased, which is related to the increased microstructural non-uniformity and defects in the materials structure, i.e. porosity, fiber damage and poor fiber wetting with the matrix.

Similarly, the viscoelastic properties of the BMC composites were influenced by the fiber fraction and distribution. The storage moduli of the composites increased with

increasing fiber content implying that the fibers provide stiffness. The coefficient of reinforcement, C, calculated from the respective moduli in the glassy and rubbery states, was the lowest (0.79) in the composite with 15 wt% of EGFs, meaning that in this composite the fiber reinforcing effect is the highest (see Figure 6.1). Even higher fiber content led to increased fiber friction which resulted in higher losses of mechanical energy, especially at 30 wt% and 35 wt% of EFG content. The glass transition temperature of the polymer matrix phase was not influenced by the EGF content.

Thermal conductivity of BMC composites decreased with increasing EGF weight content from 0.960 W/mK to 0.771 W/mK for the composite containing 0 wt% and 35 wt% of fibers, respectively (see Figure 6.1). The decrease of the thermal conductivity with increasing EGF content is explained by the formation of a thermally resistive network of EGFs and simultaneously decreasing content of $CaCO_3$ filler particles. Note that the latter have a much higher thermal conductivity than EGFs, however their contribution to the enhancement of the thermal conductivity is limited by the thermally insulating nature of the polymer matrix phase.

In summary, as shown in Figure 6.1, the highest degree of microstructural uniformity is attained in the composite with 7.5 wt% of EGFs, while the mechanical properties reach the optimal level in the EGF content range from 10 wt% to 15 wt%. Therefore, the overall optimum fiber content in the BMC composites is found to be a compromise between the high level of microstructural uniformity and suitable mechanical performance. Furthermore, present results demonstrate that the quantitative microstructural analysis may be a reliable source of supporting information in the product design and in the manufacturing process of real BMC parts from the serial production.

Appendix A

A.1 Definition of Voronoi Diagram

S denotes a set of n points in the plane. For two distinct elements in the plane $S \in p,\ q$, the dominance of p over q is defined as the subset of the plane being at least as close to p as to q, for δ denoting the Euclidean distance function:

$$D(p,\ q) = \{x \in R^2 \,|\, \delta(x,\ p) \leq \delta(x,\ q)\}. \tag{A.1}$$

$D(p,\ q)$ is a closed half plane bounded by the perpendicular bisector of p and q. This bisector separates all points of the plane closer to p from those closer to q.

The region of a site $p \in S$ is the portion of the plane lying in all of the dominances of p over the remaining sites in S.

$$VR(p, S) = \bigcap_{q \in S\{p\}} D(p, q) \tag{A.2}$$

Since the regions are coming from intersecting $n-1$ half-planes, they are convex polygons. Thus, the boundary of a region consists of at most $n-1$ edges and vertices. Each point on an edge is equidistant from exactly two sites and each vertex is equidistant from at least three. As a consequence, the regions are edge-to-edge and vertex-to-vertex, they form a polygonal partition of the plane. This partition is called the Voronoi diagram $V(S)$ of the finite point set S.

References

[1] C. Gorse, D. Johnston, and M. Pritchard, *A dictionary of Construction , Surveying and Civil Engineering*. Oxford: Oxford University Press, 2012.

[2] A. B. Strong, *Fundamentals of composites manufacturing : materials, methods and applications*, 2nd ed. Dearborn: Society of Manufacturing Engineers, 2008.

[3] K. L. Edwards, "An overview of the technology of fibre-reinforced plastics for design purposes," *Mater. Des.*, vol. 19, no. 1–2, pp. 1–10, 1998.

[4] S. K. Mazumdar, *Composites manufacturing : materials, product, and process engineering*. Boca Raton: CRC Press, 2002.

[5] S. J. Pickering, "Recycling technologies for thermoset composite materials—current status," *Compos. Part A*, vol. 37, no. 8, pp. 1206–1215, 2006.

[6] K. Jacques, L. Bax, H. Vasiliadis, I. Magallon, and K. Ong, "Polymer composites for automotive sustainability." SusChem, p. 56, 2015.

[7] K. K. Chawla, *Composite Materials: Science and Engineering*, 3rd ed. New York; London: Springer, 2012.

[8] E. Witten, M. Thomas, and K. Michael, "Composites Market Report 2015," 2015.

[9] R. Derosa, "Current State of Recycling Sheet Molding Compounds and Related Materials," *J. Thermoplast. Compos. Mater.*, vol. 18, no. May 2005, pp. 219–240, 2005.

[10] P. K. Mallick, "Polyester," in *Fiber reinforced composites: materials, manufaturing and design*, 3rd ed., Boca Raton ; London ; New York: CRC Press, 2008, pp. 76–81.

[11] C. A. Harper and E. M. Petrie, "Introduction," in *Plastic Materials and Processes: A concise Encyclopedia*, Hoboken, New Jersey: John Wiley & Sons, Inc., 2003, p. xii.

[12] "E-Glass Fibre." [Online]. Available: http://www.azom.com/properties.aspx?ArticleID=764. [Accessed: 26-Apr-2016].

[13] P. Jakubowska and T. Sterzyñski, "Thermal diffusivity of polyolefin composites highly filled with calcium carbonate," *Polimery/Polymers*, vol. 57, no. 4, pp. 271–275, 2012.

[14] P. K. Mallick, "Particulate and Short Fiber Reinforced Polymer Composites," in *Comprehensive Composite Materials*, A. Kelly, Ed. Amsterdam; New York: Elsevier Science Ltd., 2000, pp. 291–331.

[15] Z. Zhang and S. Zhu, "Microvoids in unsaturated polyester resins containing poly(vinyl acetate) and composites with calcium carbonate and glass fibers," *Polymer (Guildf).*, vol. 41, no. 10, pp. 3861–3870, 2000.

[16] R. Burns, *Polyester molding compounds*. New York ; Basel: M. Dekker, 1982.

[17] Injection Molding Online, "Injection Molding," 2007. [Online]. Available: http://www.injectionmoldingonline.com/Molding101/InjectionMolding.aspx. [Accessed: 05-Jul-2016].

[18] West Coast Gasket Company, "What is transfer molding?," 2007. [Online]. Available: http://www.westcoastgasket.com/transfer-molding.html. [Accessed: 05-Jul-2016].

[19] A. Bernasconi, F. Cosmi, and D. Dreossi, "Local anisotropy analysis of injection moulded fibre reinforced polymer composites," *Compos. Sci. Technol.*, vol. 68, no. 12, pp. 2574–2581, 2008.

[20] D. Teixeira, M. Giovanela, L. B. Gonella, and J. S. Crespo, "Influence of injection molding on the flexural strength and surface quality of long glass fiber-reinforced polyamide 6.6 composites," *Mater. Des.*, vol. 85, pp. 695–706, 2015.

[21] A. Bernasconi, P. Davoli, A. Basile, and A. Filippi, "Effect of fibre orientation on the fatigue behaviour of a short glass fibre reinforced polyamide-6," *Int. J. Fatigue*, vol. 29, no. 2, pp. 199–208, 2007.

[22] W. Callister and D. Rethwisch, "Composites," in *Materials Science and Engineering*, 7th ed., New York: John Wiley & Sons, Inc., 2007, pp. 577–620.

[23] A. N. Oumer and O. Mamat, "A review of effects of molding methods, mold thickness and other processing parameters on fiber orientation in polymer composites," *Asian J. Sci. Res.*, vol. 6, no. 3, pp. 401–410, 2013.

[24] E. Lafranche, P. Krawczak, J. P. Ciolczyk, and J. Maugey, "Injection moulding of long glass fibre reinforced polyamide 6-6: Guidelines to improve flexural properties," *Express Polym. Lett.*, vol. 1, no. 7, pp. 456–466, 2007.

[25] X. Sun, J. Lasecki, D. Zeng, Y. Gan, X. Su, and J. Tao, "Measurement and quantitative analysis of fiber orientation distribution in long fiber reinforced part by injection molding," *Polym. Test.*, vol. 42, pp. 168–174, 2015.

[26] C. A. Silva, J. C. Viana, F. W. J. van Hattum, and A. M. Cunha, "Fiber orientation in divergent/convergent flows in expansion and compression injection molding," *Polym. Compos.*, vol. 27, no. 5, pp. 539–551, 2006.

[27] K. Takahashi and N. S. Choi, "Influence of fibre weight fraction on failure mechanisms of poly(ethylene terephthalate) reinforced by short-glass-fibres," *J. Mater. Sci.*, vol. 26, no. 17, pp. 4648–4656, 1991.

[28] R. Blanc, C. Germain, J. P. Da Costa, P. Baylou, and M. Cataldi, "Fiber orientation measurements in composite materials," *Compos. Part A Appl. Sci. Manuf.*, vol. 37, no. 2, pp. 197–206, 2006.

[29] T. B. Nguyen Thi, M. Morioka, A. Yokoyama, S. Hamanaka, K. Yamashita, and C. Nonomura, "Measurement of fiber orientation distribution in injection-molded short-glass-fiber composites using X-ray computed tomography," *J. Mater. Process. Technol.*, vol. 219, pp. 1–9, 2015.

[30] A. Bernasconi, F. Cosmi, and P. J. Hine, "Analysis of fibre orientation distribution in short fibre reinforced polymers: A comparison between optical and tomographic methods," *Compos. Sci. Technol.*, vol. 72, no. 16, pp. 2002–2008, 2012.

[31] F. J. Guild and J. Summerscales, "Microstructural image analysis applied to fibre composite materials: a review," *Composites*, vol. 24, no. 5, pp. 383–393, 1993.

[32] L. Averous, J. C. Quantin, D. Lafon, and A. Crespy, "Morphological determinations of fiber composites," *Microsc. Microanal. Microstruct.*, vol. 7, no. 5–6, pp. 433–439, 1996.

[33] J. Zangenberg, J. Larsen, R. C. Østergaard, and P. Brøndsted, "Methodology for characterisation of glass fibre composite architecture," *Plast. Rubber Compos.*, vol. 41, no. 4, pp. 187–193, 2012.

[34] S. Toll and P.-O. Andersson, "Microstructural characterization of injection moulded composites using image analysis," *Composites*, vol. 22, no. 4, pp. 298–306, 1991.

[35] F. Aurenhammer, "Voronoi Diagrams — A Survey of a Fundamental Data Structure," *ACM Comput. Surv.*, vol. 23, no. 3, pp. 345–405, 1991.

[36] M. G. Voronoi, "Recherches sur les parallélloèdres primitifs," *J. für die reine und Angew. Math.*, vol. 134, pp. 198–287, 1908.

[37] M. G. Voronoi, "Nouvelles applications des paramètres continus à la théorie des formes quadratiques. Deuxième mémoire. Recherches sur les parallélloèdres primitifs. Second partie.," *J. für die Reine Angew. Math.*, vol. 136, pp. 67–182, 1909.

[38] A. Okabe, T. Satoh, T. Furuta, A. Suzuki, and K. Okano, "Generalized network Voronoi diagrams: Concepts, computational methods, and applications," *Int. J. Geogr. Inf. Sci.*, vol. 22, no. 9, pp. 965–994, 2008.

[39] S. Fonseca, J. Milho, B. Travassos, and D. Araújo, "Spatial dynamics of team sports exposed by Voronoi diagrams," *Hum. Mov. Sci.*, vol. 31, no. 6, pp. 1652–1659, 2012.

[40] B. She, X. Zhu, X. Ye, W. Guo, K. Su, and J. Lee, "Weighted network Voronoi Diagrams for local spatial analysis," *Comput. Environ. Urban Syst.*, vol. 52, pp. 70–80, 2015.

[41] K. R. Mackie and C. D. Cooper, "Landfill gas emission prediction using Voronoi diagrams and importance sampling," *Environ. Model. Softw.*, vol. 24, no. 10, pp. 1223–1232, Oct. 2009.

[42] M. J. G. W. Heijman, N. E. Benes, J. E. Ten Elshof, and H. Verweij, "Quantitative analysis of the microstructural homogeneity of zirconia-toughened alumina composites," *Mater. Res. Bull.*, vol. 37, no. 1, pp. 141–149, 2002.

[43] G. Trefalt, A. Benčan, M. Kamplet, B. Malič, Y. Seo, and K. G. Webber, "Evaluation of the homogeneity in $Pb(Zr,Ti)O_3$-zirconia composites prepared by the hetero-agglomeration of precursors using the Voronoi-diagram approach," *J. Eur. Ceram. Soc.*, vol. 34, no. 3, pp. 669–675, 2014.

[44] J. Summerscales, F. J. Guild, N. R. L. Pearce, and P. M. Russell, "Voronoi cells, fractal dimensions and fibre composites," *J. Microsc.*, vol. 201, no. 2, pp. 153–162, 2001.

[45] Z. Samardžija, U. Kunaver, M. Čeh, and S. Novak, "Determination of ZrO_2 Distribution in an Al_2O_3 Matrix by Digital Image Analysis and Point-Pattern Analysis," *Scanning*, vol. 17, pp. 186–191, 1995.

[46] S. Ghosh, Z. Nowak, and K. Lee, "Quantitative Characterization and Modeling of Composite Microstructures By Voronoi Cells," *Acta Mater.*, vol. 45, no. 6, pp. 2215-2234, 1997.

[47] Z. Sun, X. Zhao, and J. Ma, "Characterization of microstructures in sisal fiber composites by Voronoi diagram," *J. Reinf. Plast. Compos.*, vol. 32, no. 1,

pp. 16-22, 2012.

[48] R. Pyrz, "The application of morphological methods to composite materials," in *Polymer matrix composites*, R. Talreja and J. Manson, Eds. Amsterdam: Elsevier, 2001, pp. 553–576.

[49] G. Trefalt, "A New Synthesis Route to $Pb(Mg_{1/3}Nb_{2/3})O_3$-Based Materials by the Controlled Agglomeration of Reagent Particles," Jožef Stefan International Postgraduate School, 2012.

[50] J. M. Ziman, "Amorphous or paracrystalline?," in *Models od disorder: The theoretical Physics of Homogeneously Disordered Systems*, Cambridge; New York: Cambridge University Press, 1979, p. 69.

[51] R. K. Everett, "Quantification od random fiber arrangements using a radial distribution function approach," *J. Compos. Mater.*, vol. 30, no. 6, pp. 748–758, 1996.

[52] R. Pyrz, "Correlation of microstructure variability and local stress field in two-phase materials," *Mater. Sci. Eng. A*, vol. 177, no. 1–2, pp. 253–259, 1994.

[53] S. Singh, P. Kumar, and S. K. Jain, "An experimental and numerical investigation of mechanical properties of glass fiber reinforced epoxy composites," *Adv. Mater. Lett.*, vol. 4, no. 7, pp. 567–572, 2013.

[54] S. Joseph, M. S. Sreekala, Z. Oomen, P. Koshy, and S. Thomas, "A comparison of the mechanical properties of phenol formaldehyde composites reinforced with banana fibre and glass fibres," *Compos. Sci. Technol.*, vol. 62, pp. 1857–1868, 2002.

[55] S.-Y. Fu, B. Lauke, E. Mäder, C.-Y. Yue, and X. Hu, "Tensile properties of short-glass-fiber-and short-carbon-fiber-reinforced polypropylene composites," *Compos. Part A Appl. Sci. Manuf.*, vol. 31, no. 10, pp. 1117–1125, 2000.

[56] A. A. Abdulmajeed, T. O. Närhi, P. K. Vallittu, and L. V. Lassila, "The effect of high fiber fraction on some mechanical properties of unidirectional glass fiber-reinforced composite," *Dent. Mater.*, vol. 27, no. 4, pp. 313–321, 2011.

[57] G. Agarwal, A. Patnaik, and R. K. Sharma, "Mechanical and Thermo–Mechanical Properties of Bi-Directional and Short Carbon Fiber Reinforced Epoxy Composites," *J. Eng. Sci. Technol.*, vol. 9, no. 5, pp. 590–604, 2014.

[58] J. L. Thomason, "The influence of fibre length and concentration on the properties of glass fibre reinforced polypropylene. 6. The properties of injection moulded long fibre PP at high fibre content," *Compos. Part A Appl. Sci. Manuf.*, vol. 36, no. 7, pp. 995–1003, 2005.

[59] Siddhartha and K. Gupta, "Mechanical and abrasive wear characterization of bidirectional and chopped E-glass fiber reinforced composite materials," *Mater. Des.*, vol. 35, pp. 467–479, 2012.

[60] J. L. Thomason, "The influence of fibre length and concentration on the properties of glass fibre reinforced polypropylene: 5. Injection moulded long and short fibre PP," *Compos. Part A Appl. Sci. Manuf.*, vol. 33, no. 12, pp. 1641–1652, 2002.

[61] P. Amuthakkannan, V. Manikandan, J. T. W. Jappes, and M. Uthayakumar, "Effect of Fibre Length and Fibre Content on Mechanical Properties of Short Basalt Fibre," *Mater. Phys. Mech.*, vol. 16, pp. 107–117, 2013.

[62] V. S. Sreenivasan, D. Ravindran, V. Manikandan, and R. Narayanasamy,

"Mechanical properties of randomly oriented short Sansevieria cylindrica fibre/polyester composites," *Mater. Des.*, vol. 32, no. 4, pp. 2444–2455, 2011.

[63] L. J. Mishnaevsky, K. Derrien, and D. Baptiste, "Effect of microstructure of particle reinforced composites on the damage evolution : probabilistic and numerical analysis," *Compos. Sci. Technol.*, vol. 64, pp. 1805–1818, 2004.

[64] N. Saba, M. Jawaid, O. Y. Alothman, and M. T. Paridah, "A review on dynamic mechanical properties of natural fibre reinforced polymer composites," *Constr. Build. Mater.*, vol. 106, pp. 149–159, 2016.

[65] Z. Budai, Z. Sulyok, and V. Vargha, "Glass-fibre reinforced composite materials based on unsaturated polyester resins," *J. Therm. Anal. Calorim.*, vol. 109, no. 3, pp. 1533–1544, 2012.

[66] M. Idicula, S. K. Malhotra, K. Joseph, and S. Thomas, "Dynamic mechanical analysis of randomly oriented intimately mixed short banana/sisal hybrid fibre reinforced polyester composites," *Compos. Sci. Technol.*, vol. 65, no. 7–8, pp. 1077–1087, 2005.

[67] D. Romanzini, A. Lavoratti, H. L. Ornaghi, S. C. Amico, and A. J. Zattera, "Influence of fiber content on the mechanical and dynamic mechanical properties of glass/ramie polymer composites," *Mater. Des.*, vol. 47, pp. 9–15, 2013.

[68] L. Uma Devi, S. S. Bhagawan, and S. Thomas, "Dynamic mechanical analysis of pineapple leaf/glass hybrid fiber reinforced polyester composites," *Polym. Compos.*, vol. 31, no. 6, pp. 956–965, 2010.

[69] J. H. S. Almeida Junior, H. L. Ornaghi Junior, S. C. Amico, and F. D. R. Amado, "Study of hybrid intralaminate curaua/glass composites," *Mater. Des.*, vol. 42, pp. 111–117, 2012.

[70] S. Houshyar, R. A. Shanks, and A. Hodzic, "The effect of fiber concentration on mechanical and thermal properties of fiber-reinforced polypropylene composites," *J. Appl. Polym. Sci.*, vol. 96, no. 6, pp. 2260–2272, 2005.

[71] V. S. Sreenivasan, N. Rajini, A. Alavudeen, and V. Arumugaprabu, "Dynamic mechanical and thermo-gravimetric analysis of Sansevieria cylindrica/polyester composite: Effect of fiber length, fiber loading and chemical treatment," *Compos. Part B Eng.*, vol. 69, pp. 76–86, 2015.

[72] R. Arambakam, H. Vahedi Tafreshi, and B. Pourdeyhimi, "A simple simulation method for designing fibrous insulation materials," *Mater. Des.*, vol. 44, pp. 99–106, 2013.

[73] I. a. Tsekmes, R. Kochetov, P. H. F. Morshuis, and J. J. Smit, "Thermal conductivity of polymeric composites: A review," *2013 IEEE Int. Conf. Solid Dielectr.*, no. December 2015, pp. 678–681, 2013.

[74] G. Kalaprasad, P. Pradeep, G. Mathew, C. Pavithran, and S. Thomas, "Thermal conductivity and thermal diffusivity analyses of low-density polyethylene composites reinforced with sisal , glass and intimately mixed sisal/glass fibres," *Compos. Sci. Technol.*, vol. 60, pp. 2967–2977, 2000.

[75] N. Burger, A. Laachachi, M. Ferriol, M. Lutz, V. Toniazzo, and D. Ruch, "Review of thermal conductivity in composites: mechanisms, parameters and theory," *Prog. Polym. Sci.*, pp. 1–28, 2016.

[76] S. Han and D. D. L. Chung, "Increasing the through-thickness thermal conductivity of carbon fiber polymer-matrix composite by curing pressure increase and filler incorporation," *Compos. Sci. Technol.*, vol. 71, no. 16, pp. 1944–1952, 2011.

[77] B. Rudin and D. Drummer, "Heat conductive thermosets for the injection molding process," *2012 2nd Int. Electr. Drives Prod. Conf. EDPC 2012 - Proc.*, pp. 1–4, 2012.

[78] Y.-H. Yu, C.-C. M. Ma, C.-C. Teng, Y.-L. Huang, H.-W. Tien, S.-H. Lee, and I. Wang, "Enhanced thermal and mechanical properties of epoxy composites filled with silver nanowires and nanoparticles," *J. Taiwan Inst. Chem. Eng.*, vol. 44, no. 4, pp. 654–659, 2013.

[79] J. P. Hong, S. W. Yoon, T. Hwang, J. S. Oh, S. C. Hong, Y. Lee, and J. Do Nam, "High thermal conductivity epoxy composites with bimodal distribution of aluminum nitride and boron nitride fillers," *Thermochim. Acta*, vol. 537, pp. 70–75, 2012.

[80] S. Li, S. Qi, N. Liu, and P. Cao, "Study on thermal conductive BN/novolac resin composites," *Thermochim. Acta*, vol. 523, no. 1–2, pp. 111–115, 2011.

[81] B. Weidenfeller, M. Höfer, and F. R. Schilling, "Thermal conductivity, thermal diffusivity, and specific heat capacity of particle filled polypropylene," *Compos. Part A Appl. Sci. Manuf.*, vol. 35, no. 4, pp. 423–429, 2004.

[82] S. Zhang, X. Y. Cao, Y. M. Ma, Y. C. Ke, J. K. Zhang, and F. S. Wang, "The effects of particle size and content on the thermal conductivity and mechanical properties of Al_2O_3/high density polyethylene (HDPE) composites," *Express Polym. Lett.*, vol. 5, no. 7, pp. 581–590, 2011.

[83] C. L. Beyler and M. M. Hirschler, "Thermal Decomposition of Polymers," *SPE Handb. Fire Prot. Eng.*, pp. 110–131, 2001.

[84] Y. Bai, T. Keller, and T. Vallée, "Modeling of stiffness of FRP composites under elevated and high temperatures," *Compos. Sci. Technol.*, vol. 68, no. 15–16, pp. 3099–3106, 2008.

[85] A. P. Mouritz, Z. Mathys, and A. G. Gibson, "Heat release of polymer composites in fire," *Compos. Part A Appl. Sci. Manuf.*, vol. 37, no. 7, pp. 1040–1054, 2006.

[86] K. Laoubi, Z. Hamadi, A. Ahmed Benyahia, A. Serier, and Z. Azari, "Thermal behavior of E-glass fiber-reinforced unsaturated polyester composites," *Compos. Part B Eng.*, vol. 56, pp. 520–526, 2014.

[87] E. Kandare, B. K. Kandola, D. Price, S. Nazaré, and R. A. Horrocks, "Study of the thermal decomposition of flame-retarded unsaturated polyester resins by thermogravimetric analysis and Py-GC/MS," *Polym. Degrad. Stab.*, vol. 93, no. 11, pp. 1996–2006, 2008.

[88] J. Rueff, J. P. Teixeira, L. S. Santos, and J. F. Gaspar, "Genetic effects and biotoxicity monitoring of occupational styrene exposure," *Clin. Chim. Acta*, vol. 399, no. 1–2, pp. 8–23, 2009.

[89] IARC Working Group on the evaluation of carcinogenic risks to humans, "Styrene," in *IARC Monographs on the Evaluation of Carcinogenic Risks to Humans: Some Industrial Chemicals*, vol. 60, Lyon: International Agency for Research on Cancer, 1994, p. 389.

[90] Cefic, "Occupational exposure to styrene," *Technical Bulletin*. [Online]. Available: http://www.plasticseurope.org/Documents/Document/20100308102027-CEFICpdf3Occupationalexposuretostyreneversion3-20050407-014-EN-v1.pdf. [Accessed: 11-Dec-2016].

[91] G. Rajhans and B. Pathak, "Standards and guidelines," in *Practical guide to respirator usage in industry*, 2., Woburn: Elsevier Science, 2002, p. 165.

[92] "Uradni List Republike Slovenija št.100," no. 63. Republika Slovenija, Ministrstvo za delo, družino in socialne zadeve, pp. 3873–3928, 2011.

[93] IARC Working Group on the Evaluation of Carcinogenic Risks to Humans, "Styrene," in *IARC Monographs on the Evaluation of Carcinogenic Risks to Humans: Some Traditional Herbal Medicines, Some Mycotoxins, Naphthalene, and Styrene*, vol. 82, Lyon: International Agency for Research on Cancer, 2002, p. 590.

[94] J. C. Wakefield, "Styrene-Toxicological overview." HPA Centre for Radiation, Chemical and Environmental Hazards, pp. 1–10, 2007.

[95] OSHA, "Styrene-OSHA Method ORG-09," 1980. [Online]. Available: https://www.osha.gov/dts/sltc/methods/organic/org009/org009.html. [Accessed: 12-Dec-2016].

[96] T. Salthammer and E. Uhde, Eds., *Organic Indoor Air Pollutants: Occurence, Measurement, Evaluation*, 2nd ed. Weinheim: Wiley-VCH, 2009.

[97] G. Marsh, "Europe gets tough on end-of-life composites," *Reinf. Plast.*, no. September, pp. 34–39, 2003.

[98] "Directive 2000/53/EC on end-of life vehicles." pp. 1–22, 2013.

[99] J. R. Correia, N. M. Almeida, and J. R. Figueira, "Recycling of FRP composites: Reusing fine GFRP waste in concrete mixtures," *J. Clean. Prod.*, vol. 19, no. 15, pp. 1745–1753, 2011.

[100] "Directive 2002/96/EC on waste electrical and electronic equipement." pp. 24–39, 2003.

[101] "Directive 2008/98/EC on waste and repealing certain Directives." pp. 3–30, 2008.

[102] C. Fischer, M. Lehner, and D. McKinnon, "Overview of the use of landfill taxes in Europe," 2012.

[103] J. Rybicka, A. Tiwari, P. Alvarez Del Campo, and J. Howarth, "Capturing composites manufacturing waste flows through process mapping," *J. Clean. Prod.*, vol. 91, pp. 251–261, 2015.

[104] Y. Yang, R. Boom, B. Irion, D. J. van Heerden, P. Kuiper, and H. de Wit, "Recycling of composite materials," *Chem. Eng. Process. Process Intensif.*, vol. 51, pp. 53–68, 2012.

[105] P. Asokan, M. Osmani, and A. D. F. Price, "Assessing the recycling potential of glass fibre reinforced plastic waste in concrete and cement composites," *J. Clean. Prod.*, vol. 17, no. 9, pp. 821–829, 2009.

[106] G. Oliveux, J.-L. Bailleul, and E. L. G. La Salle, "Chemical recycling of glass fibre reinforced composites using subcritical water," *Compos. Part A Appl. Sci. Manuf.*, vol. 43, no. 11, pp. 1809–1818, 2012.

[107] S. Job, G. Leeke, P. T. Mativenga, G. Oliveux, S. Pickering, and N. A. Shuaib, "Composites recycling : Where are we now ?," 2016. [Online]. Available:

https://compositesuk.co.uk/system/files/documents/Recycling%20Report%202016.pdf. [Accessed: 12-Dec-2016].

[108] Fiberline Composites, "Breakthrough: Recycling of fibreglass is now a reality," 2010. [Online]. Available: https://fiberline.com/news/miljoe/breakthrough-recycling-fibreglass-now-reality. [Accessed: 14-Dec-2016].

[109] "ISO 3167: Plastics-Multipurpose test specimens," 2002.

[110] M. N. Rahaman, *Ceramics Processing*. Boca Raton: CRC Press, 2006.

[111] W. S. Rasband, "ImageJ." U.S. National Institutes of Health, Maryland, USA, 2014.

[112] "UTHSCSA ImageTool." University of Texas Health Science Center At San Antonio, Texas, 2002. Available: http://compdent.uthscsa.edu/dig/itdesc.html.

[113] "ISO 178: Plastics. Determination of flexural properties," 2003.

[114] Z. Zhang, P. Wang, and J. Wu, "Dynamic Mechanical Properties of EVA Polymer-Modified Cement Paste at Early Age," *Phys. Procedia*, vol. 25, pp. 305–310, 2012.

[115] "Measuring specific heat capacity," no. UC 71. Mettler Toledo, pp. 1–20, 1998.

[116] D. a. Ditmars, S. Ishihara, S. S. Chang, G. Bernstein, and E. D. West, "Enthalpy and Heat-Capacity Standard Reference Material: Synthetic Sapphire (Alpha-Al2O3) from 10 to 2250 K," *J. Res. Natl. Bur. Stand. (1934).*, vol. 87, no. 2, pp. 159–163, 1982.

[117] S. E. Gustafsson, "Transient plane source techniques for thermal conductivity and thermal diffusivity measurements of solid materials," *Rev. Sci. Instrum.*, vol. 62, no. 3, pp. 797–804, 1991.

[118] "PDF-ICDD." International Center for Diffraction Data, Newton Square, 2002.

[119] L. Von Entwässerungsanlagen, "Technische information TETRADUR L 4220-776." Tetradur, pp. 1–12, 2008.

[120] K. Gawdzinska, L. Wojnar, M. Malinski, and J. Chraponski, "Structure homogeneity as a parameter for evaluation of composite casting quality," *Arch. Foundry Eng.*, vol. 10, no. 3, pp. 187–192, 2010.

[121] M. G. H. M. Hendriks, M. J. G. W. Heijman, W. E. van Zyl, and J. E. ten Elshof, "Quantitative Analysis of Microstructural Homogeneity and Capacitance Correlations in Palladium/Yttria-Stabilized Zirconia Composites," *J. Am. Ceram. Soc.*, vol. 85, no. 8, pp. 2097–2101, 2002.

[122] H. Tanaka, T. Hayashi, and T. Nishi, "Digital image analysis of droplet patterns in polymer systems: Point pattern," *J. Appl. Phys.*, vol. 65, no. 12, pp. 4480–4495, 1989.

[123] W. A. Spitzig, J. F. Kelly, and O. Richmond, "Quantitative characterization of second-phase populations," *Metallography*, vol. 18, pp. 235–261, 1985.

[124] V. N. Bulsara, R. Talreja, and J. Qu, "Damage initiation under transverse loading of unidirectional composites with arbitrarily distributed fibers," *Compos. Sci. Technol.*, vol. 59, no. 5, pp. 673–682, 1999.

[125] S. D. Salman, Z. Leman, M. T. H. Sultan, M. R. Ishak, and F. Cardona, "Influence of Fiber Content on Mechanical and Morphological Properties of Woven Kenaf Reinforced PVB Film Produced Using a Hot Press Technique," *Int. J. Polym. Sci.*, vol. 2016, pp. 1–11, 2016.

[126] L. A. Pothan, Z. Oommen, and S. Thomas, "Dynamic mechanical analysis of banana

fiber reinforced polyester composites," *Compos. Sci. Technol.*, vol. 63, no. 2, pp. 283–293, 2003.

[127] A. P. Mouritz and A. G. Gibson, "Thermal Decomposition of Composites in Fire," in *Fire Properties of Polymer Composite Materials*, Dordrecht: Springer, 2006, pp. 19–58.

[128] L. B. Manfredi, E. S. Rodríguez, M. Wladyka-Przybylak, and A. Vázquez, "Thermal degradation and fire resistance of unsaturated polyester, modified acrylic resins and their composites with natural fibres," *Polym. Degrad. Stab.*, vol. 91, no. 2, pp. 255–261, 2006.

[129] S. J. Evans, P. J. Haines, and G. A. Skinner, "The thermal degradation of polyester resins II. The effects of cure and of fillers on degradation," *Thermochim. Acta*, vol. 291, no. 1–2, pp. 43–49, 1997.

[130] I. Halikia, L. Zoumpoulakis, E. Christodoulou, and D. Prattis, "Kinetic study of the thermal decomposition of calcium carbonate by isothermal methods of analysis," *Eur. J. Miner. Process. Environ. Prot.*, vol. 1, no. 2, pp. 89–102, 2001.

[131] X. Li, L. G. Tabil, I. N. Oguocha, and S. Panigrahi, "Thermal diffusivity, thermal conductivity, and specific heat of flax fiber-HDPE biocomposites at processing temperatures," *Compos. Sci. Technol.*, vol. 68, no. 7–8, pp. 1753–1758, 2008.

[132] Matweb, "Calcium Carbonate, Calcite (CaCO3)." [Online]. Available: http://www.matweb.com/search/datasheet_print.aspx?matguid=bea4bfa9c8bd462093d50da5eebe78ac. [Accessed: 03-Feb-2017].

[133] Matweb, "E-Glass Fiber, Generic." [Online]. Available: http://www.matweb.com/search/datasheet.aspx?matguid=d9c18047c49147a2a7c0b0bb1743e812&ckck=1. [Accessed: 03-Feb-2017].

[134] M. Li, Y. Wan, Z. Gao, G. Xiong, X. Wang, C. Wan, and H. Luo, "Preparation and properties of polyamide 6 thermal conductive composites reinforced with fibers," *Mater. Des.*, vol. 51, pp. 257–261, 2013.

[135] P. Eyerer, "Plastics: Classification, Characterization, and Economic Data," in *Polymers: opportunities and risks, Vol. 1, General and environmental aspects*, vol. 1, Berlin, London: Springer, 2010, p. 437.

[136] Saint Gobain Vetrotex, "E, R and D glass properties," 2002. [Online]. Available: http://glassproperties.com/glasses/E_R_and_D_glass_properties.pdf. [Accessed: 17-Nov-2016].

[137] A. Patnaik, P. Kumar, S. Biswas, and M. Kumar, "Investigations on micro-mechanical and thermal characteristics of glass fiber reinforced epoxy based binary composite structure using finite element method," *Comput. Mater. Sci.*, vol. 62, pp. 142–151, 2012.

[138] U. Almaz Optics, Inc., "CALCIUM CARBONATE (CALCITE), CaCO3." [Online]. Available: http://www.almazoptics.com/CaCO3.htm. [Accessed: 17-Nov-2016].

Bibliography

Publications Related to the Thesis

Journal Articles

B. Bertoncelj, K. Vojisavljević, J. Rihtaršič, G. Trefalt, M. Huskić, E. Žagar, B. Malič. "A Voronoi-diagram analysis of the microstructures in bulk-molding compounds and its correlation with the mechanical properties," Express Polymer Letters, vol. 10, no. 6, pp. 493-505, 2016.

B. Bertoncelj, K. Vojisavljević, M. Vrabelj, B. Malič. "Thermal properties of polymer-matrix composites reinforced with E-glass fibers = Toplotne lastnosti kompozitov na osnovi polimerov, ojačanih s steklenimi vlakni," *Informacije MIDEM*, vol. 45, no. 3, pp. 216-221, 2015.

Published scientific conference paper

B. Bertoncelj , K. Vojisavljević, J. Rihtaršič, G. Treflat, B. Malič." Microstructural analysis of Bulk Molding Compounds and correlation with the flexural strength," in *Proceedings of the 8th Jožef Stefan International Postgraduate School Student' Conference*, Ljubljana, Slovenia: Jožef Stefan International Postgraduate School, 2016.

B. Bertoncelj , K. Vojisavljević, J. Rihtaršič, G. Jelenc, B. Malič. "Microstructure, mechanical and electrical properties of Glass Fiber Reinforced Composites (GFRC)," in *Proceedings of the 7th Jožef Stefan International Postgraduate School Student' Conference*, Ljubljana, Slovenia: Jožef Stefan International Postgraduate School, 2015.

B. Bertoncelj , K. Vojisavljević, J. Rihtaršič, G. Jelenc, B. Malič. "Effect of e-glass fiber and mineral filler content on microstructure, mechanical, dielectric and thermal properties of bulk molding compound," in *Proceedings of the 50th International Conference on Microelectronics, Devices and Materials*, Ljubljana, Slovenia: MIDEM - Society for Microelectronics, Electronic Components and Materials, 2014.

B. Bertoncelj , K. Vojisavljević, J. Rihtaršič, G. Jelenc, B. Malič, M. Stušek, D. Belavič. "Characterization of glass fiber reinforced composites for housing of electrical motors," in *Proceedings of the 49th International Conference on Microelectronics, Devices and Materials & the Workshop on Digital Electronic Systems*, Kranjska Gora, Slovenia: MIDEM - Society for Microelectronics, Electronic Components and Materials, 2013.

Published scientific conference contribution – abstract

B. Bertoncelj, K. Vojisavljević, J. Rihtaršič, M. Huskić, E. Žagar, G. Trefalt, B. Malič. "Influence of E-glass fibre content on thermal properties of glass-fibre reinforced composites," in *Book of abstracts of the 3rd Central and Eastern European Conference on Thermal Analysis and Calorimetry*, Ljubljana, Slovenia: CEEC-TAC3 - Central and Eastern European Committee for Thermal Analysis and Calorimetry, 2015.

Other Publications

N. Kojadin, B. Bertoncelj, J. Rihtaršič, R. Žavbi. "Informacije za demontažo elektromotorjev po direktivi 2012/19/EU: odpadna električna in elektronska oprema – OEEO," Ljubljana: Faculty Of Mechanical Engineering, 2015.

N. Kojadin, B. Bertoncelj, J. Rihtaršič, R. Žavbi. "*Znižanje ogljičnega odtisa v odvisnosti od sprememb različnih parametrov elektromotorjev*," Ljubljana: Faculty Of Mechanical Engineering, 2014.

Biography

I was born on 5 August 1982 in Kranj. After finishing the Gymnasium in Škofja Loka I enrolled to the programme Graphic Technology at the Faculty of Natural Sciences and Engineering, University of Ljubljana. I graduated in June 2010 with the diploma thesis entitled *Durability of printed polyolefin plates, made with the addition of starch.* In October 2012 I started working in the company Domel and enrolled in the doctoral study programme Ecotechnology at the Jožef Stefan International Postgraduate School. My work mainly comprises the study of polymer-matrix reinforced composites, their microstructure and properties. The part of the research work is carried out at the Jožef Stefan Institute at the Electronic Ceramics Department.

Attendance at workshops and courses:

- Varno delo z nevarnimi kemikalijami, Most do znanja, Železniki, Slovenia, 14 November 2013.
- Šola kakovosti za analitske laboratorije, Slovenian Institute of Quality and Metrology, Ljubljana, Slovenia, 1–4 April and 25 April 2014.
- Termična analiza, Mettler Toledo course and workshop, Bled, Slovenia, 27 May and 28 May 2015.
- NanoAnalyze Software Workshop and Discovery DSC Hands-On Workshop, 6th Slovenian-Croatian TA Instruments Users´Meeting, Podčetrtek, Slovenia, 27 May 2015.
- Načrtovanje okolju primernejše (trajnostne) embalaže, workshop at the Faculty of Economics and Business, Institute for Technology, Maribor, Slovenia, 18 June 2015.
- Short Summer School on Thermal Analysis & Calorimetry, 3rd Central and Eastern European Conference on Thermal Analysis and Calorimetry, Faculty of Chemistry and Chemical Technology, Ljubljana, Slovenia, 25 August 2015.